

# **MECHANICAL TESTING AND DESIGN OF A LIGHTWEIGHT NOVEL WBD BRAKE DISC**

**Alan Chen**

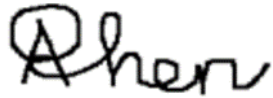
A dissertation submitted to the Faculty of Engineering and the Built Environment, of the University of the Witwatersrand, in fulfilment of the requirements for the degree of Master of Science in Engineering.

Johannesburg 2020

## **DECLARATION**

I declare that this dissertation is my own unaided work. It is being submitted to the Degree of Master of Science to the University of the Witwatersrand, Johannesburg. It has not been submitted before for any degree or examination to any other University.

Signed this 16th day of June 2020

A handwritten signature in black ink, appearing to read 'A Chen', with a stylized, cursive script.

Alan Chen

## **ACKNOWLEDGEMENTS**

I would like to thank my supervisor Prof. Frank Kienhöfer for his support, guidance, and encouragement. He inspired my interest in heavy vehicles and has imparted invaluable knowledge to me. I am extremely grateful for his mentorship.

This research would not have been possible without the financial support of merSETA and my supervisor. I would like to express my deepest gratitude.

I would like to thank my mom, dad, and brother for their motivation and for always believing in me.

Many thanks to Mr. Shaun Riekert, Mr. Andrew Heydenrych, and the rest of the Wits School of Mechanical Engineering workshop for their valuable technical support in preparing the test rig and samples.

## ABSTRACT

Limited research exists on the loading mechanism of a brake disc. The need to determine the mechanical stresses in typical brake disc set-up has never been necessary as these stresses are well below the strength of typical brake disc materials. A recently developed wire-woven bulk diamond (WBD) ventilated brake disc with superior thermal performance has initiated a need to understand how the mechanical stresses within a brake disc are developed. The loading mechanism was separated into the resultant compressive stresses due to the clamping load and the shear stresses due to the applied braking torque. These stresses were measured experimentally using strain gauges mounted on a solid brake disc tested on a custom-built test rig. For the clamping load test, the compressive stresses were concentrated at the disc/pad contact interface. For the applied torque load test, the disc face shear stresses were found to be distributed throughout the circumference of the disc. These results were applied to design the required reinforcement of a WBD brake disc. The analysis was based on the maximum possible deceleration conditions of a medium sized truck. While the WBD material was strong enough to withstand the shearing of the braking torque, the clamping load was determined to cause failure. Consequently, straight radial ribs were designed to reinforce the ventilated core. The final dimensions of the designed rib were 74 x 14 x 2.5 mm, manufactured from mild steel (SAE1006). The core will be reinforced with 10 ribs orientated radially and equispaced at 36° intervals. The 10 ribs adds 0.20 kg to the weight of the WBD disc. Thus, the newly reinforced WBD brake disc remains lighter than a commercially available pin-finned disc, has superior thermal performance and is strong enough to withstand the required mechanical stresses.

# CONTENTS

DECLARATION	i
ACKNOWLEDGEMENTS	ii
ABSTRACT	iii
CONTENTS	iv
LIST OF FIGURES	vi
LIST OF TABLES	viii
LIST OF SYMBOLS	ix
LIST OF ACRONYMS	x
1. INTRODUCTION	1
1.1. Background and Motivation	1
1.2. Objectives	2
2. Literature Review	3
2.1. Brake Disc Designs	3
2.2. Cellular Metal	4
2.3. WBD core	5
2.4. Pad/Disc Interface Pressure Distribution	12
2.5. Identified Research Gaps in the Literature	21
3. EXPERIMENTAL DETAILS AND METHODOLOGY	22
3.1. Test Samples	22
3.2. Brake Test Rig Overview	24
3.3. Instrumentation	25
3.4. Experimental Procedures	26
3.5. Measurement Uncertainty Analysis	32
4. CALIBRATION, VERIFICATION, AND PRELIMINARY TESTS	34
4.1. Load Cell Test	34
4.2. Torque Calibration Test	36

4.3.	Effect of Static Torque on Brake Disc Compressive Strains	38
4.4.	Repeatability of the Uniaxial Strain Gauges Orientated at 45°	40
4.5.	Linearity of Applied Torque versus Shear Strain	42
4.6.	Discretisation of Torque	44
5.	RESULTS AND DISCUSSION	45
5.1.	Overview	45
5.2.	Experimental Clamping Load Test	45
5.3.	Experimental Applied Brake Torque Load Test	50
5.4.	Design Application of the WBD Brake Disc Core	61
6.	CONCLUSIONS	71
7.	REFERENCES	74
	APPENDIX A	78
	APPENDIX B	89
	APPENDIX C	93

## LIST OF FIGURES

Figure 1: Different types of commercially available brake discs	4
Figure 2: Cellular structure: (a) wire-woven bulk Kagome (b) wire-woven bulk diamond	6
Figure 3: Structure of a single layered WBD block structure	7
Figure 4: WBD Unit Cell	7
Figure 5: Zoomed in view of the a) WBD b) WBK cross point	9
Figure 6: WBD unit cell with indications of two different shear directions	11
Figure 7: Brake system showing the floating brake caliper, the brake pads, and disc	13
Figure 8: Back face of inboard brake pad showing the spigot hole	15
Figure 9: Finite element model of pad distortion under load applied by the caliper piston	16
Figure 10: Finite element model of the static interface pressure distribution	16
Figure 11: Finite model of static interface pressure distribution with the caliper	17
Figure 12: Surface topography of the different brake pad pairs	18
Figure 13: Static contact pressure distribution	19
Figure 14: Finite element model of dynamic interface pressure distribution	20
Figure 15: Dynamic interface pressure distribution at various rotation speeds	20
Figure 16: Solid brake disc	22
Figure 17: WBD brake disc	23
Figure 18: Brake test rig with components	24
Figure 19: Uniaxial strain gauges on the brake disc for the clamping test	27
Figure 20: Disc orientation coordinates (outboard face view)	28
Figure 21: Eight uniaxial strain gauges installed for applied torque load test	30
Figure 22: Different orientation of the strain gauges for the applied torque load test	31
Figure 23: Configuration of a 45° strain rosette with three strain gauges	31
Figure 24: Rotating strain gauge coordinate system relative to disc coordinates	32
Figure 25: Load cell test configuration	35
Figure 26: Clamping force and pneumatic chamber pressure relationship	35
Figure 27: Mass hanger with calibration weights applying torque to the shaft	37
Figure 28: Measured strains from the upper location strain gauges in the 45° orientation	41
Figure 29: Measured strains from the lower location strain gauges in the 45° orientation	42
Figure 30: Strain measured by strain gauge 1 to 4 under various applied torque loads	43
Figure 31: Normal strains on the solid disc core measured during the clamping load test	46
Figure 32: Stress distribution around disc circumference due to applied clamping loads	47

Figure 33: Brake pad pressing on the disc exhibiting the contact interface	49
Figure 34: Normal stress $\sigma_\theta$ experienced around solid disc face at the upper rosette	51
Figure 35: Normal stress $\sigma_r$ experienced around solid disc face at the upper rosette	51
Figure 36: Visualisation of the effects of the normal stresses $\sigma_\theta$ on the disc	52
Figure 37: Shear stress $\tau_{\theta r}$ experienced around solid disc face at the upper rosette	53
Figure 38: $\tau_{\theta r}$ experienced around circumferential length at the upper rosette	55
Figure 39: Cross-section of half solid disc with the disc and hub thickness	57
Figure 40: Calculated normal strain $\epsilon_z$ around the solid disc face at the upper rosette	57
Figure 41: Normal stress $\sigma_\theta$ experienced around solid disc face at the lower rosette	58
Figure 42: Normal stress $\sigma_r$ experienced around solid disc face at the lower rosette	58
Figure 43: Shear stress $\tau_{\theta r}$ experienced around solid disc face at the lower rosette	60
Figure 44: Calculated normal strain $\epsilon_z$ around the solid disc face at the lower rosette	61
Figure 45: Cross-section of half of the WBD brake disc	64
Figure 46: WBD core thickness reinforced with rib distributing the compressive pad load	66
Figure 47: Pad area distribution considered to withstand the compressive force	66
Figure 48: Minimum of one rib in the disc core under the contact interface	70



## LIST OF TABLES

Table 1: Ratio of normalised shear to normalised compressive properties of WBD	10
Table 2: Multi-layered WBD properties obtained from analytical solutions	11
Table 3: Physical properties of the solid disc	22
Table 4: WBD sandwich core material properties and disc dimensions	23
Table 5: Test rig component models	25
Table 6: Strain gauge properties	26
Table 7: Strain gauge positions for applied torque test	31
Table 8: Brake disc compressive strains with, and without calibration torque load	39
Table 9: Percentage change of compressive strains with and without applied torque	39
Table 10: WBD disc reinforcement results for maximum compressive pad force	68

## LIST OF SYMBOLS

$\mu$	coefficient of friction [dimensionless]
$\rho_{rel}$	relative density [dimensionless]
$d$	diameter [m]
$D$	wire woven unit cell size [m]
$c$	strut length [m]
$p$	helical pitch [m]
$\varepsilon$	porosity [dimensionless]
$\in$	strain [m/m]
$E$	Young's modulus [MPa]
$G$	Shear modulus [MPa]
$\overline{\sigma_c}$	compressive strength of the wire woven metal composed of the struts [MPa]
$\overline{E}$	equivalent Young's modulus for multi-layered metal [GPa]
$\nu$	Poisson's ratio [dimensionless]
$\gamma$	shear strain [dimensionless]
$\tau$	shear stress [MPa]
$\sigma$	normal stress [MPa]

## LIST OF ACRONYMS

<i>CO<sub>2</sub></i>	Carbon Dioxide
<i>WBD</i>	Wire-woven Bulk Diamond
<i>PCM</i>	Periodic Cellular Metals
<i>WBK</i>	Wire-woven Bulk Kagome
<i>ADC</i>	Analogue-to-Digital converter
<i>D/A</i>	Digital-to-Analogue
<i>FMVSS</i>	Federal Motor Vehicle Safety Standards
<i>EEC</i>	European Economic Community
<i>EU</i>	European Union

# **1. INTRODUCTION**

## **1.1. Background and Motivation**

Vehicle advancement requires components to be lightweight. Reducing vehicle weight, reduces fuel consumption which in turn assists newly produced vehicles to meet stricter emissions standards [1-5]. According to research conducted by the University of Stellenbosch [6], the South African logistics costs increased by more than 9% each year between 2013 and 2015. Lightweighting vehicles is a practical way to reduce logistics costs and CO<sub>2</sub> emissions. Reducing weight is particularly important for a brake disc. A lightweight brake disc ensures the rotating parts possess a low rotational inertia, which allows for more rapid acceleration and deceleration. Lighter brake discs reduce the unsprung mass which improves suspension performance [7]. The main driver for reducing the brake disc weight is however reduced fuel consumption and CO<sub>2</sub> emissions.

The brake disc is a safety critical vehicle component which cannot be made lighter without ensuring the disc has adequate thermal capacity to absorb heat [8-10] and the heat dissipation characteristics of the disc are improved. High brake disc temperatures have a detrimental effect on the disc and pad wear. Furthermore, at elevated temperatures brake fade and thermal cracking are likely to occur. A cooler operating brake disc is thus safer and reduces maintenance costs. Recent studies, by the University of the Witwatersrand [11-14], have shown wire-woven bulk diamond (WBD) to be an excellent ventilated medium for the core of a brake disc to improve the heat dissipation characteristics of a brake disc. WBD is a highly porous, cellular material which is made up of interwoven wires brazed together. The material is high in strength and enhances convective cooling. Laboratory tests [11, 13] show the prototype WBD disc to operate at a 15-25% lower steady state temperature as compared to solid or commercially available pin-finned discs. The results of these laboratory tests were confirmed with on-the-vehicle tests conducted at Gerotek [14] which showed the prototype discs to operate at 29% lower steady state temperature as compared to the commercially available disc.

WBD was chosen by Mew et al. [11] as the highly porous medium in the ventilated channel of the brake disc because of its superior strength over the wire-woven bulk Kagome (WBK); the material properties comparison is analysed in detail in the Literature Review

(Section 2.3). Although the yielding mechanism for the material is complicated and dependent on the wire diameter and slenderness ratio of the struts, the equivalent compressive strength of the material is in the region of 6 MPa [22]. The material has good strength especially when normalised by its mass but is nevertheless weaker than grey cast iron ( $S_{uc} = 570\sim 1290$  MPa) or mild steel ( $S_{uc} = 250\sim 1000$  MPa).

In spite of the good thermal results obtained from the WBD brake disc, the initial calculations and laboratory testing of the disc strength have shown that further research and development is required. The WBD disc was able to withstand a pneumatic chamber braking pressure of 4 bar but failed to withstand an emergency braking pressure of 5.2 bar [15]. At this braking pressure the WBD material was crushed and the disc failed. The upper limit of braking pressure in service is around 7 bar [16]. The need to determine the mechanical stresses due to a typical brake disc set-up has never been necessary as these stresses are typically in the region of 6 MPa; well below the strength of typical brake disc materials like grey cast iron and steel. The proposed use of WBD as a novel medium in a brake disc now requires that the loading mechanism of a brake disc with resultant compressive stresses due to the pad clamping as well as the shear stresses due to the braking torque be characterised.

## **1.2. Objectives**

A main focus of this project is to characterise the loading mechanism of a brake disc. The brake disc is subjected to compressive clamping as well as shearing due to the braking torque. These stresses are aggravated by a rise in temperature which reduces the material strength of the brake disc. The project will aim to understand how a brake caliper loads a brake disc, apply this to the known strength of the WBD material and use this as a basis to predict the stress distribution in the WBD disc. The objectives of this study are to:

1. Measure and characterise the loading mechanism of a brake disc with resultant compressive stresses due to clamping as well as the shear stresses due to the braking torque.
2. Apply the experimental solid brake disc stress distribution results to determine the required strength for the WBD ventilated core for an improved lightweight brake disc that is able to withstand the critical design case loading, specifically maximum clamping load and braking torque.

## **2. Literature Review**

### **2.1. Brake Disc Designs**

A brake disc must provide a rubbing surface (or friction surface) compatible with the brake pad that provides sufficient friction in the region of  $\mu = 0.4$  that is thermally stable so that an easily controllable brake torque can be developed to decelerate the vehicle. A brake disc is thus subjected to thermal and mechanical loads. The disc must provide heat dissipation properties such that it is cooled effectively to avoid excessive temperatures, while remaining lightweight. Furthermore, the disc must be sufficiently strong to resist failure due to the clamping loads of the pads and the frictional shearing of the pads which develop the brake torque; combined with the thermal stresses which are unavoidable.

Commercially available solid brake discs and ventilated brake discs are commonly used; Figure 1a shows a solid brake disc and three ventilated brake discs, namely the radial-vaned, curve-vaned, and the pin-finned core brake discs are shown in Figure 1b, 1c and 1d respectively. The solid brake disc comprises a solid core with a rubbing surface on each side. The solid core brake disc possesses superior mechanical strength and thermal storage capabilities. Solid brake discs have a smaller thickness than ventilated brake discs, and are used mostly on light vehicles.

Current brake disc topology uses a ventilated core for the brake disc with radial or pin-finned cooling passages between the two rubbing surfaces [17, 18]. The cooling passages act as a pump circulating cooling air from the centre of the brake disc to the outer edge of the disc. Ventilated core brake discs are used in heavy vehicles due to their ability to dissipate heat more effectively. Both the internal and external surfaces of the disc are exposed to convective cooling, thereby increasing the overall surface area exposed to cooling [27].

The brake disc topology is however limited by the casting process [19] which precludes the use of a multitude of thin pin fins in the ventilated channel because thin cross sections cannot be economically cast. Therefore, current vanes and pin-fins are prismatic and thick to eliminate casting defects. However, this constraint adversely affects the forced convective heat transfer performance as it limits the flow mixing and heat transfer area [12]. In 1999, Evans et al. [20] proposed the use of cellular metals in multifunctional components because

of their light weight, excellent heat dissipation characteristics and good strength. This led to the development of a patented WBD brake disc which was introduced by Mew et al. [11].

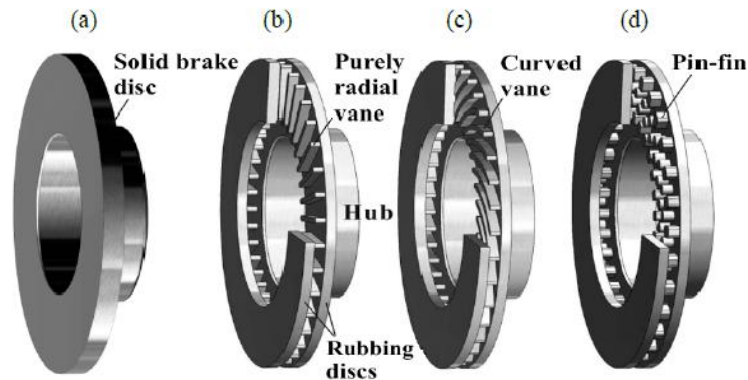


Figure 1: Different types of commercially available brake discs [1]: a) Solid, b) Radial vane, c) Curved vane, d) Pin-finned

## 2.2. Cellular Metal

‘Cellular metal’ is the general term used to describe a metallic body within which any type of gaseous void is dispersed [28]. Open-cell and closed-cell foams are composed of stochastic structures. The irregular topologies of these foams result in lower strength and stiffness per unit weight than their corresponding counterparts, periodic cellular metals (PCMs). PCMs are composed of regular topologies. The honeycomb structure is classified as a type of prismatic PCM having a 2D structure.

Closed-cell foams and honeycomb structures are the predominant choices for the cores of sandwich-structured composites. Honeycombs have excellent strength-to-weight ratio and closed-cell foams are economical. However, the interior space of both of these structures are not accessible for additional functions. Truss type PCMs are based on traditional truss structures used for construction purposes and represent a new approach. Truss PCMs have fully open cells, which allow for utilisation of the interior space for additional functions such as heat dissipation. In addition, the regular periodic structure provides mechanical strength comparable to honeycomb structures [23]. However, mass production of PCMs at an acceptable cost is still underdeveloped [22].

## 2.3. WBD core

### 2.3.1 Structure

Metallic wires offer several benefits as a raw material for the fabrication of truss-like PCMs. Wires have high strength with few defects. Mass production of wires through drawing is cost effective and techniques for wire-woven products are well-developed (based on existing textile processes). Wire-woven metals are composed of periodic topologies with open cells similar to truss type PCMs. The struts that compose the truss-like structure are generally not straight or do not penetrate each other at intersections, unlike for ideal truss PCM configurations. The struts are curve-shaped and pass each other within close contact, hence the 'truss-like' description. The propitious thermal and mechanical properties of a PCM make it a good candidate material for lightweight ventilated brake discs.

Two cellular metal wire structures that have been recently developed will be discussed in the literature: the wire-woven bulk Kagome (WBK) and the wire-woven bulk diamond (WBD), refer to Figure 2 for the cellular structure and the projections in three directions. The Kagome structure mimics a bamboo basket mesh pattern. Lee et al. [21] have shown that the WBK material is limited to a relative density of less than 6.3% due to interference among the wires. The relative density is a function of the slenderness ratio of the struts. A wire-woven metal with a higher relative density increases its load-supporting ability. The upper limits of the relative density of the multi-layered wire-woven metal is 42.5%. However, the heat transfer performance is closely related to the relative density, thus a balance is required between the mechanical strength and heat dissipation properties when considering the cellular material. The relative density ( $\rho_{rel}$ ) is defined as the ratio of the density of the cellular metal to that of the mother metal (the mother material refers to the metallic wires).

The University of the Witwatersrand has patented the WBD brake disc [24], but the concept is also being researched at the Fraunhofer Institute in Germany [25]. The 'Strucwire' structure uses multiple layer of wire woven around each other to create a 3D structure, similar to WBK. Because the helical radius of the wires used for Strucwire are very large, and approximates the cell size; the struts composing Strucwire are severely curved, like an arc, which lowers the strength of the material [26]. The Strucwire disc is still in the conceptual phase with no laboratory tests [11-13] or on-vehicle tests published [14].



The WBD structure is made of a wire woven cellular structure composed of regular octahedrons and cuboctahedrons. The "diamond" truss nomenclature arises from the side view of the structure which reveals a diamond shape [22], as shown in Figure 2b. The cellular metal structure has high strength and stiffness because the wires have high strength and toughness. The single layered WBD structure (Figure 3) is fabricated using the following process: four straight steel wires with identical diameters are twisted together until plastic deformation occurs. Thereafter, the wires are untied from each other giving each wire a helical shape. The 2-dimensional mesh is weaved using the helical wires (in-plane assembling). Multiple 2D meshes are stacked parallel at constant intervals. Additional helical wires are spin-inserted in four out-of-plane directions. Refer to Figure 4 for the WBD unit cell. An in-depth fabrication procedure is described by Lee et al. [22].

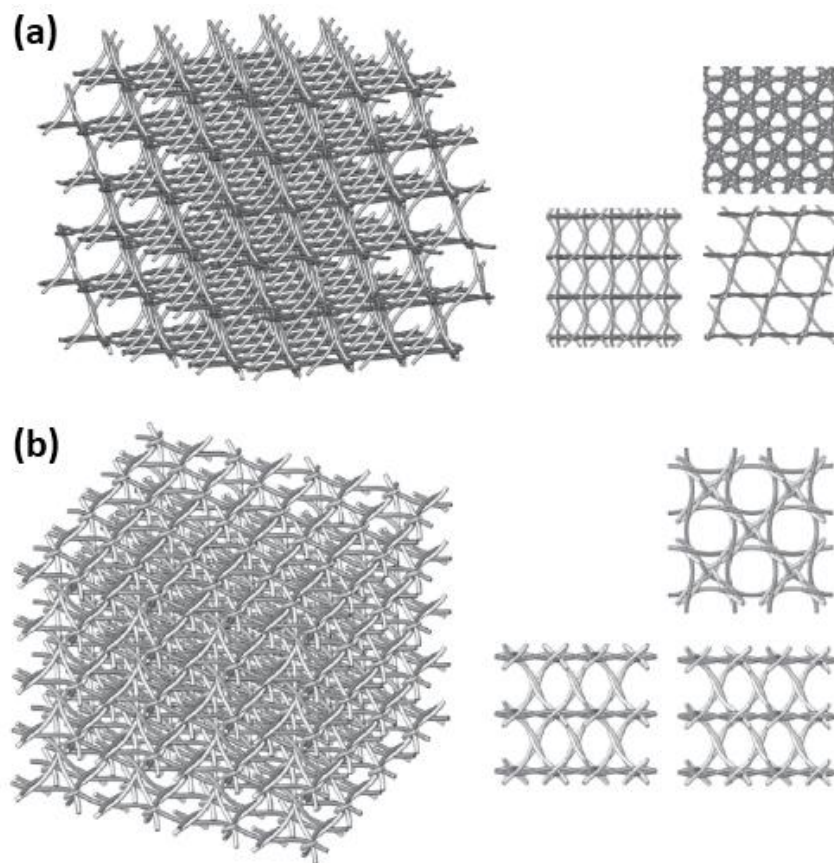


Figure 2: Cellular structure: (a) wire-woven bulk Kagome (b) wire-woven bulk diamond [28]

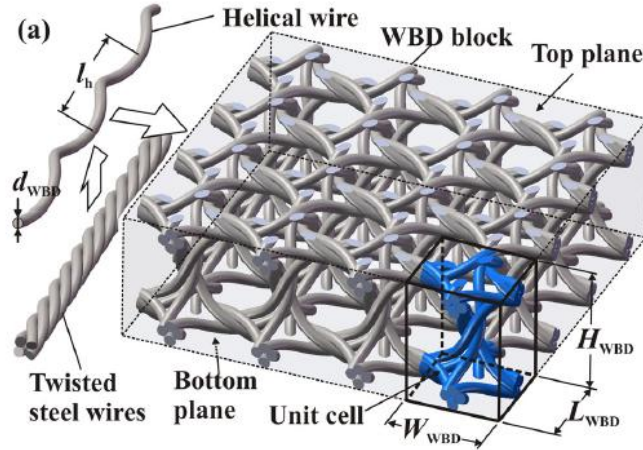


Figure 3: Structure of a single layered WBD block structure [12]

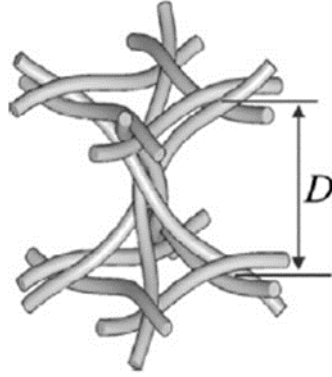


Figure 4: WBD Unit Cell [28]

### 2.3.2 Material Properties

The WBD core of the brake disc is manufactured using cold-rolled mild steel wires with diameters of  $d = 1.5$  mm and helical pitches of  $p = 19.0$  mm. Referring to the unit cell in Figure 4, the lengths of the wires that comprise the stacked 2D meshes (the square lattice form) are identical on all four sides. The helical wires that are screwed into the multiple layers of the 2D meshes in the four out-of-plane directions at  $45^\circ$  angles (the wires running diagonally through the stacked meshes) are twice the length of the wires of the 2D mesh wires. Therefore, for the WBD unit cell the following dimensions apply: length = 9.5 mm, width = 9.5 mm, height = 14.0 mm. As a result, the WBD core possess a porosity of approximately  $\epsilon \approx 0.9$  and a surface area density of approximately  $255 \text{ m}^2/\text{m}^3$  [11, 12]. The relative density can be calculated as  $\rho_{\text{rel}} = 1 - \epsilon = 0.1$ . These values are calculated based on the idealised diamond unit cell with straight struts (equations shown in Table 2). When

considering the helical ligaments (hence curvature of the struts), the relative density and surface area density increases by approximately 15%, which needs to be considered [12].

Using the above dimensions, the experimentally determined equivalent yield strength, maximum strength, and Young's modulus of the WBD core are 3.2 MPa, 4.8 MPa, and 1.08 GPa, respectively [11, 12].

### **2.3.3 WBD Compressive Strength Characteristics**

For a given slenderness ratio of the cellular wires, the density and strength of WBD are approximately twice as large as compared to WBK; while the equivalent Young's modulus is 50% higher [22]. The normalised (by mass) equivalent strength and normalised modulus of WBD is weaker than WBK. The WBD geometry has four wires closely pass by one another at each cross point, while the WBK has three wires. Figure 5a) and b) reveal the close-up views of the cross point and the cross-sections at the midpoint of the two materials. Lee et al. [22] found the helical radius of WBD to be 22.5% higher than for WBK. The higher helical radius results in a higher eccentricity of the struts of the WBD structure which results in a lower Young's modulus. Figure 5 shows that the filler metal occupies volume at the cross points, after undergoing the brazing process; the heights of the brazed portions are denoted as 'B'. This brazed portion decreases the eccentricity and the strut length which prevents premature buckling of the structure, resulting in the material possessing higher strength and modulus. The disadvantage of increasing the filler metal is that it increases the relative density which adversely affects the normalised equivalent strength and modulus. The WBD structure was determined to possess a higher filler metal proportion of the volume than compared to the WBK. The conclusion from the compressive characteristic test by Lee et al. [22] highlights that the WBD structure is able to achieve relative density values of 12.8% while WBK can only achieve 6.3%, thereby making WBD more suitable for heavy duty applications. The heat dissipation of WBD is better than WBK as it has twice the surface area. Additionally, under shear loading, the strength of the WBD material has a lower dependency on the orientation or loading direction as compared to WBK, rendering it more suitable as a sandwich core in the brake disc.

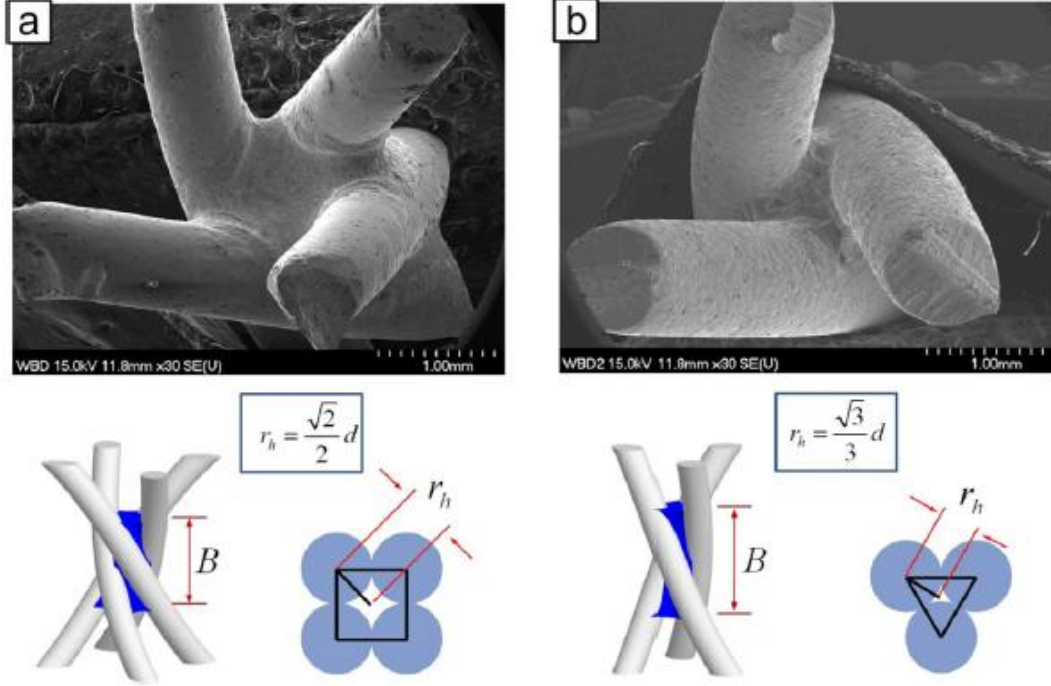


Figure 5: Zoomed in view of the a) WBD b) WBK cross point [22]

### 2.3.4 WBD Shear Strength Characteristics

The curved struts of the wire-woven metals have been shown [29] to significantly degrade the mechanical properties such as the strength and stiffness of the wire-woven structures. As a result, the strengths of the wire-woven materials with the more curved struts are more susceptible to “bending-dominate” than “stretching-dominate” [30]. When a cellular material is loaded, if the strut joints of the cellular material are free to rotate, then the struts support axial loads (tension and compression) and failure occurs due to axial loading of the struts (stretching-dominate). If the strut joints are not free to rotate, then the applied load induces bending moments at the joints and failure occurs due to bending of the struts (bending-dominate). The degree of “curviness” of the struts are defined by the helical radius of the wires that are used to create the structure, where the larger the helical radius the greater the strength degradation.

For the application of the wire-woven material as a sandwich core, the shear properties are more important than the compressive properties. For the first estimation of the shear strength of the WBD material, it can be estimated from the compressive strength through an

expression of the strength ratios as calculated from the analytic solutions [31]. The ratios of the shear properties to the compressive properties is given in Table 1. For a specified relative density, the equivalent shear strengths are significantly degraded in comparison to the equivalent compressive strengths.

Table 1: Ratio of normalised shear properties to normalised compressive properties of WBD at a specified relative density [28]

WBD	
$\frac{\bar{\tau}_0}{\bar{\sigma}_0}$	0.5 - 0.7
$\frac{\bar{G}}{\bar{E}}$	0.33 - 0.4

Similar to the shear strength; the shear modulus of the WBD material can be estimated from the Young's modulus using analytical solutions as expressed in Table 1, where  $\bar{\sigma}_0$  and  $\bar{\tau}_0$  are the equivalent compressive and shear strengths at a given relative density, respectively.  $\bar{E}$  and  $\bar{G}$  are the equivalent Young's modulus and shear modulus for multi-layered metal, respectively. It is clear that for a specified relative density, the equivalent shear modulus of WBD is further degraded from the equivalent Young's modulus (ratio = 0.33 – 0.4) than the equivalent shear strength from the equivalent compressive strength (ratio = 0.5 – 0.7).

### 2.3.5 WBD Structure Orientation Effects

For the WBD, two different orientations, A and B, provide the maximum and minimum equivalent shear strengths, respectively, as shown in Figure 6. Orientation A is rotated 45° from orientation B. The equivalent shear strength and modulus for the two directions do not differ significantly [31]. Shear failure of the WBD is due to elastic or plastic buckling of one of the four out-of-plane struts in the pyramid. Orientation B has a lower equivalent shear strength and modulus than orientation A. This result can be proven using analytical solutions or FEA [31, 32].

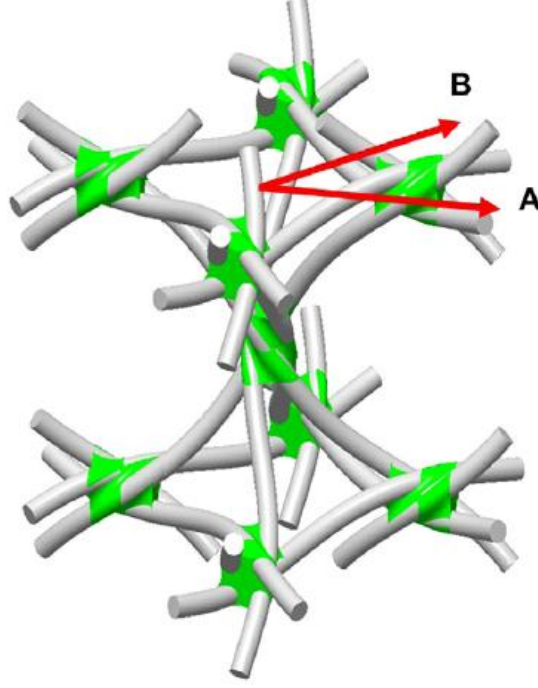


Figure 6: WBD unit cell with indications of two different shear directions [31]

### 2.3.6 Failure Strains

The equivalent failure strains can be estimated by dividing the equivalent strength of the WBD by the corresponding equivalent Young's modulus. Analytic solutions derived by Kang et al. [28] (See Table 2) can be used to express the WBD equivalent failure strains as  $\bar{\epsilon} = 3 \frac{\sigma_0}{E}$  where  $\sigma_0$  is the yield strength of the wires.

Table 2: Multi-layered WBD properties obtained from analytical solutions [28]

Multi-layered WBD	
Relative density	$\frac{3\sqrt{2}}{2} \pi \left(\frac{d}{D}\right)^2 \geq 0.0053$
Equivalent compressive strength	$\frac{\sqrt{2}}{2} \pi \left(\frac{d}{D}\right)^2 \sigma_c = \frac{\rho_{rel} \sigma_c}{3}$
Equivalent Young's modulus	$\frac{\sqrt{2}}{6} \pi \left(\frac{d}{D}\right)^2 E = \frac{\rho_{rel} E}{9}$
Strut length	$\frac{D}{\sqrt{2}}$

Where:

$\sigma_c$  : strut failure strength subjected to compression loading

E : Young's modulus of the strut

The analytical solutions of the WBD properties as shown in Table 2 do not consider the effects of the wire curvatures. However, the factor that affects the strength more is the strain hardening of the wires. During the process of preforming the wires: the four straight wires are twisted together until plastic deformation, and then untied from each other to generate the required helical shape. The wires are plastically formed mainly through shear deformation.

The wire-woven metals have an upper limit in the relative density due to the interference in the wires. The relative densities were calculated using CAD to account for realistic geometries (which was not considered in the analytical solutions) such as wire curvature the brazed filler metal. The upper limit of the relative density for WBD was calculated to be  $\rho_{rel} = 12.8\%$ .

## **2.4. Pad/Disc Interface Pressure Distribution**

### **2.4.1 Introduction**

The floating brake caliper configuration consists of brake pads, caliper, brake disc, and piston (see Figure 7). During the braking action, the caliper presses the pads against the disc, and should ideally achieve full contact on the pad area with a uniform pressure distribution between the contacting pad/disc surfaces. Uniform interface pressure between the pad and disc results in uniform pad wear and brake temperatures, and more stable pad/disc friction coefficients [8]. For safe and consistent braking the pad must maintain proper contact with the disc. However, in practice incomplete contact may be observed. Even if full contact is achieved, the interface pressure between the pad and disc is not necessarily uniform. Therefore, understanding the distribution of the interface pressure is important for the successful design and safe operation of disc brakes, especially for heavy duty applications as this will provide insight into how the applied pad forces are transferred through to the brake disc.

Mechanical and thermal loads influence the pad distortion which ultimately affects pressure distributions. The pressure and contact at the pad/disc interface can be considered at three levels [33, 35]. The first level is the large-scale pressure variation over the full contact interface which is induced by bulk deformation (flexural) effects in the application of the braking force. The second level is the “macroscopic” interface pressure distribution. These refer to the localised variations in contact and pressure, arising from localised deformation or distortion of the pad/disc. The third level represents frictional contact on the microscopic scale and is fundamental to the study of friction and wear. The first two levels are within the control of the brake designer, while the third depends on the tribological characteristics of the pair of contacting surfaces.

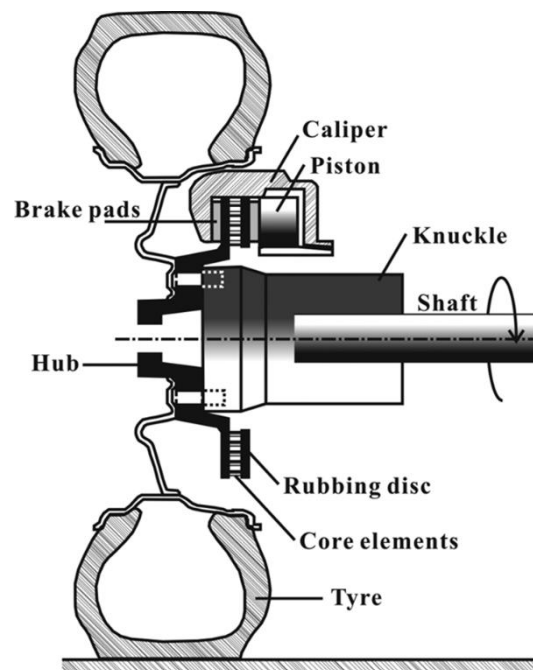


Figure 7: Brake system showing the floating brake caliper, the brake pads, and disc [11]

#### 2.4.2 Static Contact Interface Pressure Distribution

The dynamic interface pressure distributions in disc brake systems are currently impossible to measure directly using experimental methods as the measuring devices are destroyed in the friction area, but static pressure distributions have been measured. Dubensky [36] used pressure sensitive paper to measure the static pressure distribution between the brake disc and pad. Tumbrink [37] measured the pressure distribution at the disc and pad interface using steel balls and optical techniques.



Tirovic and Day [33] credit Harding and Wintle [34] as the first to publish research investigating pressure distributions in disc brakes, where the flexural effects in the brake pad assembly were studied both theoretically and experimentally, by applying the theory of beams on elastic foundations and analysing two-dimensional finite element models.

Brake pad material possesses a relatively low modulus of compression. Therefore, it is not practical to directly apply load to the material unless the material is sufficiently large to avoid excessive compression. This leads to the requirement of using a metal backplate to transmit the pressure between the pad and the piston (refer to Figure 9a). The pad assembly consists of the slab of friction material mounted on a flat metal backplate. The metal (commonly steel) backplate provides the flexural stiffness. It also plays a vital role in locating the assembly within the caliper and carries the frictional drag force. When the brake is applied the interface between the pad and backplate is always in compression. Brake pad designs can take many different general shapes, those with a high aspect ratio (length to width) can be treated theoretically as a plate beam on an elastic friction material foundation which is support by the rigid disc [34].

Single piston caliper designs may be subjected to pad assemblies that have high aspect ratios, hence the need for the analysis of the pressure distribution over the pad length. A single piston caliper can be modelled as a single concentrated load applied at the centre of the backplate. Harding and Wintle [34] found that any pad length greater than a critical length value would result in inefficient pressure distribution and a change from compression to tension along the pad/backplate interface towards the ends. In other words, high aspect ratio pads may separate at the interface and cannot distribute pressure beyond the critical length. The critical length is dependent on the relativity of the compression modulus of the pad friction material to the flexural stiffness of the backplate. The spigot hole on the inboard pad (refer to Figure 8), which locates the piston to the backplate, reduces the localised section modulus of the backplate, which can be compensated for with a thicker backplate for the inboard pad as compared to the outboard pad. The pad backplates are commonly manufactured using mild steel.

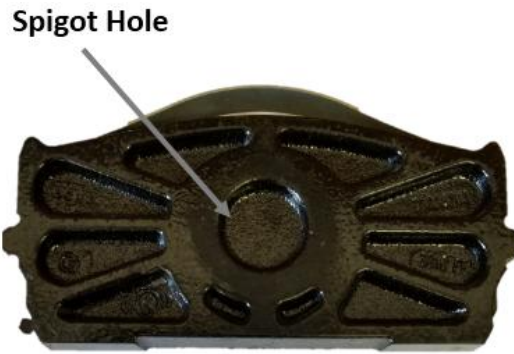


Figure 8: Back face of inboard brake pad showing the spigot hole

Figure 9 shows the finite element model of the pad distortion (exaggerated deflection for illustration purposes) when under applied load by the caliper piston during the braking action. The static pressure distributions are due only to the compressive forces that are transmitted at the interface, with no dynamic friction drag on the pad surface. The force applied to the pad was reacted by the brake disc which was modelled as being rigid (infinite stiffness). It was proven that the static results were linear i.e. halving the actuating force halves the interface pressure at any point of the friction surface.

Tirovic and Day [33] further analysed the results of Harding and Wintle [34] as described earlier. The length of the friction material of the pad that is in contact with the disc depends on the compressibility of the friction material. In the ideal scenario the full length of the friction material (pad) would be in contact with the brake disc. For standard friction material, only 75% of the pad surface area is contact with the disc. This value is reduced to 60% if a stiff friction material is chosen.

Figure 10 exhibits the static interface pressure distribution on the pad for one of the configurations tested. The figure only shows half a pad, where the most left vertical line represents the pad centre-line. The darker regions represent the highest magnitude of the interface pressure, while the white regions represent the lowest magnitude of pressure. The interface pressure is the greatest near the centre of the pad, decreasing towards the outer regions of the pad as seen in the shade gradient in the figure. Near the right edge of the pad there is no interface pressure as there is lifting of the pad, known as the lift off region. This signifies that there is no contact between the pad and disc as was discussed earlier regarding the critical length.

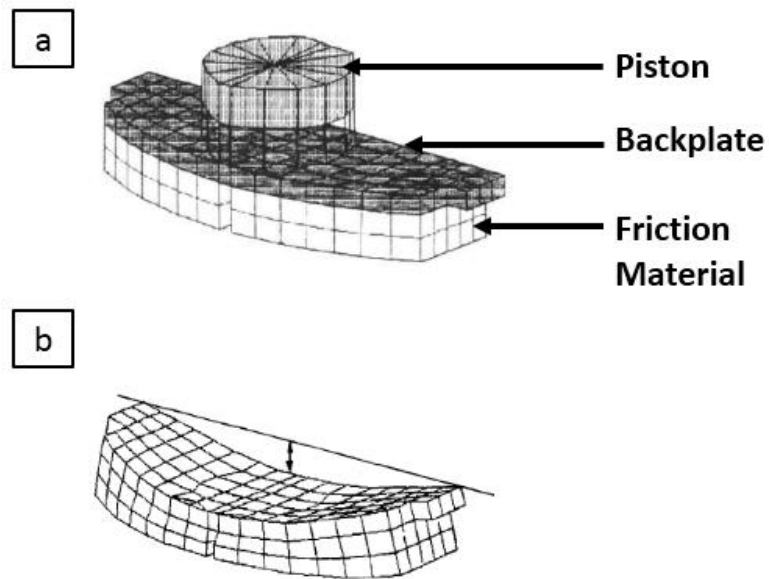


Figure 9: Finite element model: a) caliper piston and pad backplate and friction material, b) pad distortion under load applied by the caliper piston; figure adapted from [33]

Abu Bakar et al. [38] showed through their validated 3-dimensional finite element model that during the braking action when the disc is stationary the pressure distribution is symmetric about the geometric centre line of the pad, as seen in Figure (15.a). The static interface pressure distribution from the finite element analysis from Figure 10 and Figure (15.a) assumes linear elastic behaviour and perfect initial contact, which means that contacting surfaces of the pad and the disc are modelled to be perfectly aligned when they are brought together. However, that is only an ideal case.

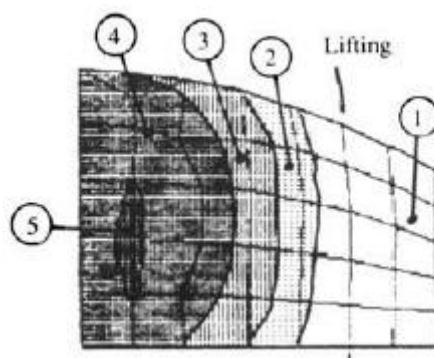


Figure 10: Finite element model of the static interface pressure distribution for inboard half pad [33]

Interface pressure variations can occur due to caliper distortion and deflections under operational loads. Their finite element model included the floating caliper and the outboard

pad (non-piston side) in the analysis. Only the static interface pressure distribution was considered in the analysis, hence no braking torque was applied. The inboard pad interface pressure distribution (seen in Figure 11) is similar to the results of Figure 10 (which did not model the caliper) in size but the contact area is slightly reduced in the caliper model. For the caliper model, the centre of pressure is shifted outwards. Under the braking action, significant caliper displacements were observed due to the compression of the friction material [33], but also floating calipers can open out under actuation load. This shifts the maximum pressure interface on the outboard pad to the outer region as seen in Figure 11.

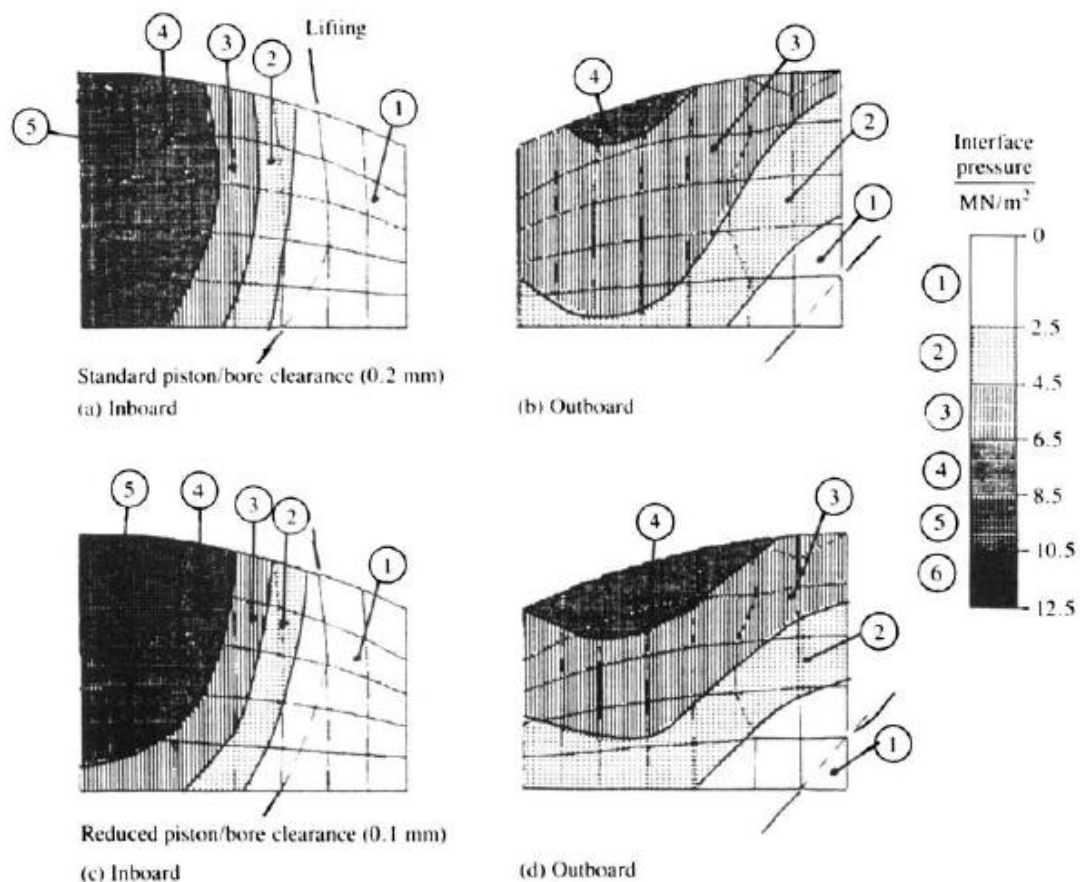


Figure 11: Finite model of static interface pressure distribution with the caliper [33]

### 2.4.3 Brake Pad Surface Topography

Studies by Chen et al. [39] showed that there is a variation in the static contact interface pressure distributions of new sets of brake pads; even if the pads are tested with the same brake system under the same braking pressure. Abu Bakar et al. [40] investigated the cause and suggested that one of the reasons for the different contact pressure distributions is the

variation of the brake pad surface topography, as the surface profiles are different for each pad. The investigation was conducted experimentally by measuring the pressures at the contact interface using pressure indicating films which were then post-processed using proprietary software to obtain the pressures quantitatively. The brake pad surface topography was measured using a linear gauge. Both new and worn brake pads were tested and studied. A solid brake disc with a floating brake caliper setup was utilised. A 3-dimensional finite element model was also developed.

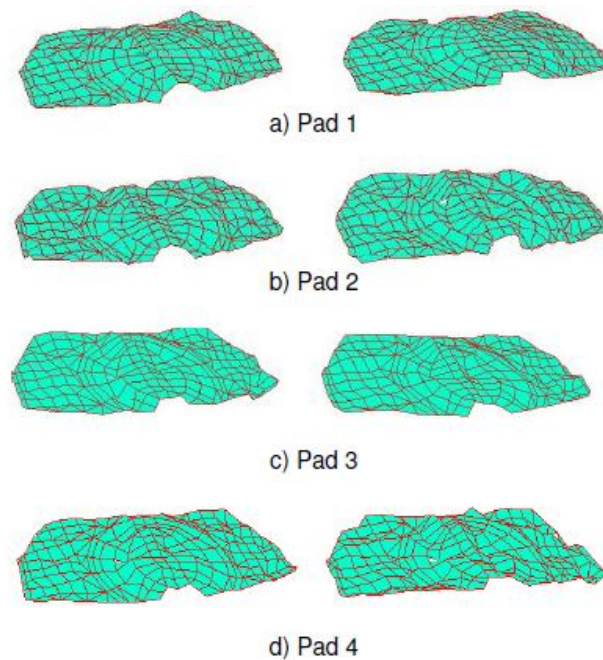


Figure 12: Surface topography of the different brake pad pairs [40]

The surface topography is different for each pad as shown in Figure 12, despite them all being made from the same manufacturer. Figure (13.a) shows the static interface contact pressure distribution for one set of the new pads tested by Abu Bakar et al. [40] obtained experimentally, on the inboard and outboard pads. Figure (13.b) was the simulated result after inputting the surface topography. The results were in agreement with each other. It was further observed that the higher the applied pressure, the greater the generated contact area, and the greater the maximum pressure. The trailing edges had the lowest pressure (close to zero) while the outer boarder regions had the highest pressures. It was concluded from the results that variations in contact pressure distributions between different pads on the same test rig were due to the brake pad surface topography. Therefore, when brake pad pairs are fitted in brake systems in vehicles, the left and right

wheels may produce different braking torques as the contact pressure distributions may be different [40].

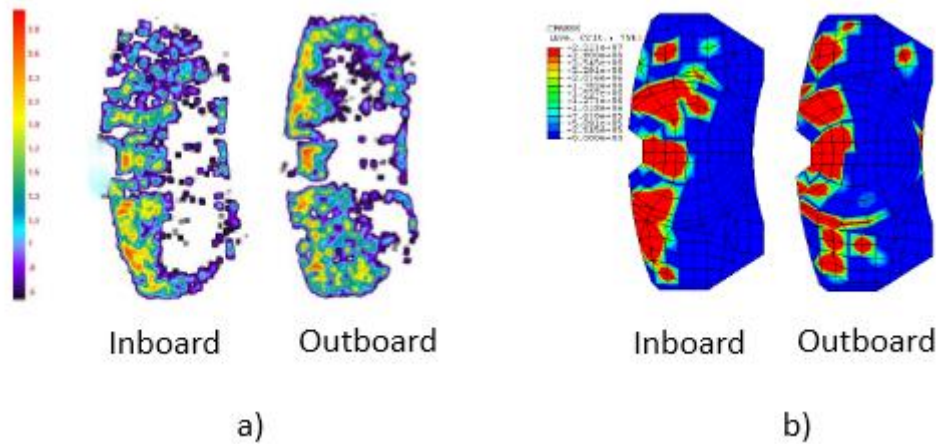


Figure 13: Static contact pressure distribution a) analysed image from pressure film sensor test b) simulated results of the pad with the same surface topography [40]

#### 2.4.4 Dynamic Contact Interface Pressure Distribution (Numerical)

The dynamic interface pressure distributions in disc brake systems cannot currently be measured using experimental methods. Finite element models are required. Figure 14 shows the results for a finite element model of the dynamic interface pressure for a coefficient of friction value  $\mu = 0.30$  [33]. The results show that the leading edge (where the pad first contacts the brake disc) maintains contact, however, the trailing edge loses contact over the last part of its length. Abu Bakar et al. [38] investigated the pressure distributions at different disc rotational speeds while applying the braking load as shown in Figure 15. Under the braking action with the disc rotating, the contact pressure distributions are no longer symmetric about the geometric centre of the pad. Additionally, the highest pressure now occurs at the leading edge (the bottom side of the figures are the leading edges), which is in agreement with the results from Tirovic and Day [33]. For the speed  $\Omega = 6$  rad/s, the ratio of the computed contact area to the apparent contact area is 86.0% which also exhibits that a small section of the pad/disc does not make contact.

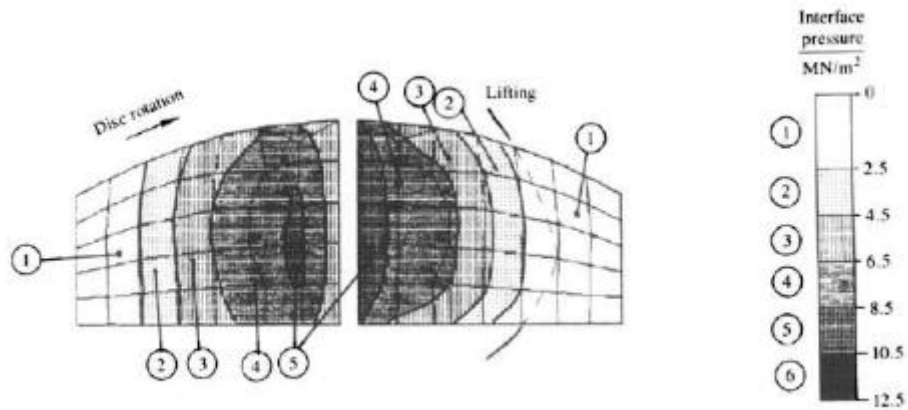


Figure 14: Finite element model of dynamic interface pressure distribution [33]

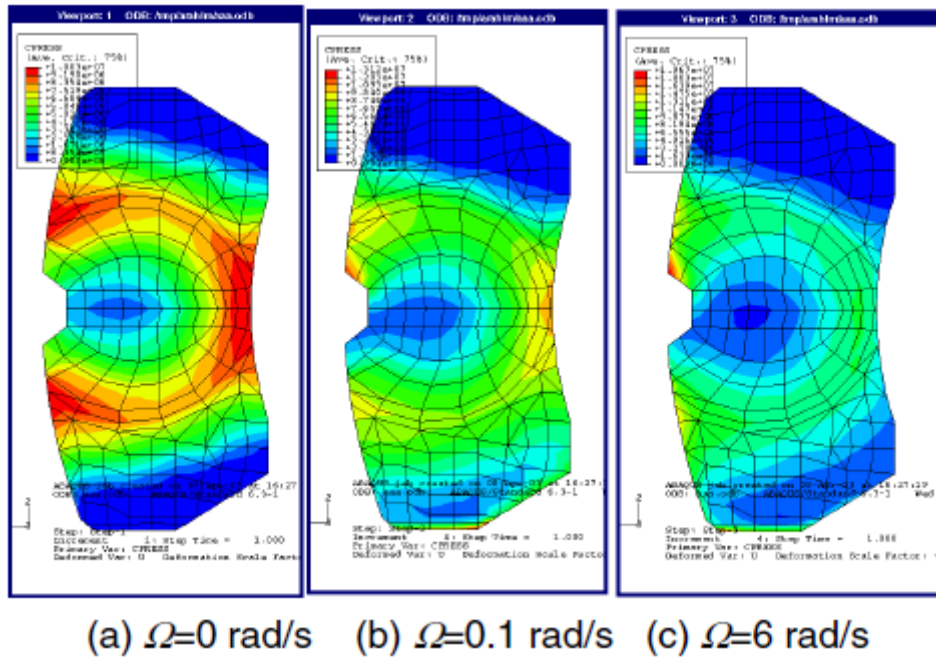


Figure 15: Dynamic interface pressure distribution at various rotation speeds [38]

There is significantly more wear on the leading side than on the trailing side of a worn pad. The uneven wear is caused by the higher pressure on the leading edge of the pad/disc contacting interface. It is estimated that the pressure at the leading edge will be as much as one-third greater than the average pressure [38].

## **2.5. Identified Research Gaps in the Literature**

The WBD brake disc has been shown to offer superior thermal performance but a structural analysis of the WBD disc has not been conducted. The novel brake disc must be proven to be sufficiently strong to resist failure due to the clamping loads of the pads and the frictional shearing of the pads which develop the brake torque, at the upper limits of the braking conditions in service.

The cellular metals and in particular the WBD material properties have been characterised but these have not been applied to the design of a component or machine. The characterisation of the loading mechanism of a brake disc can be applied with the material properties to determine the stresses developed in the cellular metals to evaluate the design of the component.

The pressure at the pad/disc interface has been characterised but the mechanical stresses in the disc have not been investigated. In this research the solid brake disc mechanical stresses and their distribution around the disc circumference will be determined experimentally.



### 3. EXPERIMENTAL DETAILS AND METHODOLOGY

#### 3.1. Test Samples

Testing was conducted on a commercially available solid brake disc. The experimental results and understanding of the mechanical stresses developed in a solid brake disc were used to redesign the WBD prototype to withstand the mechanical loads applied to a brake disc.

##### 3.1.1 Solid Brake Disc

A commercially available solid brake disc (Figure 16) was donated by Alfa Brakes based on the dimensions of a Mercedes Benz Atego 500 series. The grey cast iron disc was cast as a single unit and heat treated. The solid brake disc was skimmed to ensure a uniform thickness was obtained around the disc. The physical properties of the solid brake disc are shown in Table 3, which include the material standard and grade, modulus of elasticity (E), Poisson's ratio ( $\nu$ ), modulus of rigidity or shear modulus (G), outer disc radius and rotor thickness.

Table 3: Physical properties of the solid disc

Solid Brake Disc	
Material	Grey Cast Iron
Grade	BS 1452 Grade 17 or SABS 1034-1975 Grade 250
Modulus of Elasticity (E)	120 GPa
Poisson's Ratio ( $\nu$ )	0.26
Modulus of Rigidity (G)	48 GPa
Outer Disc Radius	167 mm
Rotor Thickness	32.4 mm

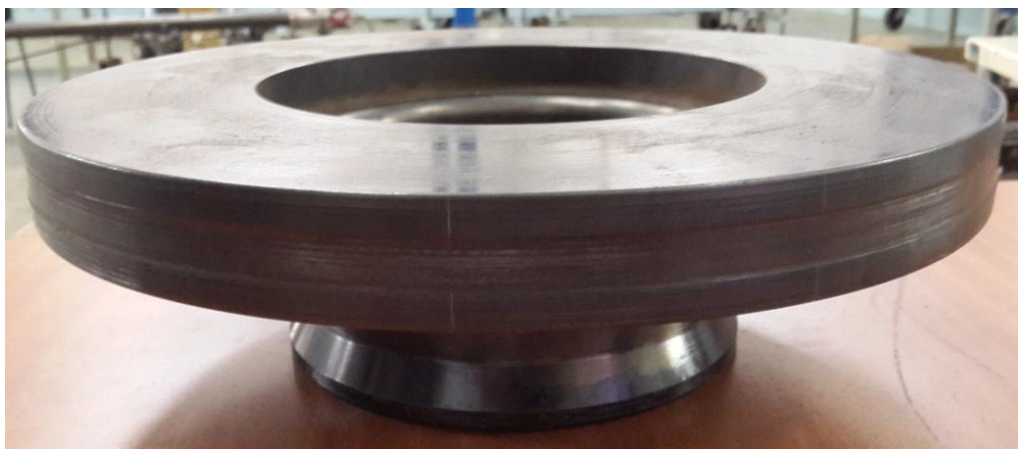


Figure 16: Solid brake disc

### 3.1.2 WBD Brake Disc

The sandwich core of the WBD brake disc prototype (shown in Figure 17) is currently manufactured in South Korea through an agreement with Professor Kang of Chonnam University. The WBD core brazed to the mild steel rubbing plates is shipped to the University of the Witwatersrand, Johannesburg (Wits). The Wits School of Mechanical Engineering workshop welded the brake disc hat on to the sandwich core supplied by Chonnam University and machined the required holes so that the disc can be mounted on a wheel hub. The cellular structure and material properties of the WBD were discussed in detail in the Literature Review (Section 2.3). The key points for selecting the WBD material for the core of a ventilated brake disc were the good normalised strength and stiffness properties, and the improved heat dissipation characteristics. The equivalent material properties and disc dimensions of the WBD are shown in Table 4.

Table 4: WBD sandwich core material properties and disc dimensions

WBD Core	
Equiv. Compressive Strength	6 MPa
Equiv. Yield Strength	3.2 MPa
Equiv. Maximum Strength	4.8 MPa
Equiv. Young's Modulus	1.08 GPa
Outer Disc Radius	168 mm
Ventilated Channel Width	14 mm
Rotor Thickness	10 mm (Each Rubbing Disc)



(a)



(b)

Figure 17: WBD brake disc a) Mercedes Benz Atego prototype b) with one transparent rubbing disc to display the core [11]

### 3.2. Brake Test Rig Overview

A custom-built test rig was used to replicate the applied braking loads experienced by the disc of a medium sized truck when operated in the field. The test rig is shown in Figure 18 and the manufacturer and model specification of each component are listed in Table 5. The entire rig was electrically grounded, including the safety cage (not shown in the figure).

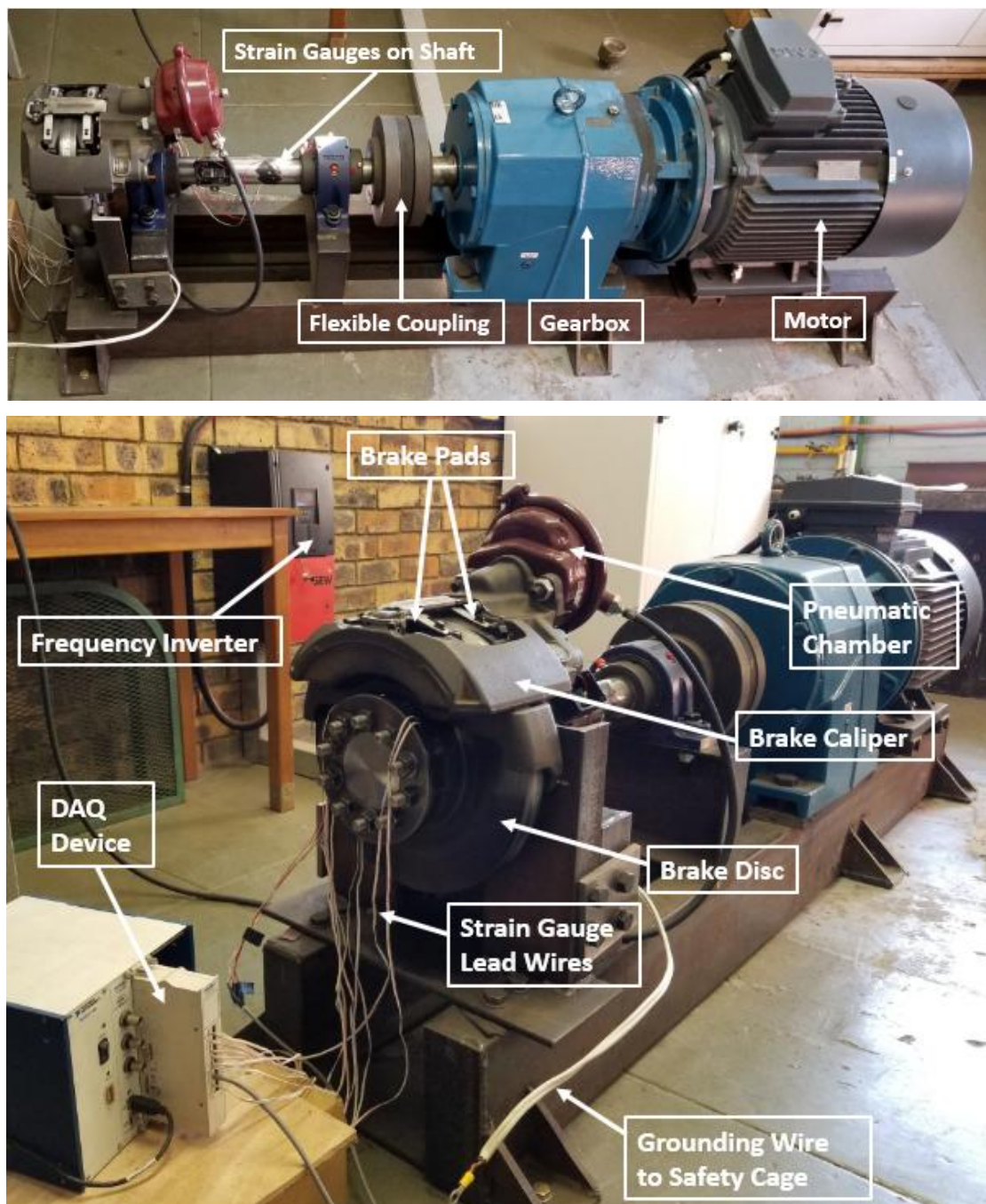


Figure 18: Brake test rig with components

The test rig consists of a 37 kW (3 phase 400 V) AC induction motor which has a maximum speed of 1500 RPM and maximum torque of 1030 Nm. The motor speed and/or torque was

regulated by the SEW frequency inverter that received the set values through the adjustment of the wired potentiometer. The motor was geared to a gearbox with a reduction ratio 3.7:1. The gearbox transmits torque to the shaft through a flexible coupling. The shaft was manufactured from EN8 mild steel and has an outer diameter of 60 mm. The opposite end of the shaft was flanged to allow the mounting of the brake disc through fastening of the bolts. The shaft rotates on two non-self-aligning bearings.

A floating brake caliper with a single piston was used to apply brake pressure on the brake disc through the brake pads, as shown in Figure 18. The brake caliper was actuated using a pneumatic chamber which was controlled using a Festo digital proportional pressure regulator. Externally supplied compressed air at 6 bar was fed to the inlet of the pressure regulator. The braking force was regulated by the pressure regulator controlling the air pressure supplied to the pneumatic chamber. The set point was selected on the pressure regulator by the user.

Table 5: Test rig component models

Component	Manufacturer	Model
AC Induction Motor	Marathon Electric	MART 225S-4 B35
Frequency Inverter	SEW Eurodrive	MOVITRAC LTP-B
Gearbox	David Brown	Series M (M10213.6.BGC-1)
Brake Caliper	Knorr-Bremse	SN5
Pressure Regulator	Festo	VPPM-6L-L-1-G18-0L6H-V1P-C1

### 3.3. Instrumentation

Uniaxial strain gauges were installed on the brake disc to measure the strains. A 3-wire lead system was used to compensate for temperature effects. Biaxial stacked rosettes were installed on the shaft to determine the torque. The strain gauge properties for both strain gauges are shown in Table 6.

Signal conditioning of the data from the strain gauges was performed using a data acquisition device (DAQ) from National Instruments as shown in Figure 18. The system included the SCXI 1000 chassis which housed and powered all the modules, the SCXI 1600 USB DAQ module which controlled the signal conditioning modules and interfaced with the computer through USB, the SCXI 1520 strain-gauge module, and the SCXI 1314 terminal

block to which the strain gauge lead wires were connected to through screw terminals. NI-DAQmx and LabVIEW proprietary software were used to convert the signals from the data acquisition devices into measured strains.

Table 6: Strain gauge properties

	Uniaxial Strain Gauge	Torque Strain Gauge
Manufacturer	KYOWA	KYOWA
Model	KFG-2-350-C1-11L1M3R	KFGS-5-350-D16-11L1M2S
Gauge Length	2 mm	5 mm
Gauge Resistance	$350.0 \pm 2.4 \Omega$	$350.0 \Omega \pm 0.7\%$
Gauge Factor	$2.10 \pm 1.0\%$	$2.14 \pm 1.0\%$

A LabVIEW program was written to retrieve the strain signals from the SCXI DAQ which was then converted into readable strain values that were stored coupled with the corresponding timestamps in a textfile format.

### 3.4. Experimental Procedures

Two separate tests were conducted to characterise the loading of a brake disc: a clamping load test and a torque load test.

#### 3.4.1 Clamping Load Test

Shunt calibration and offset nulling were performed prior to testing. The strain values were continuously sampled at a frequency of 100 Hz. The strains were sampled over a time period of 10 seconds and averaged to reduce noise effects. Three strain gauges, 30° radially apart from each other, were utilised to ensure repeatability of the measured strains as shown in Figure 19. The strain gauges were aligned in the same direction as the applied braking force of the pads such that the strains due to the compressive braking were measured. The clamping load test was performed under the condition of a stationary brake disc.



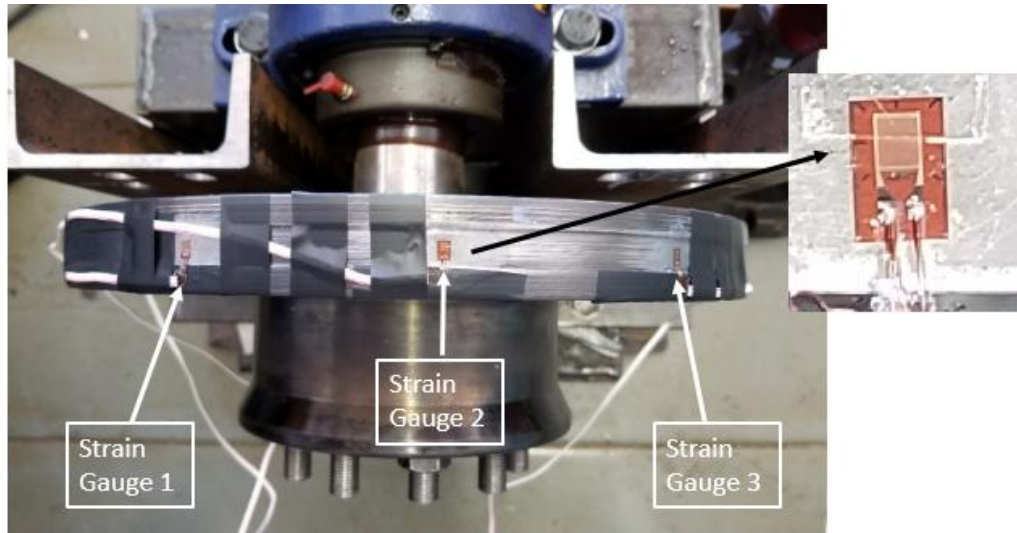


Figure 19: Uniaxial strain gauges on the brake disc for the clamping test

Figure 19 shows the positions of the three strain gauges on the disc core. The disc orientation coordinates are shown in Figure 20. The positive sign convention was set as clockwise rotation around the disc. For the testing procedure, the three strain gauges were first aligned with strain gauge 1 at  $0^\circ$ , strain gauge 2 at  $30^\circ$ , and strain gauge 3 at  $60^\circ$  on the brake disc coordinates as shown in Figure 20. The pneumatic chamber was pressurised such that the clamping load was applied by the brake pads on the disc and the strain measurements from the strain gauges were recorded. The pneumatic chamber was depressurised releasing the clamping load. Thereafter, the strain gauge positions were adjusted to the next testing coordinates by rotating the disc to the next orientation. (Although the disc was rotated to different orientations for each test, the disc coordinates remain unchanged i.e. the  $0^\circ$  coordinate was always taken to be at the top circumferential position;  $90^\circ$  the rightmost circumferential position;  $180^\circ$  the bottom circumferential position; and  $270^\circ$  the leftmost circumferential). The disc coordinates did not change but rather it was the position of the strain gauges within the coordinate system that changed. Strain gauge 1 was originally at  $0^\circ$ , but when rotated clockwise by  $15^\circ$ , strain gauge 1 would then measure the strain at  $15^\circ$  of the disc. While strain gauge 2 at  $45^\circ$  and strain gauge 3 at  $75^\circ$ . The strains around the entire disc could thus be measured by rotating the disc a full revolution ( $360^\circ$ ) until the strains in all the required orientations of the disc were measured for all three strain gauges. The strains were measured in smaller angle intervals of  $15^\circ$  on the disc near the disc/pad contact interface as this was expected to be the region where the strains were concentrated and the strain magnitudes would vary significantly, while the region away from the disc/pad interface was measured at a spacing of  $30^\circ$  as it was

predicted that the strains would not change significantly at the positions away from the pad disc interface. The test was completed at four different pneumatic chamber pressures, namely: 1 bar, 2 bar, 4 bar, and 6 bar; for all the required disc orientations. Referring to the Load Cell Test (Section 4.1), these pressures are equivalent to pad clamping forces of 11 kN, 24.6 kN, 50.4 kN, and 77.4 kN, respectively.

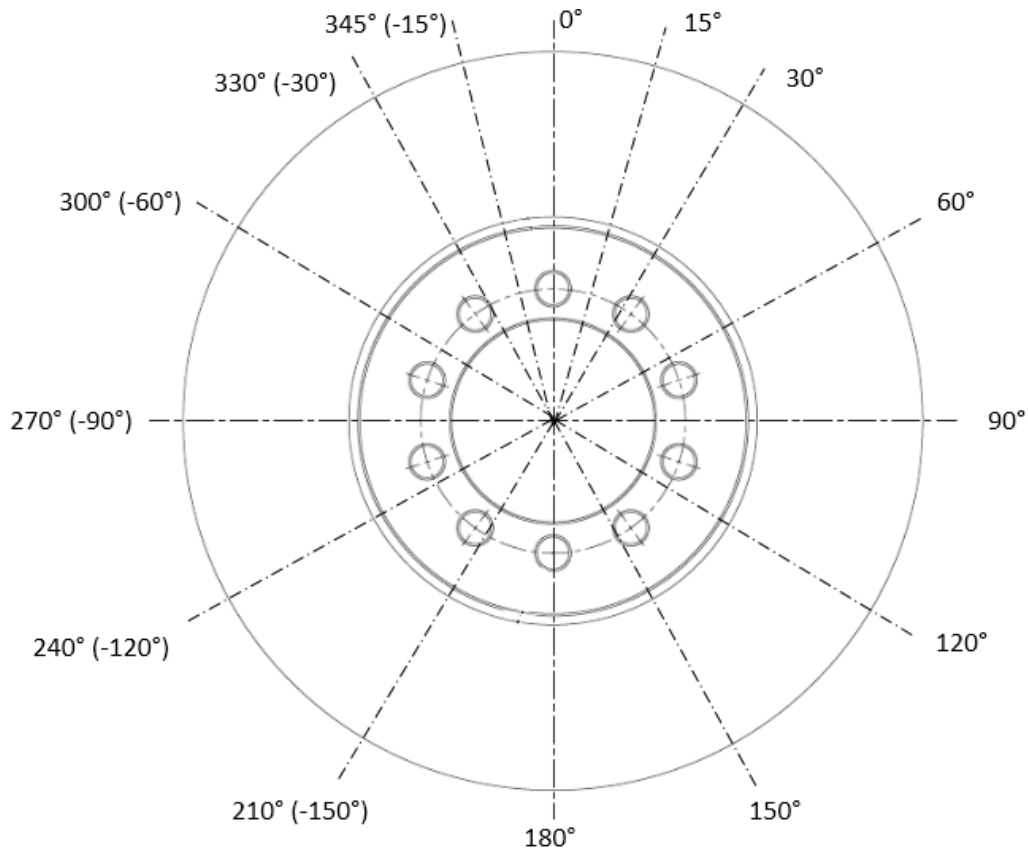


Figure 20: Disc orientation coordinates (outboard face view)

### 3.4.2 Torque Load Test

For the torque load test the shaft torque (hence disc braking torque) was monitored by measuring the strain obtained by strain gauges directly installed on the shaft. Two pairs of biaxial 0°/90° stacked rosettes orientated at 45° to the longitudinal direction of the shaft were bonded to the shaft, on diametrically opposite sides of the shaft. Refer to Table 6 for the torque strain gauge properties. The two rosettes were wired together as an active full-bridge system for torque measurement. The leadwires of the rosettes were connected to the SCXI DAQ and the strains were recorded using LabVIEW.

For the torque load test, it was ultimately desired to measure the strains on the disc on the surface that makes contact with the brake pads. However, as discussed in the Literature Review (Section 2.3.4) it is currently impossible to experimentally measure the dynamic interface pressure distribution (between pad and disc) or the strains in this area. Strain gauges installed between the disc/pad contact interface would be crushed. Therefore, the strains were measured as close as possible to the contact interface without damaging the equipment. Uniaxial strain gauges were installed on the face of the brake disc directly below the outboard pad contact interface. The strain gauge properties are shown in Table 6. The strains were sampled at 1000 Hz.

The strains due to the applied brake torque were measured using eight uniaxial strain gauges installed on the disc outboard face, as shown in Figure 21, labelled strain gauge 1 to strain gauge 8. A pair of strain gauges were installed on each of the radial lines as indicated by the white lines in Figure 21. The radial lines on which the strain gauges were mounted were separated by multiples of  $15^\circ$  from one another. The uniaxial strain gauges were positioned at two different radii on the disc, one upper location (above the ridge/recess) and one lower location (below the ridge/recess), as shown in Figure 22. Two strain gauges were mounted at  $0^\circ$  to the radial line, four at  $45^\circ$  and, two at  $90^\circ$ . By rotating the disc, strains at  $0^\circ$ ,  $45^\circ$  and  $90^\circ$  orientation could be measured at the same point. Ideally, strain rosettes would have been used with all three strain gauges in a single location on one radial line (refer to Figure 23 and 24), however, the surface that the strain gauges could be installed was constrained to the narrow region between the disc hub and directly below the brake pads. This ensured that the strain gauges would not be damaged under the braking action. Therefore, it was required to split the uniaxial strain gauges over different radial lines. Refer to Table 7 and Figure 22 for the orientations of each of the installed strain gauge, and the radial distance between each of the strain gauges to the disc circumference. Referring to Figure 20 for the disc orientation coordinates tested for the clamping load test, the torque load test was completed at all the disc coordinates indicated on the figure, with the additional positions of  $45^\circ$ ,  $75^\circ$ ,  $285^\circ$  (or  $-75^\circ$ ), and  $315^\circ$  (or  $-45^\circ$ ). Similar to the clamping load test, the disc was rotated  $15^\circ$  when the strain gauges were near the brake pad and  $30^\circ$  when away from the pad which enabled the strain gauges to measure the strains around the entire disc.



A suitably large braking pressure was applied to the disc to ensure that the brake disc would not rotate under the maximum applied torque (approximately 1030 Nm). The torque was applied in a counter-clockwise direction as viewed from the outboard standpoint. A pneumatic chamber pressure of 4 bar (equivalent to a pad clamping force of 50.4 kN) was sufficient to stop the disc from rotating. Thereafter, the torque was applied to the disc and the strains were measured at all disc orientations.



Figure 21: Eight uniaxial strain gauges installed for applied torque load test (SG: strain gauge)

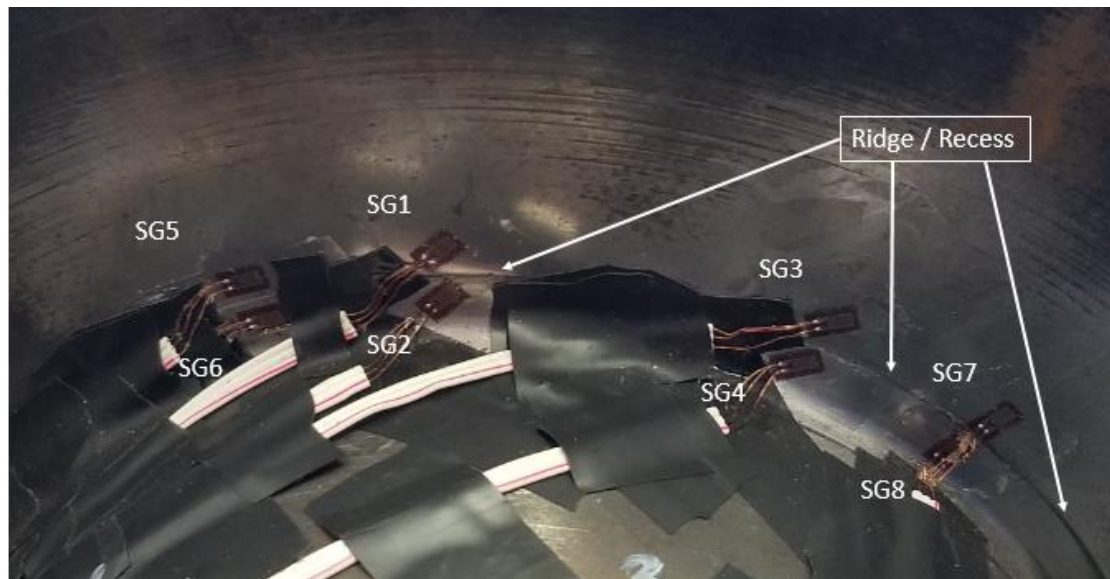


Figure 22: Different orientation of the strain gauges for the applied torque load test

Table 7: Strain gauge positions for applied torque test

Strain Gauge	Above or Below Recess	Orientation on Radial line	Radial Distance to Disc Circumference
1	Above	45°	71 mm
2	Below	45°	79 mm
3	Above	45°	71 mm
4	Below	45°	79 mm
5	Above	0°	71.5 mm
6	Below	0°	79 mm
7	Above	90°	71 mm
8	Below	90°	78.5 mm

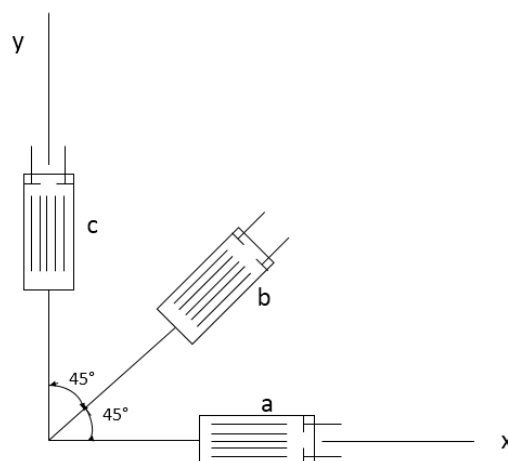


Figure 23: Configuration of a 45° strain rosette with three strain gauges

Two pairs of strain gauges (with each pair on a different radial line 30° apart) were utilised to measure the normal strains in the 45° orientation on the disc. The pairs were denoted as

strain gauge 1 and 2, and strain gauge 3 and 4. These two pairs of strain gauges were utilised to ensure repeatability of the measured strains. Refer to the section Repeatability of the Uniaxial Strain Gauges Orientated at  $45^\circ$  (Section 4.4) for the detailed analysis of the repeatability of the strain results from these four strain gauges. Strain gauge 1 and 3, and strain gauge 2 and 4 were measuring identical positions respectively; and it was observed that the two pairs of strain gauges when compared produced repeatable results.

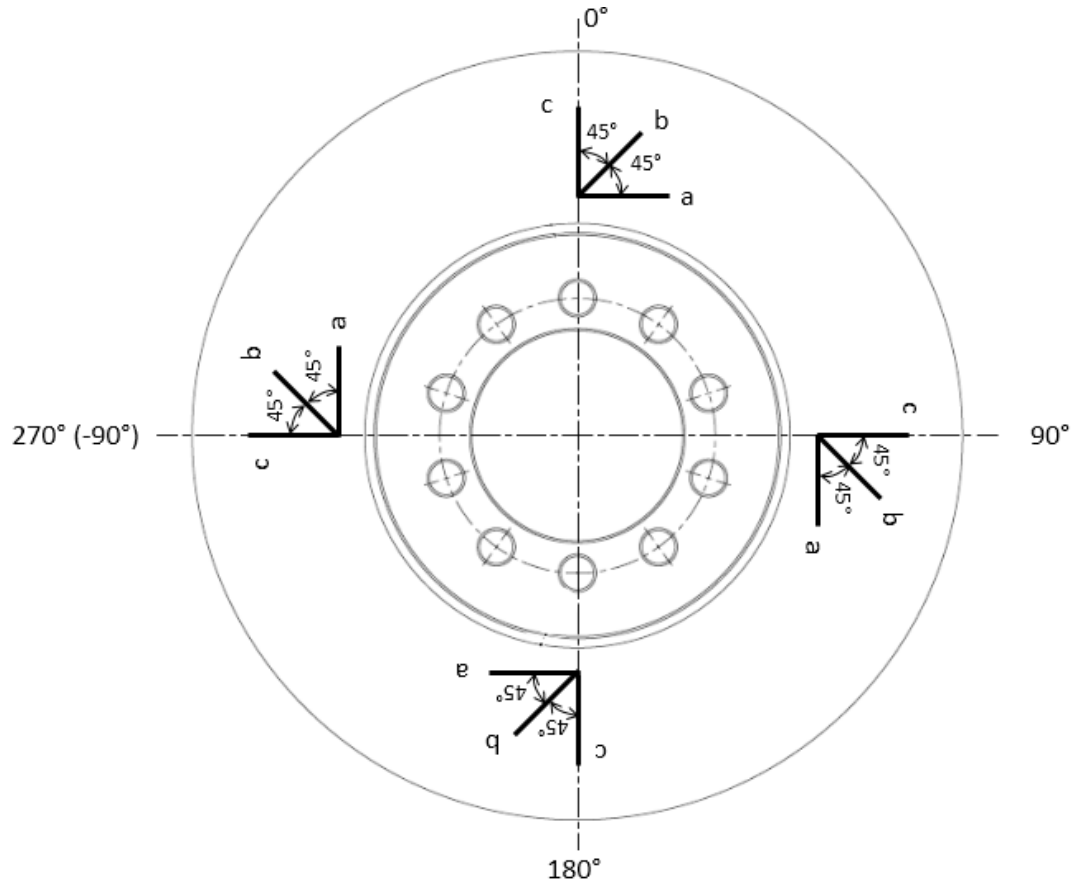


Figure 24: Rotating strain gauge coordinate system relative to disc coordinates

### 3.5. Measurement Uncertainty Analysis

An uncertainty analysis evaluates the factors that influence the accuracy of the results. Refer to Appendix A (Section A.1) for the full details of the measurement uncertainty analysis. A summary of the analysis follows.

The accuracy of each of the system components needs to be calculated before the overall system accuracy can be determined. Frequently, it is useful to calculate the absolute accuracy relative to the input (RTI), which provides a more respective comparison. The

absolute accuracy RTI calculated for the SCXI-1520 and SCXI-1600 devices were  $\pm 0.07\%$  and  $\pm 0.036\%$ , respectively. The absolute system accuracy RTI represents the end-to-end accuracy of the signal conditioning and data acquisition device, which was calculated to be  $\pm 0.079\%$ .

The root sum squares (RSS) method was used to calculate the propagation of uncertainty for the entire strain measuring system (the strain gauges and the DAQ). The strain uncertainty  $\Delta\varepsilon$  was calculated using equation 1. The supply voltage,  $V_s$  and bridge output voltage,  $V_0$  relate to the accuracy of the Wheatstone bridge circuit. The third term relates to the accuracy of the strain gauge. Refer to Appendix A for the partial derivatives. For the highest measured strain, the strain uncertainty being expressed as a percentage,  $\Delta\varepsilon/\varepsilon$ , was calculated to be 1%.

$$\Delta\varepsilon = \sqrt{\left(\frac{\partial\varepsilon}{\partial V_0}\Delta V_0\right)^2 + \left(\frac{\partial\varepsilon}{\partial V_s}\Delta V_s\right)^2 + \left(\frac{\partial\varepsilon}{\partial k}\Delta k\right)^2} \quad (1)$$

A second method of characterising the accuracy of the experiment was used to compare to the RSS method. The second method applied 6 bar brake pressure on the disc, and recorded the strain values at the  $0^\circ$  disc orientation. This was repeated five times at the same location. Ideally these five measurements should be equal, however, slightly different strain readings do occur. The accuracy of the measurements can be characterised using the standard deviation of the five strain readings. This was performed for each strain gauge. Averaging the uncertainty values across the three strain gauges and across all pressures resulted in an uncertainty of 1.41%. Comparison of the uncertainty calculated based on the RSS method and the standard deviation method shows good agreement.

## **4. CALIBRATION, VERIFICATION, AND PRELIMINARY TESTS**

### **4.1. Load Cell Test**

An initial load cell test was performed to determine the relationship between the pneumatic chamber pressures to the clamping forces applied by the brake pads i.e. this was to characterise the clamping forces for each bar of pneumatic pressure being applied. An HBM U9C load cell rated at 50 kN was utilised for the test.

A pair of commercially available brake pads were modified for the load cell test. The friction material of both of the pads were removed revealing the face of the steel backing plates. Thereafter, a thin layer on the steel face of the plates was machined off in order to remove all the friction material thoroughly revealing the steel material only, in addition to obtaining a uniform and flat surface. Additionally, the centre of the inboard pad was machined a further 2 mm as there was excess friction material embedded near the surface of the plate. It was important to remove all the friction material (brittle material) on both pads such that the load cell was pressing against the metal material only. A hole was drilled at the centre of each of the brake pads such that the load cell can be accurately located and secured between the brake pads. The load cell mimicked the brake disc, which was sandwiched between the pads. The load cell test configuration is shown in Figure 25.

It was important to ensure that the load cell nuts were adjusted accordingly on the threads such that the load cell did not protrude past the back face of the backing plates. This ensured that the brake caliper piston pushed against the inboard pad, and not directly against the load cell. Thus, the load cell only makes contact with the pad. Similarly, on the opposite end, it was required that the load cell pushed against the outboard pad, and not on the caliper directly. An additional nut was used on each end of the load cell to lock it into position.

The test was completed from 0 to 4 bars in increments of 0.5 bars. For each of the pressures tested, the load cell forces were recorded over a 10 second period at a sampling rate of 1000 Hz. An average was calculated over the period to reduce the effects of noise. The load cell test was repeated three times and the final values were calculated based on the averages of the three tests for each of the pressures. The results for the load cell test are

shown in Figure 26, where the clamping forces are plotted against each of the pneumatic chamber pressures, from 0.5 to 4 bar.

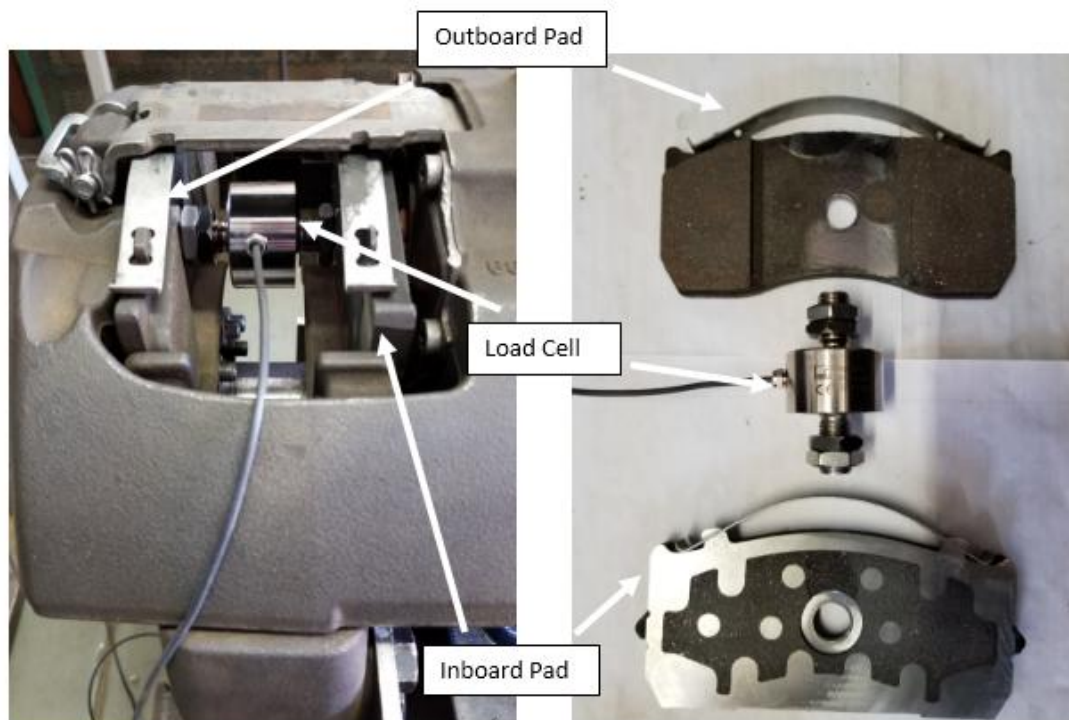


Figure 25: Load cell test configuration with the load cell slotted between the two brake pads

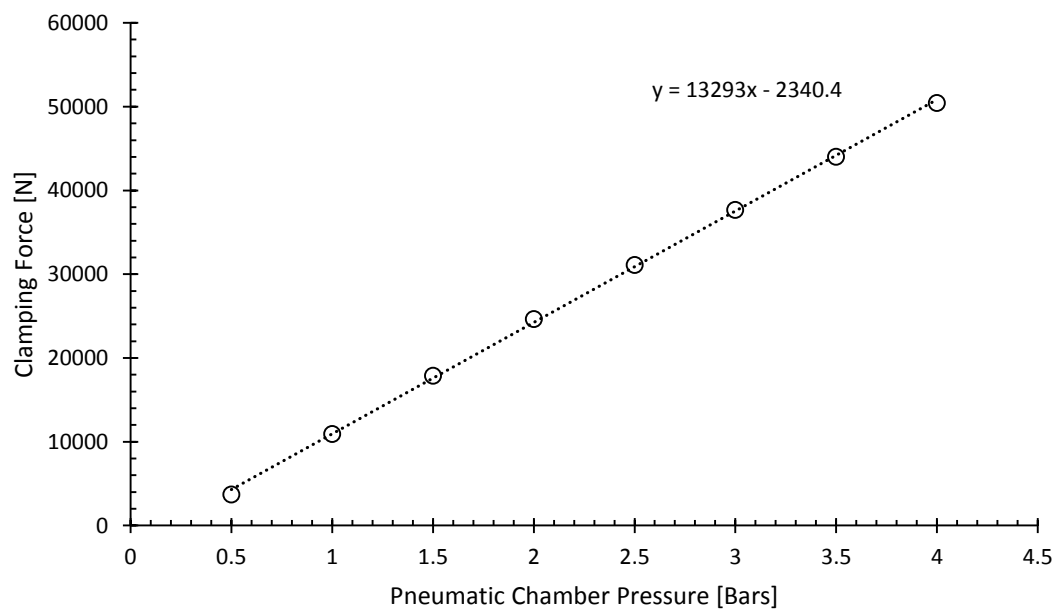


Figure 26: Clamping force and pneumatic chamber pressure relationship as per load cell test

Referring to Figure 26, the minimum clamping force was 3.72 kN at 0.5 bar of pneumatic chamber pressure, whilst the maximum clamping force was 50.4 kN at 4 bar of pneumatic chamber pressure. Refer to Table A-3 in Appendix A for the exact clamping force values for each of the pneumatic chamber pressures. The data exhibited a linear relationship, as seen from the linear trendline fitted through all the plotted data points with the trendline equation shown in Figure 26. Since the load cell was rated at 50 kN, it was not ideal to exert a pneumatic chamber pressure greater than 4 bar, as it risked damaging the load cell. For the clamping load test, the brake disc needs to be tested to 6 bar. The linear relationship between clamping force and pneumatic chamber pressure, as shown in Figure 26, was assumed to hold true at these higher pressures as well. The justification is that for the linear regression, the coefficient of determination equals 0.999. Additionally, the maximum operating pressure of the brake chamber is approximately 10 bar. Therefore, at 6 bar, it is not near the extremes where the linearity may be difficult to justify. The clamping forces for 5 bar and 6 bar of pneumatic chamber pressures were extrapolated from the linear trendline equation to be 64.1 kN and 77.4 kN, respectively. The threshold pressure of the pneumatic chamber was obtained by calculating the x-intercept of the trendline equation, which was 0.18 bar.

#### **4.2. Torque Calibration Test**

The braking torque measured by the pair of biaxial strain gauges on the shaft were vital measurements, and as such it was essential that the braking torque be accurately measured. A physical calibration with calibrated weights was performed to validate that the applied torque equalled the torque recorded by the strain gauges (after signal processing of the strains through the data acquisition devices). Refer to Appendix A (Section A.3) for the full details of the torque calibration test. A summary of the calibration results follows.

Referring to Figure 27, the torque calibration test rig consisted of one end of a flat bar bolted to the brake disc on the flange bolts. A mass hanger was attached to the other end of the flat bar for the placement of slotted calibration weights. The lever arm setup enabled the torque to act through the centre of the shaft. In total, four calibration weights were used to perform the torque calibration. The measured torque values calculated from the strain gauge readings were compared to the applied calibration weight torques. The difference between the two values displayed a trend of decreasing differences from a 10.7% difference

at the smallest calibration weight to a 6.2% difference at the highest calibration weight as seen in Table A-6 in Appendix A. This exhibits good agreement between the known applied calibration torque and the experimentally measured torque, whereby it can be concluded that the accuracy of the torque measured using the strain gauges was acceptable for the range test.

The calibration torque was approximately 10% of the torque applied during testing. The calibration test was not performed for the full range of torque, because applying 1000 Nm of torque through the lever arm required a calibrated weight in excess of 203 kg. A calibrated weight of this magnitude was not readily available within the provided resources, and was not financially feasible to obtain. The torque measurement strain gauges were manufactured from a trusted reputable brand (Kyowa) and was expected to provide accurate torque readings, as it is the standard of measuring torsion. The calibration test served to provide reassurance that the measurement system was fully operational and correctly assembled, and that the torque readings were accurate. Therefore, although the calibration process was not performed for the full range of torque; for the torques that were performed it exhibited good agreement between the known applied calibration torque and the experimentally measured torque. Considering all the factors, it was assumed that the torque measurement system would unlikely deviate significantly at the higher torques.



Figure 27: Mass hanger with calibration weights applying torque to the shaft through a flat bar



### **4.3. Effect of Static Torque on Brake Disc Compressive Strains**

The first phase of experimental testing applied static clamping brake loads on the brake disc, where the disc did not rotate. This isolated the applied loading by the pads on the brake disc to clamping only; no torque loading was applied to the disc.

The second phase of experimental testing replicated a representative braking action which included both a braking torque and clamping load. Due to the tight space tolerances between the brake caliper and disc, during the applied torque load test it was not possible to retain the uniaxial strain gauges that were used to measure the compressive strains on the disc core as the strain gauge wires would have been damaged with rotation of the brake disc.

A test was performed prior to the applied torque load test to determine whether the compressive strains experienced by the disc during the static clamping brake loading would differ, if a known static torque was applied in addition to the same clamping load. This would indicate whether the uniaxial strain gauges on the disc core were required for the applied torque load test.

The procedure consisted of two separate tests conducted at the same position on the brake disc. Firstly, the compressive strains on the disc were measured with the clamping action applied by the brake pads on the static disc. This was repeated twice to minimise any influence due to noise.

For the second part of the procedure, the compressive strains were measured with the brakes applied, but with the addition of approximately 100 Nm of torque being applied statically (non-rotating disc) through the shaft using a lever arm and calibration weights as described in the Torque Calibration Test (Section 4.2). This was repeated twice and the averaged value was used. This procedure was performed at a braking load of 2 bar and 4 bar pneumatic chamber pressures. The uniaxial strain gauge was positioned at 7.5° counter-clockwise from the zero reference on the brake disc. The measured compressive strain results for the test are shown in Table 8, and the percentage changes of the measured strains between the test with torque and without torque are shown in Table 9.

Table 8: Brake disc compressive strains with, and without calibration torque load

	Compressive Strain [ $\mu\epsilon$ ]		
	Without Torque		With Torque
	Test 1	Test 2	Test 3
2 bar	-30.5	-31.1	-31.89
4 bar	-74.5	-74.8	-75.88

Table 9: Percentage change comparing compressive strains without applied torque to with applied torque

	Percentage Change [%]	
	Test 1	Test 2
2 bar	4.6	2.6
4 bar	1.8	1.5

Referring to the compressive strains in Table 8 for the static compressive loading without applied torque, at 2 bar pneumatic brake chamber pressure, test 1 recorded a strain  $-30.5 \mu\epsilon$  and test 2 was  $-31.1 \mu\epsilon$ . At the same position and with identical braking pressure but with the addition of 100 Nm of applied torque, the compressive strain was  $-31.89 \mu\epsilon$  for test 3. Referring to Table 9, the addition of the applied static torque (test 3) translated to a percentage change of the compressive strain of 4.6% when compared to test 1 and 2.6% when compared to test 2. The results for the 4 bar pneumatic brake chamber pressure yielded strains of  $-74.5 \mu\epsilon$  for test 1 and  $-74.8 \mu\epsilon$  for test 2. The compressive strain measured for test 3 with the applied torque was  $-75.88 \mu\epsilon$ . This represented a 1.8% strain change when compared to test 1 and 1.5% strain change when compared to test 2. The compressive strain differed by approximately 1 to  $1.5 \mu\epsilon$  when a static torque was applied in addition to the compressive loading. This is considered negligible considering the Measurement Uncertainty Analysis (Section 3.5)

The results indicate that it is acceptable to assume that the compressive strains for the clamping-only loading are equal to the compressive strains from the combined loading (clamping and applied torque) test. The compressive strains remained relatively unchanged under applied static torque load. This allowed the applied torque load test to be performed without the need to measure the compressive strains with the uniaxial strain gauges as the compressive strains would be equal to those from the clamping loading at the same positions. Only the disc face strains (hence shear stresses) were required to be actively measured for the applied torque load test.

#### **4.4. Repeatability of the Uniaxial Strain Gauges Orientated at 45° for the Torque Load Test**

For the torque load tests, two pairs of strain gauges (strain gauge 1 and 2; strain gauge 3 and 4) were utilised to measure the strains at the 45° orientation around the brake disc face. The two pairs of strain gauges were placed on two different radial lines (30° apart) to ensure repeatability of the strain values being measured, as the strains at this 45° orientation are vital in the processing of the shear strains ( $\gamma$ ) and the shear stresses ( $\tau$ ). For the test a constant pneumatic chamber pressure of 4 bar (equivalent to a pad clamping force of 50.4 kN) was first applied to the brake disc, thereafter an applied torque load of 1005 Nm was applied to the disc. Strain gauge 1 and strain gauge 3 (upper location strain gauges) essentially measured the strains at the same positions on the brake disc at each of the disc orientation angles. The strain results from both strain gauges are plotted on the same set of axes for comparison, as shown in Figure 28.

Referring to Figure 28, the trends are nearly identical for the two strain gauges. When comparing the strains between the two strain gauges at the positions away from the disc/pad contact interface (between -75° to -180° and 75° to 180°) the values between the gauges were very similar, with the differences between them in the range of between 0.5  $\mu\epsilon$  to 0.9  $\mu\epsilon$ . This can be considered negligible when considering the propagation of error of strain gauges which was discussed in detail in the Measurement Uncertainty Analysis (Section 3.5). There were moderate differences between the two strain gauge values at a few of the positions in the vicinity of the disc/pad interface (between -30° to 30°), with the differences in the range of 4  $\mu\epsilon$ . These locations with the larger differences coincided with the points where the gradients of the graph were the steepest. The positions around the brake disc were marked using a scribe and the centre position of the pad was marked using a white marker. Each of the brake disc orientations were rotated and selected by aligning the scribed line on the disc with the centre position mark on the pad. Therefore, the slightest misalignment between these lines propagated into large differences in the regions of the steeper gradients. Considering these factors, it was acceptable to conclude that the strain results were repeatable for strain gauge 1 and strain gauge 3.

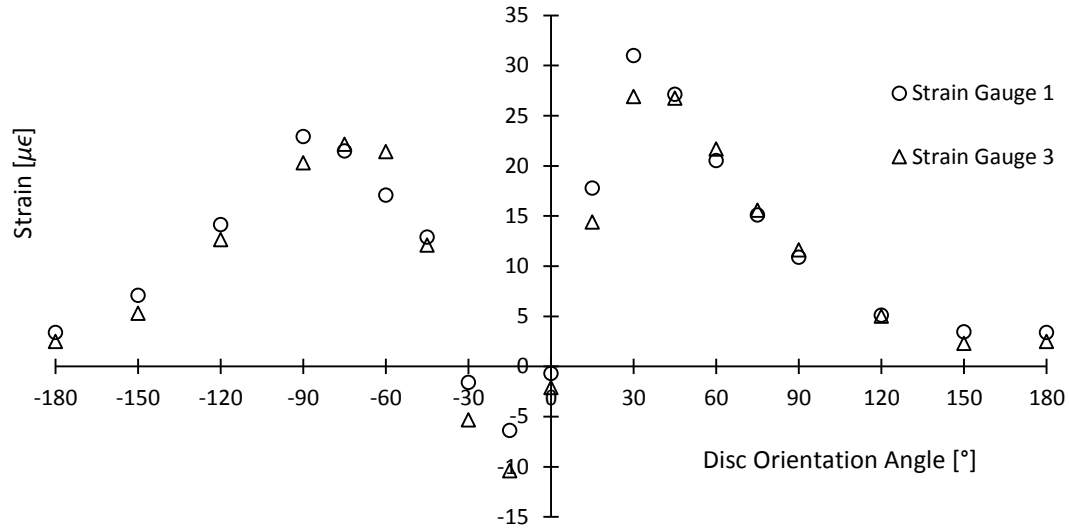


Figure 28: Measured strains from the upper location strain gauges in the 45° orientation

Similarly, the strain results for the lower location strain gauges, strain gauge 2 and strain gauge 4 were plotted on the same set of axes, as shown in Figure 29. Strain gauge 2 and strain gauge 4 were measuring the strain at the same position at each of the disc orientation angles.

Referring to Figure 29, the trends of the strain values for the two strain gauges were identical. Similar to the results for strain gauge 1 and 3 when comparing the strains between the two strain gauges, the values away from the disc/pad contact interface were similar with small differences in the range of between 0.1  $\mu\epsilon$  to 3  $\mu\epsilon$ . There were also a few points with slightly larger differences between the strain values which were measured at the identical positions, but as explained previously, these were at the positions of the steepest gradient on the plots. Therefore, both the trends and values of strain gauge 2 and 4 were deemed repeatable. Thus, the two pairs of strain gauges (1,2 and 3,4) when compared produced repeatable results, and as such during the processing of the strain results to stress values it was possible to process the rosette using either strain gauge 1 and 2 or strain gauge 3 and 4 as the 45° orientation gauges, as either pair would produce similar stress results.

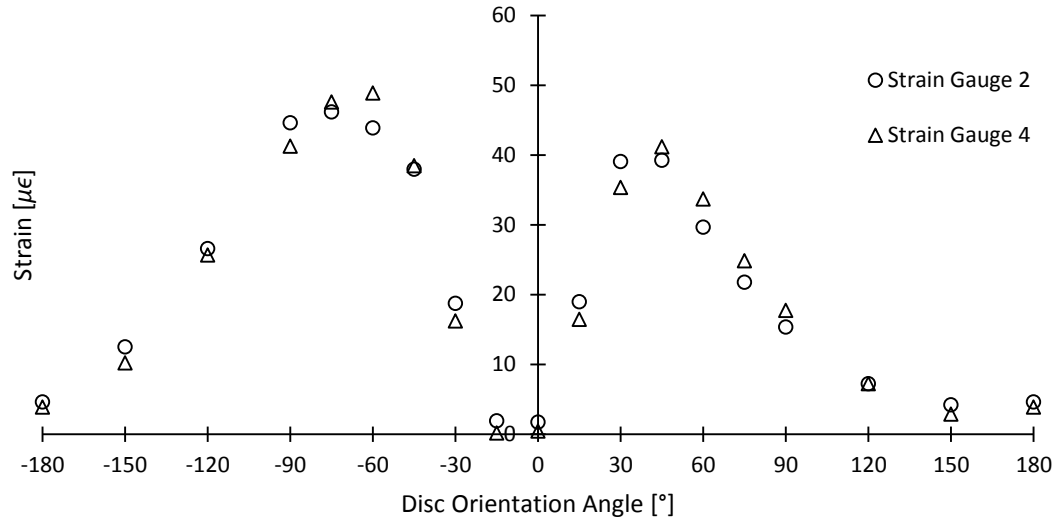


Figure 29: Measured strains from the lower location strain gauges in the 45° orientation

#### 4.5. Linearity of Applied Torque versus Shear Strain

A constant 4 bar pneumatic chamber pressure (equivalent to a pad clamping force of 50.4 kN) was first applied to the brake disc, thereafter a range of torques from 530 Nm to 1030 Nm were applied to the disc through the motor. The high brake pressure value was selected to ensure that no rotation of the brake disc occurred during the application of the entire range of torques. The strains on the brake disc due to the different applied torques were recorded using the SCXI DAQ devices and LabVIEW. The shaft torque (hence braking torque) was measured using the two pairs of biaxial strain gauges. The shaft material properties and equations converting the measured strain to torque can be found under the Torque Calibration Test (Section 4.2). The test was performed at the 0° position of the brake disc and at the 30° position. All four strain gauges were used to measure the strains at these two positions to evaluate the repeatability. The orientations were achieved by manually rotating the disc to the required positions.

Figure 30 shows the strains experienced by the disc at the applied torques. The results are for strain gauge 1 and strain gauge 2 in the 0° disc orientation position, and for strain gauge 3 and strain gauge 4 in the 30° position. The strain results measured using strain gauge 1 and strain gauge 2 at 0° are close to zero. This indicates that the 45° normal strains experienced directly below the disc/pad contact interface on the same radial line as the central position

of the interface are negligible when loaded by various torques. These results were repeatable and confirmed using strain gauge 3 and strain gauge 4 at the same position (0°).

The test was additionally performed at the 30° disc position, due to the test at the 0° position yielding minimal strain response.

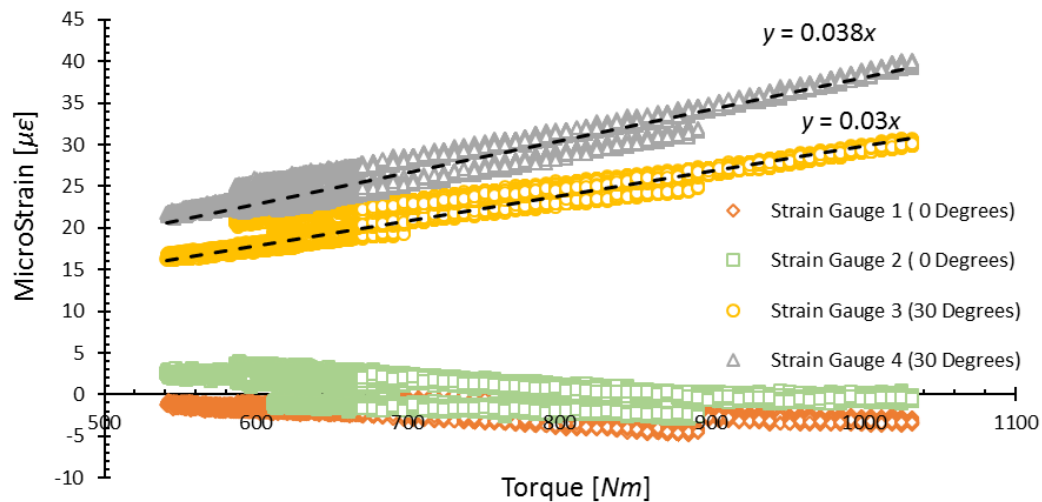


Figure 30: Strain measured by strain gauge 1 to 4 under various applied torque loads

The results from the 30° position are shown by strain gauge 3 and strain gauge 4 in Figure 30. A linear regression line was fitted to the results for both strain gauge 3 and strain gauge 4. For the initial regression lines, the y-intercept of strain gauge 3 was  $2.1 \mu\epsilon$  and for strain gauge 4 it was  $1.7 \mu\epsilon$ . The small strain offset was due to system noise since it was within the same fluctuation range previously of that of strain gauge 1 and 2 at 0°. New regression lines were processed to set the y-intercept to zero (0). This would be physically valid as zero applied torque should generate zero strain on the disc. The new linear regression line for strain gauge 3 was  $y = 0.030x$ . For strain gauge 4:  $y = 0.038x$ . The results for both strain gauge 3 and strain gauge 4 exhibited a linear relationship between the strain experienced by the brake disc and the applied torque values, where an increase in torque results in an increase in strain.

There was repeatability of the strain gauge 3 and strain gauge 4 results as the linear relationship was confirmed by the results of a separate linear test at the same position (30°) by strain gauge 1 and strain gauge 2, respectively. The linear regression line for strain

gauge 1 was  $y = 0.030x$  and for strain gauge 2 was  $y = 0.038x$ . Therefore, there was repeatability of the linear test results.

#### **4.6. Discretisation of Torque**

The maximum torque value applied to the disc that was common at all the tested positions around the disc was 1005 Nm. Several hundred strain readings were recorded by the strain gauges at this specific applied torque for each of the tested positions of the brake disc, where an average value was then calculated which aimed to minimise the uncertainty. It was noted that the measured applied torque values varied between discrete values of 998 Nm to 1005 Nm (with a few locations at 1011 Nm) near the maximum torque range. This pattern was repeated for every test. It was required to determine whether the “jumps” between the discrete values were due to the discretisation of the analog-to-digital converter (ADC) in the data acquisition (DAQ) hardware. From the Torque Calibration (Section 4.2), the above jumps in torque were determined to be jumps of 3 mV in the torque signal.

The National Instruments SCXI-1600 DAQ module has a 16-bit ADC. It was used for the data acquisition for the main experimental applied torque load tests which spanned a range of 0 to 3 V. Therefore, 3 V divided by 65536 bits equates to  $45.8 (10^{-3})$  mV per bit. Therefore, the 3 mV fluctuations spanned 65.5 bits. Thus the fluctuations are significantly larger than the resolution of the ADC, hence the “jump” in the applied torque values were not due to the discretisation of the bits of the ADC in the DAQ. The variable speed drive was determined to be the reason for maintaining the torque at these discrete values before step changing to the next torque.

## **5. RESULTS AND DISCUSSION**

### **5.1. Overview**

The results of the experimental clamping load test for the solid brake disc are presented and discussed in Section 5.2. The results for the experimental applied brake torque load test for the solid brake disc are presented and discussed in Section 5.3. The solid brake disc stress distribution results for the clamping load and the applied torque load were applied to the design of the reinforcement of the WBD brake disc core in Section 5.4.

### **5.2. Experimental Clamping Load Test**

The experimental clamping load test for the solid brake disc was conducted at four compressive loads; at 1, 2, 4, and 6 bar pneumatic chamber pressures, which translated to applied pad compressive forces of 11.0 kN, 24.6 kN, 50.4 kN, and 77.4 kN, respectively. The normal strains experienced in the disc core around the circumference of the brake disc due to the clamping loads were measured. It was previously stated in the Literature (Section 2.4.3) that for the contact interface on the pad that most of the higher contact pressures were located at the outer boarder regions of the pad (which was shown in Figure 13). This provided the motivation to measure the strains (hence stresses) on the circumference of the brake disc, as it was expected to be the region with the greatest contact pressure, hence should provide the maximum strains and stresses.

Three strain gauges were installed (30° radially apart) to evaluate the repeatability. When compared, the trends of the measured strain results for all three strain gauges were very similar for all the orientation locations tested around the disc circumference, indicating the results were repeatable. The magnitude of the strain results measured by strain gauge 2 at the -15° and 0° disc orientation locations were slightly larger than those of strain gauge 1 and strain gauge 3. The -15° and 0° orientations were retested but yielded the same results, therefore the different results were deemed not to be due to an error in measurement. The disc was skimmed prior to testing and as such the disc thickness was uniform, therefore the possibility of a non-uniformity on the disc surface was minimised. The discrepancy at these two orientations (-15° and 0°) for strain gauge 2 were in close proximity of each other. The strains measured by strain gauge 3 was selected as the best representation of the results for



the clamping load test (shown in Figure 31). The strain results for strain gauge 1 and strain gauge 2 are shown in Figure C-1 and Figure C-2, respectively, in Appendix C. The negative strains indicate compression and the positive strains for tension.

The strain results at the 0° (zero degree) position on the plots as shown in Figure 31 are of high importance as the vertical 0° disc radial line coincides with the pad geometric centre-line when the two components are in contact during the braking action, and consequently this was the centre-line of the disc/pad contact interface. For the various applied clamping loads, the disc strains were fairly symmetrical about the 0° vertical centre-line which represents a near uniform and equal distribution of the strains on either sides of the centre-line, and hence the disc/pad contact interface. This may be additionally extended as an indication of a near symmetrical distribution of the pad forces applied through by the caliper piston. According to Abu Bakar et al. [38] the symmetric interface pressure distribution about the geometric centre-line of the pad is an indication of a favourable pressure distribution as this would reduce uneven pad wear and brake squeal.

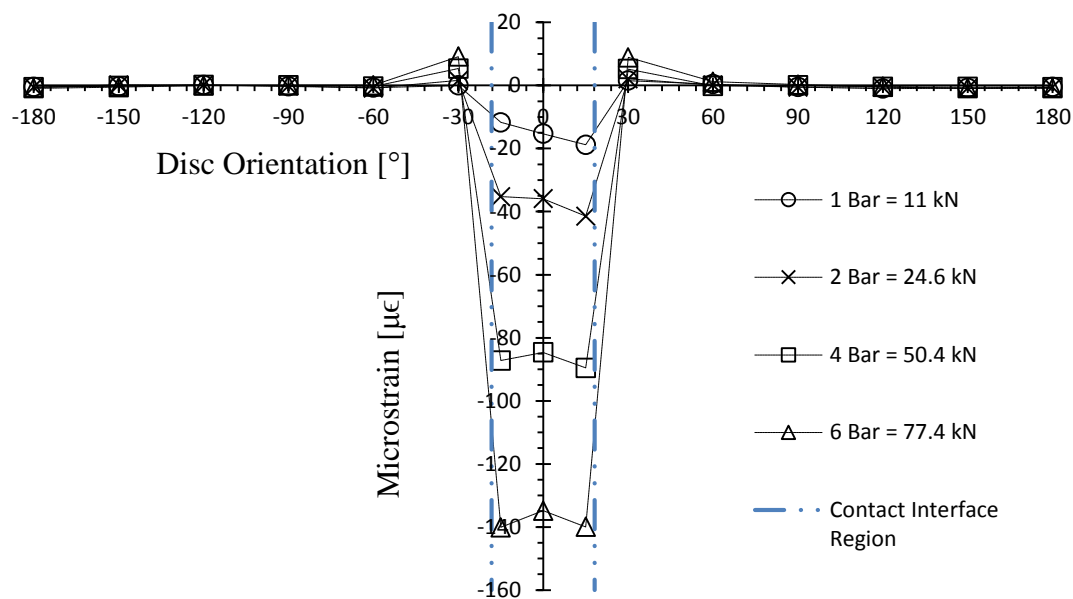


Figure 31: Normal strains on the solid disc core measured by strain gauge 3 during the clamping load test

The mechanical stresses due to a typical brake disc set-up are well below the strength of typical brake disc materials like grey cast iron and steel. Therefore, it is reasonable to assume that the solid disc stress and strains are within the elastic region and that the material behaves elastically, such that Hooke's law can be applied. The modulus of elasticity

for the solid brake disc was  $E = 120 \text{ GPa}$ . The strain results measured by strain gauge 3 were used to process and obtain the stress distribution of the solid brake disc under various applied clamping loads, as shown in Figure 32. The stress distribution processed using the strain results from strain gauge 1 and strain gauge 2 are shown in Figure C-3 and Figure C-4 in Appendix C.

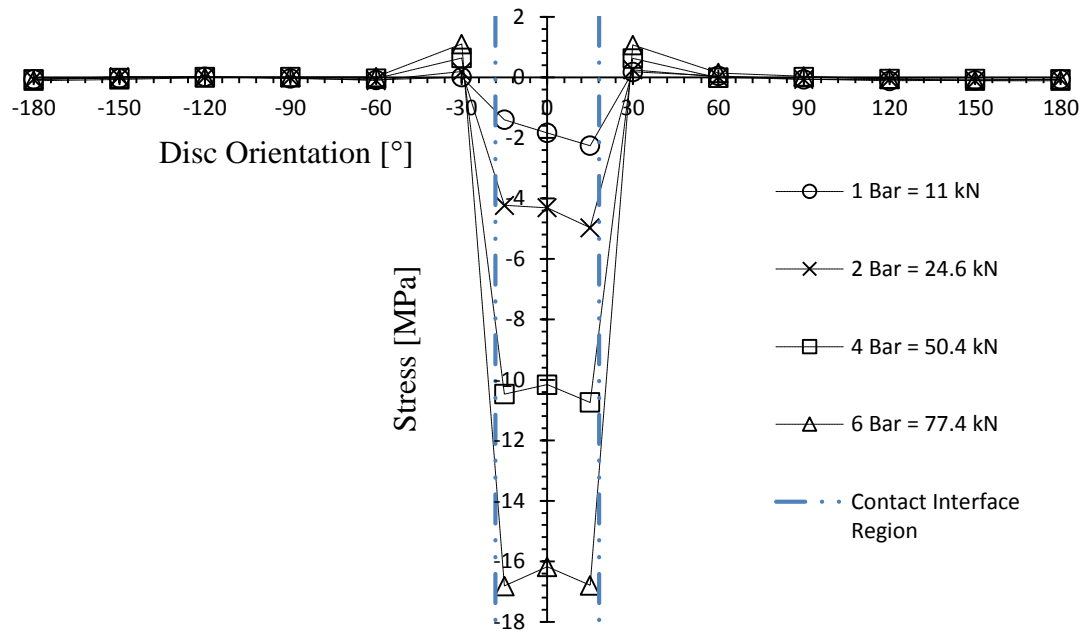


Figure 32: Stress distribution around solid disc circumference due to applied clamping loads

The nature of the surface topography of the pads results in a contact interface area that is less than the apparent contact area (geometric area) of the pad, as full contact is not achieved between pad and disc. Extensive research in the literature has investigated the factors that affect the actual contact area to the apparent contact area. This research focuses on the distribution of the stresses on the brake disc relative to the contact interface region. This will provide insight into how the applied pad forces are transferred through to the brake disc. The dimensions of the brake pads used for the experimental testing are shown in Figure C-5 in Appendix C. It is important to note that the brake pad material on the two chamfer areas did not make contact with the brake disc, as the pads were in brand new condition.

The diameter of the brake disc was 334 mm. Therefore, the disc circumference was equal to 1049.3 mm. The pad was inserted into position in the caliper where the top arc length of the pad friction material (indicated with the dimension of 106 mm in Figure C-5) was flush with

the top circumferential portion of the disc, which formed the outer boarder of the contacting region; as shown in Figure 33. Therefore, the ratio of the pad arc length to the disc circumference was 10.1%. This ratio converted to a central angle of  $36.4^\circ$  on the disc. This was important as it signified that the contacting interface between the top region of the pad with the disc accounted for a disc central angle of  $36.4^\circ$ . This angle is indicated as  $\alpha$  on Figure 33. This angle was additionally indicated in Figure 31 and Figure 32 as the “Contact Interface Region” which was denoted as the region between the two vertical dashed lines (with  $18.2^\circ$  split on each side of the  $0^\circ$  disc coordinate). This allowed the direct comparison of the distribution of disc strains with the contact interface. Referring to Figure 32, it was evident that the highest compressive stresses experienced in the disc were concentrated within the region of the disc/pad contact interface as all of the significant stress data points were within the indicated “Contact Interface Region” of between  $-18.2^\circ$  to  $18.2^\circ$ . The stresses then rapidly declined when shifting out of the contacting interface region. This can be seen in Figure 32 where the stress magnitudes of the discrete data points at  $-15^\circ$ ,  $0^\circ$ , and  $15^\circ$  maintained a relatively constant stress level with small differences between the values. However, when traversing from  $-15^\circ$  to  $-30^\circ$  and similarly from  $15^\circ$  to  $30^\circ$ , there was a rapid decline in the stress values. The results reveal that the bulk of the compressive stresses experienced by the brake disc was confined to the disc/pad contacting area of the disc.

It was necessary to determine the extent to which the bottom region of the pad reaches on the disc contact, as it will influence the distribution of stresses on the disc. Therefore, it was required that the central angle that encompasses the two lower edges of the pad be determined. Using the pad dimensions from Figure C-5 and the disc dimensions, the central angle was calculated as  $\beta = 78.2^\circ$ , as shown in Figure 33. Referring to Figure 11 and Figure 13 in the Literature Review (Section 2.4), previous studies determined the contact pressure in the vicinity of the bottom region on both of the side edges of the pad are close to zero. These bottom edges of the pad can be considered to be regions of negligible contact pressure. These features do not significantly influence the stress values of the disc, as the highest contact pressure occurs near the top outer boarder region of the pad. The  $\beta$  central angle can be split into two  $39.1^\circ$  angles on each side of the  $0^\circ$  coordinate. Figure 32 shows that the stresses were relatively close to zero as measured by the strain gauges on the circumference at the  $39.1^\circ$  points.

There are tensile stresses at the  $-30^\circ$  and  $30^\circ$  disc orientations. The Literature (Section 2.4) determined that any pad length greater than the critical length value results in an inefficient pressure distribution and a change from compression to tension along the pad/backplate interface towards the ends. In other words, high aspect ratio pads may separate at the interface and cannot distribute pressure beyond the critical length. This can be extended to the disc stresses in explaining the presence of the tensile stresses.

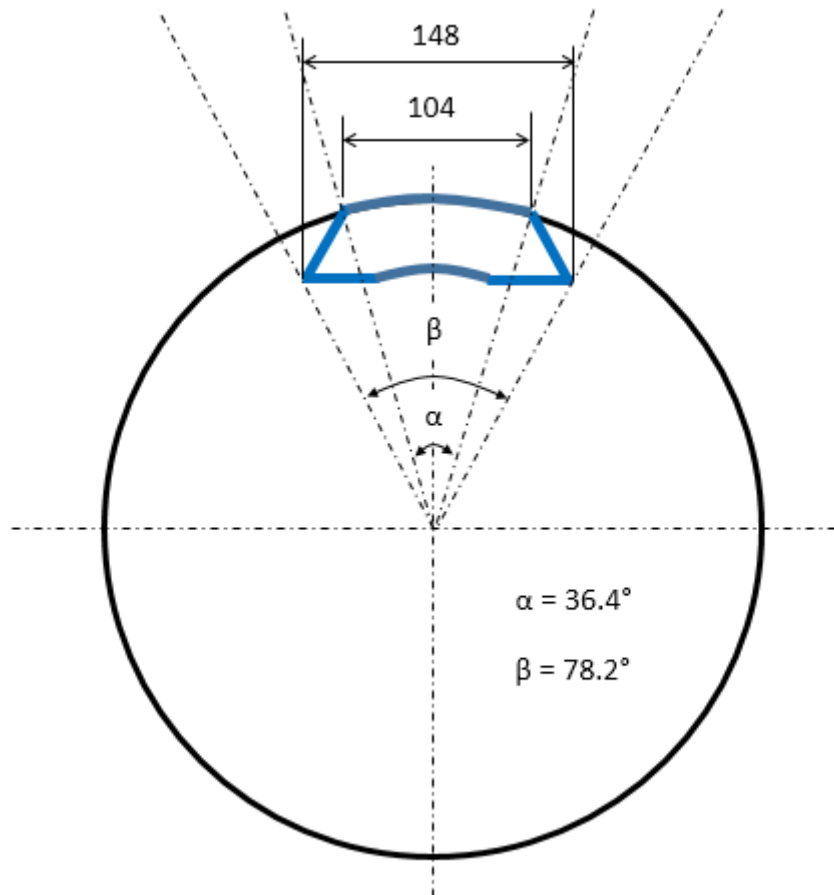


Figure 33: Brake pad pressing on the disc exhibiting the contact interface (not to scale)

The stresses decay rapidly moving away from the disc/pad contact interface where the far regions exhibit negligible stresses. This is visible as the regions between  $-60^\circ$  to  $-180^\circ$  and  $60^\circ$  to  $180^\circ$  exhibit zero stresses. The strains experienced by the solid brake disc due to the compressive clamping load applied by the brake pads are limited to the disc/pad contact interface only and do not distribute to the other regions of the disc.

### 5.3. Experimental Applied Brake Torque Load Test

For the applied brake torque load test the shaft torque (hence disc braking torque) was recorded simultaneously with the disc face strains as measured with the 6 uniaxial strain gauges that formed the two 45° strain gauge rosettes (upper and lower locations) installed on the disc outboard face in the region directly under the disc/pad contact interface as discussed in the Experimental Procedures (Section 3.4.2). Refer to Figure C-6 to Figure C-13 in Appendix C for the strain results as measured by the uniaxial strain gauges at the maximum applied torque of 1005 Nm. The torque was applied in a counter-clockwise direction as viewed on the disc outboard surface standpoint. Therefore, considering the convention of the disc orientation positions were set as clockwise positive, the leading edge are the positive angle orientations and the trailing edge are the negative angle orientations i.e. the region on the right of the 0° axis of the strain results are the leading edge, and the region on the left are the trailing edge. The disc/pad contact interface exists between the region of -18.2° to 18.2°, indicated as the region between the two dashed lines. It was evident that the disc outboard face strains as measured by the uniaxial strain gauges were not concentrated in the disc/pad contact interface region, but were distributed around the entire disc. However, the analysis of the distribution of the stress components provides a more comprehensive understanding.

The strains measured by the uniaxial strain gauges that formed the two strain gauge rosettes were then processed into stress results according to the procedure shown in Converting the Uniaxial Strains to Stresses (Section B.1 in Appendix B).

#### 5.3.1 Upper Location Strain Gauge Rosette

##### Normal Stress

The normal stress in the circumferential direction,  $\sigma_\theta$ , measured by the upper location strain gauges on the disc outboard face at different disc orientations is shown in Figure 34. The trend of the stresses is explained using Figure 36. The torque was applied in the counter-clockwise direction to the centre of the shaft and kept in equilibrium by the frictional forces to the right in Figure 34. These force elongate the disc material to the left i.e. for  $\theta < 0^\circ$  (-60° to -180°) and compress the disc material to the right i.e. for  $\theta > 0^\circ$  (30° to 180°).

The normal stress in the radial direction,  $\sigma_r$ , measured by the upper location strain gauge on the disc outboard face is shown in Figure 35. The regions which experience a tensile normal stress in the circumferential direction are accompanied by a compressive normal stress in the radial direction; and similarly regions which experience a compressive normal stress in the circumferential direction are accompanied by a tensile normal stress in the radial direction.

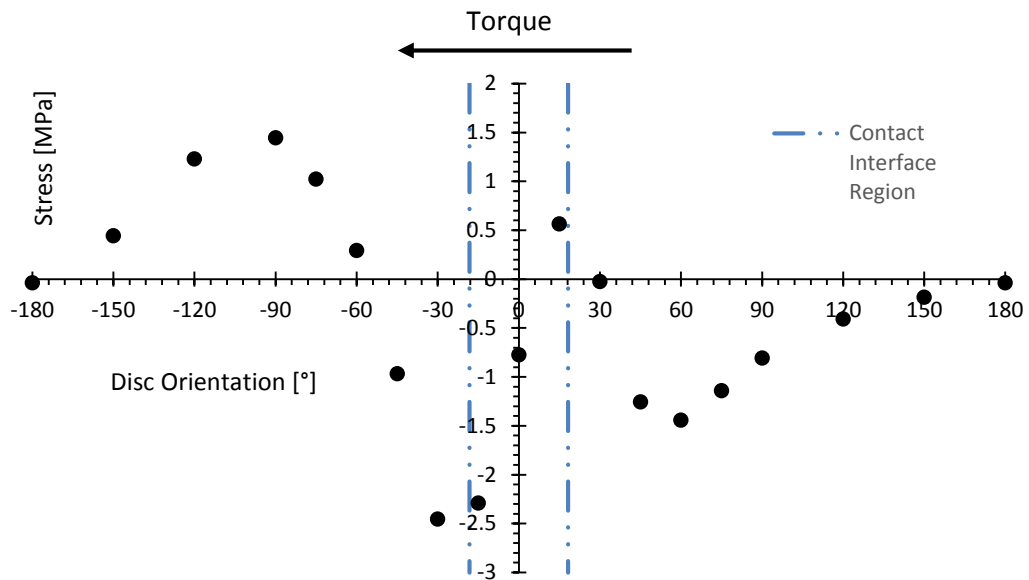


Figure 34: Normal stress  $\sigma_\theta$  experienced around solid disc face at the upper rosette location

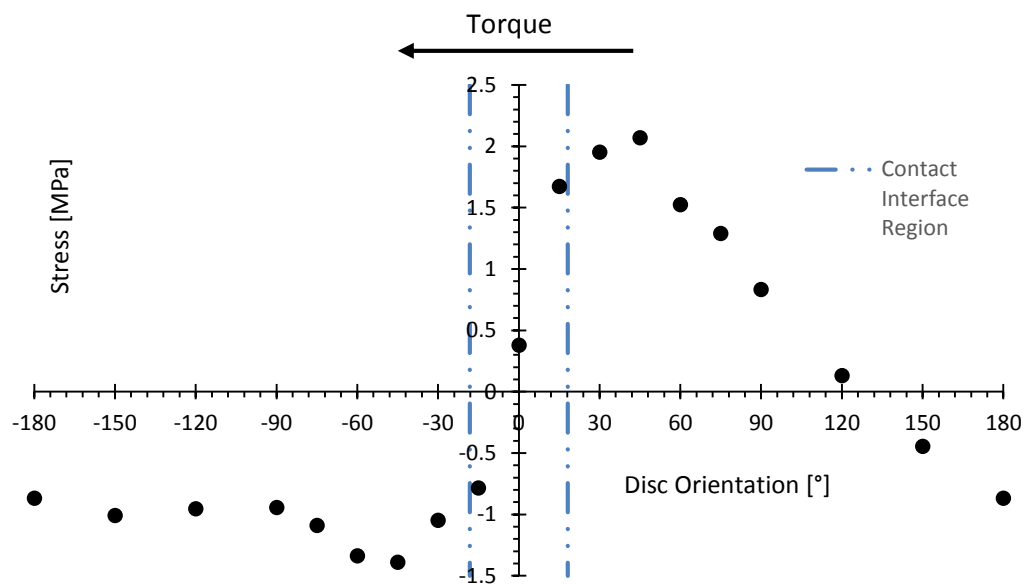


Figure 35: Normal stress  $\sigma_r$  experienced around solid disc face at the upper rosette location

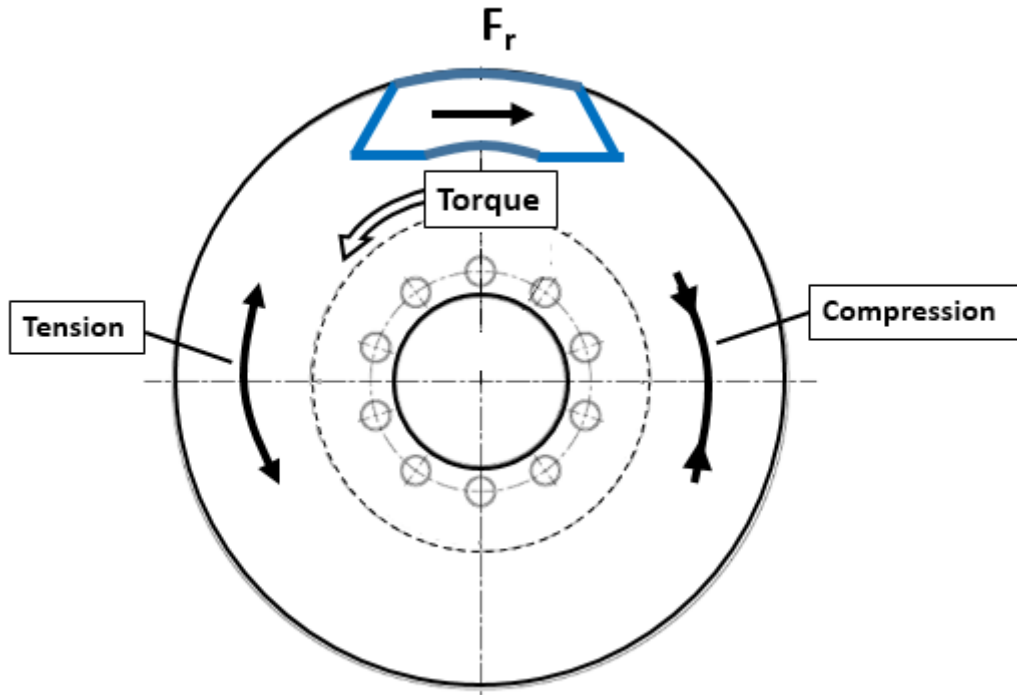


Figure 36: Visualisation of the effects of the normal stresses  $\sigma_\theta$  on the disc

### Shear Stress

The shear stress,  $\tau_{\theta r}$ , on the disc outboard face is shown in Figure 37. A common trait of disc brakes is that worn pads may exhibit significantly more wear on the leading entrance end (rotor entrance) as compared to the trailing end (rotor exit). The pressure is higher between the brake pad and disc at the leading end compared to the trailing which will cause non-uniform wear [8]. The interface pressure distribution is dependent on many factors (with differing factors between new and used pads). For the experimental testing, brand new pads were used and were supplied from the same box. According to Abu Bakar et al. [40] the pressure distribution for new brake pads are highly dependent on the pad surface topography which are ultimately dependent on the stringency of the manufacturing process. Therefore, new brake pads were utilised for the experimental clamping load tests which aimed to achieve near symmetrical uniform pressure loadings on the leading and trailing ends of the brake pads, which were proven true in the clamping load test results. Referring to the shear stress  $\tau_{\theta r}$  experienced around the disc face due to the applied torque load in Figure 37, it can be seen that the shear stresses are significantly higher on the leading end as compared to the trailing end in the contact interface region. The shear stress at  $15^\circ$  (leading end) was 1.05 MPa as compared to the shear stress at  $-15^\circ$  (trailing end) of 0.3 MPa. This behaviour was extended further to the adjacent regions as the shear stress at  $30^\circ$  was

2.4 MPa as compared to the shear stress at  $-30^\circ$  of 0.88 MPa. Previous results (Section 5.2) showed that the stress distribution under clamping load was symmetrical about the disc/pad interface geometric centre line. Pads exhibiting more wear on the leading edge side as compared to the trailing end can be attributed to the larger shear stresses experienced at the leading end as compared to the trailing end under the loading of applied brake torques.

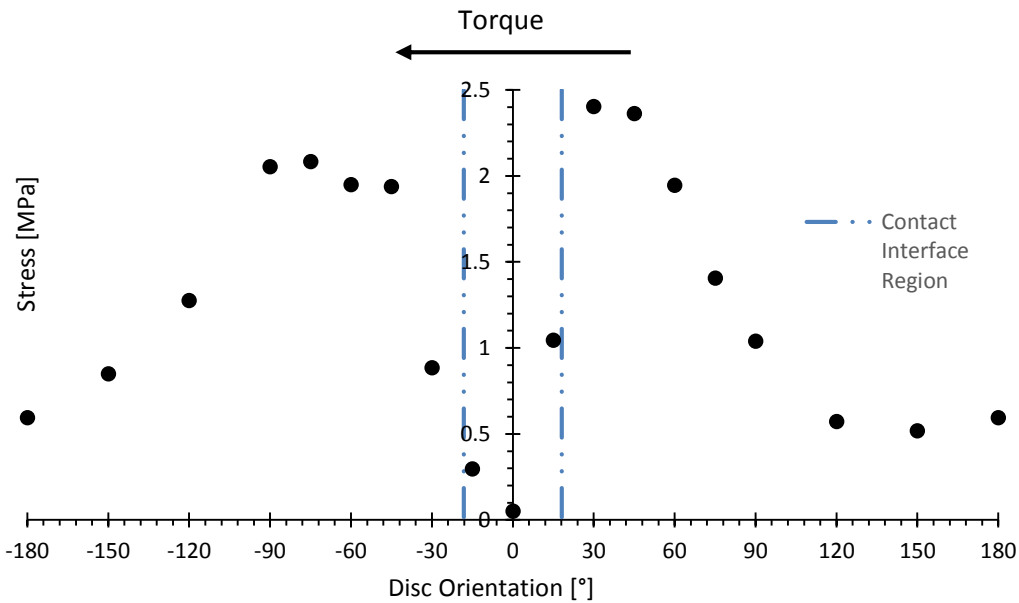


Figure 37: Shear stress  $\tau_{\theta r}$  experienced around solid disc face at the upper rosette location

The application of a torque to a circular cross-section member would result in equal shear stress at the same radial distance. The shear stress varies only along the radius from the centre (minimum) to the outer edge (maximum). The torsion formula, however, assumes that the member is long and that the torque is a pure couple. For the applied brake torque load test, the inboard and outboard pad were in contact with the disc and were responsible for the generation of the braking torque on the disc as it was through this contact that prevented the shaft from rotating the disc. Referring to Figure 37, the shear stresses  $\tau_{\theta r}$  were measured on the same radial distance from the disc core, around the entire disc, as the strain rosette was installed and fixed on the disc which was then rotated to different orientations to complete a revolution to monitor the strains at all disc orientations. For the torsion formula to hold, the shear stresses would be identical at all the disc orientations (i.e. the shear stress should be constant for all the orientations between  $-180^\circ$  to  $180^\circ$  on the results plot) since all the strains were measured at identical radial distances from the core of the disc. The disc/pad contact area (the point of application of the torque in equilibrium with



the counter-clockwise torque at the centre) is a relatively small region as compared to the entire disc area. Additionally, the thickness of a disc is relatively small compared to the length of a typical shaft or tube, therefore the localised deformations at the disc/pad contact cannot be neglected. In Figure 37 the shear stresses are not constant at all orientations but vary with orientation. The localised deformation effects are visible as the shear stresses change abruptly in the vicinity of the disc/pad contact interface and in the adjacent regions as seen by the steep and sudden changes of the gradients. The stresses then flatten moving away from the contact interface, to values of between 0.5 to 0.6 MPa in the far regions on the opposite end of the disc, further suggesting the presence of localised deformation at the contact interface. Interestingly the shear stress at the geometric centre of the contact interface (at  $0^\circ$ ) was near zero and the magnitudes of the stresses in the immediate region of the contact interface of  $-15^\circ$  and  $15^\circ$  were lower than the adjacent regions of non-contact at  $-30^\circ$  and  $30^\circ$ , respectively. The applied brake torque load test required the application of a 4 bar pneumatic chamber pressure clamping load which prevented the disc from rotating when the torque was applied. Although the strains due to the clamping load were compensated and removed from the results such that the processed stresses were due purely to the applied torque only, the clamping load of 50.4 kN restricted the deformations and strains directly under the contact interface. The force constrained the material at the disc/pad interface, and prevented it from deforming and developing shear stress. Thus shear stresses in the adjacent regions of the contact interface exhibit higher magnitudes than the shear stresses at the contact interface. It may be argued that during normal braking the clamping load has to be applied to generate the braking torque to decelerate a vehicle, but during normal braking the disc/pad interface would experience kinetic friction rather than static friction and thus allow more movement under the disc/pad interface.

The shear stresses were all positive in magnitude. The shear stresses are generated as a result of the torque; the area under the shear stress graph multiplied by the thickness of material through which the shear flow acts, multiplied by the radial distance measured from the disc centre to the rosette location. To calculate the area under the shear stress graph, Figure 37 was modified with the shear stresses plotted against the circumferential length instead of the orientation angles, as shown in Figure 38, where the shear stresses were plotted between  $-\pi r$  and  $\pi r$ . The circumferential length was calculated using the radius ( $r = 96 \text{ mm}$ ) measured from the disc centre to the rosette location. The area under the graph was calculated using the trapezoidal method to be  $719 (10^3) \text{ N/m}$ . The thickness of the

material through which the shear flow acts was 12 mm (see Figure 39 for the cross-section of half of the solid disc). Therefore, the torque calculated using the shear stress results was 829 Nm. The applied torque measured on the shaft was 1005 Nm. There was a 17.5% difference between the measured torque and the torque calculated using the shear stress. The difference is significant but has been deemed acceptable due to several reasons: the torque calculated using the shear stress graph is an approximation which uses the trapezoidal method and assumes the shear strain is constant through the thickness of the disc. Additionally, the thickness of the material through which the shear flow acts was assumed at the junction between the rubbing surface and disc hub (12 mm). However, this may be influenced with the complex changes of geometry and stress concentrations nearby. Therefore, the torque values are in reasonable agreement and provide reassurance that the experimental results are valid. Unlike the clamping stress results (Figure 31 and Figure 32) which were localised at the disc/pad interface, the brake torque stress results (Figure 37) acted through the entire orientation angle.

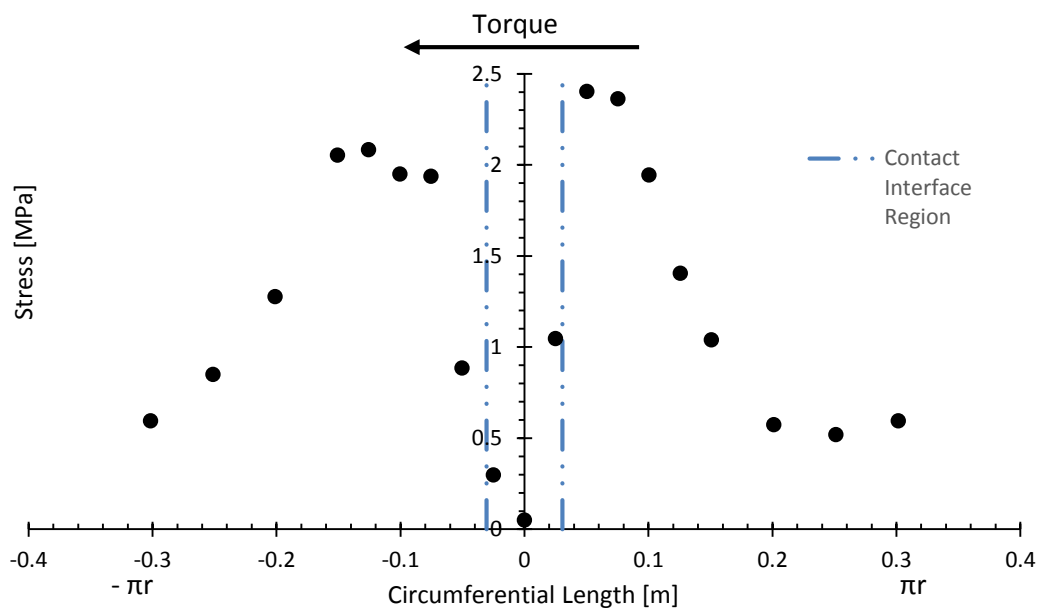


Figure 38: Shear stress  $\tau_{\theta r}$  experienced around circumferential length at the upper rosette radial position of the solid disc

The braking torque that brakes would generate on a vehicle operating on the road needs to be compared to the experimentally applied torques used. If the torque is similar in magnitude to the experimental values, then the results can be applied directly, otherwise appropriate scaling of the experimental results is required (before being applied to the design of the WBD core). The braking force was calculated by applying Newton's second law

of motion as shown in equation 2. A perfectly balanced brake distribution and equal axle loads were assumed, resulting in equal braking force on the four wheels of the vehicle. The total mass of the vehicle with payload was estimated at 10 tonnes (10 000 kg). The maximum achievable uniform braking deceleration is approximately 0.7g [42], which translates to a deceleration of 6.87 m/s<sup>2</sup>. Applying equation 2 results in a braking force  $F_B$  equal to 17.2 kN at each wheel. The braking torque can be estimated by multiplying the braking force by the radius of the tyre. The tyre specification for the Mercedes Benz Atego truck is 235/75R17.5, therefore the radius of the tyre is 398.5 mm. Therefore, the torque was calculated to be ~6841 Nm. Referring to Figure 36, the force of friction between the pad and disc is applied on both sides of the disc, since there is both the inboard pad and the outboard pad applying the braking. Therefore, only half the applied torque is transmitted through the WBD material. Therefore, the torque acting on each face is approximately 3421 Nm. The experimental applied torque was 1005 Nm. If the experimental results were to be applied to design the WBD reinforcement for vehicle braking on the road, the shear stress measurements would be required to be multiplied by a scaling factor of 3.42 to achieve the approximate results that the WBD material would experience under actual vehicle braking conditions.

$$4F_B = ma \quad (2)$$

The calculated normal strain  $\epsilon_z$  around the disc face is shown in Figure 40. The normal strains  $\epsilon_z$  were generated due to the Poisson's ratio and the application of the two normal stresses,  $\sigma_\theta$  and  $\sigma_r$ . Comparison of the normal strains  $\epsilon_z$  to the other two normal strain components  $\epsilon_\theta$  and  $\epsilon_r$ , show that the maximum magnitudes of the normal strains in the z-direction are less than half of those in the circumferential and radial directions. Comparison of  $\epsilon_z$  to the shear strains  $\gamma_{\theta r}$  also shows that the normal strains were significantly less than the shear strains. Therefore, it was important to obtain the values and distribution of the normal strains in the z-direction but the relatively small magnitudes showed that it was not the component that required the detailed analysis to design for failure due to an applied torque.

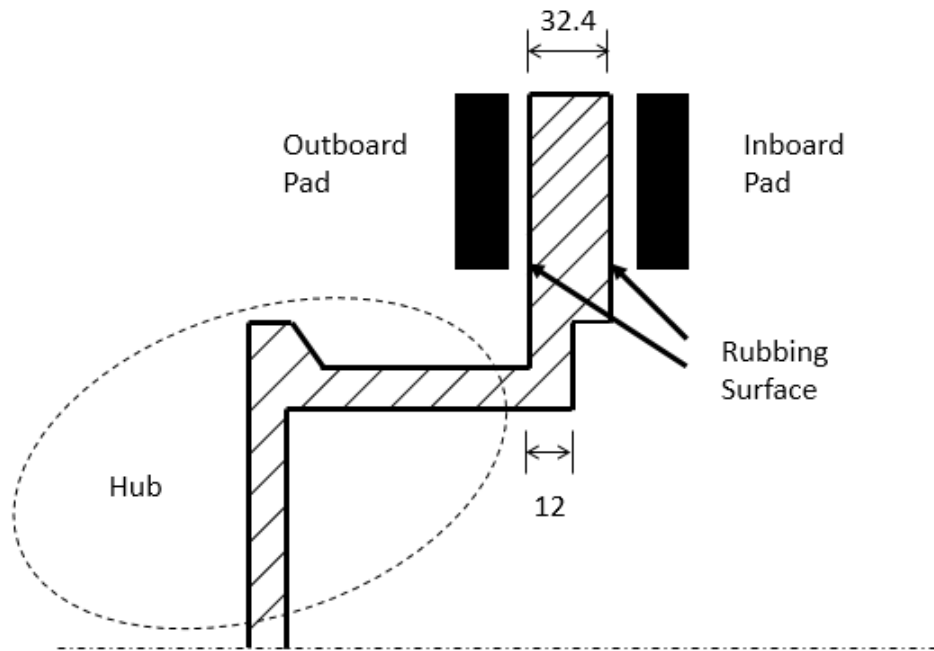


Figure 39: Cross-section of half solid disc with the disc and hub thickness (drawing not to scale and dimensions in mm)

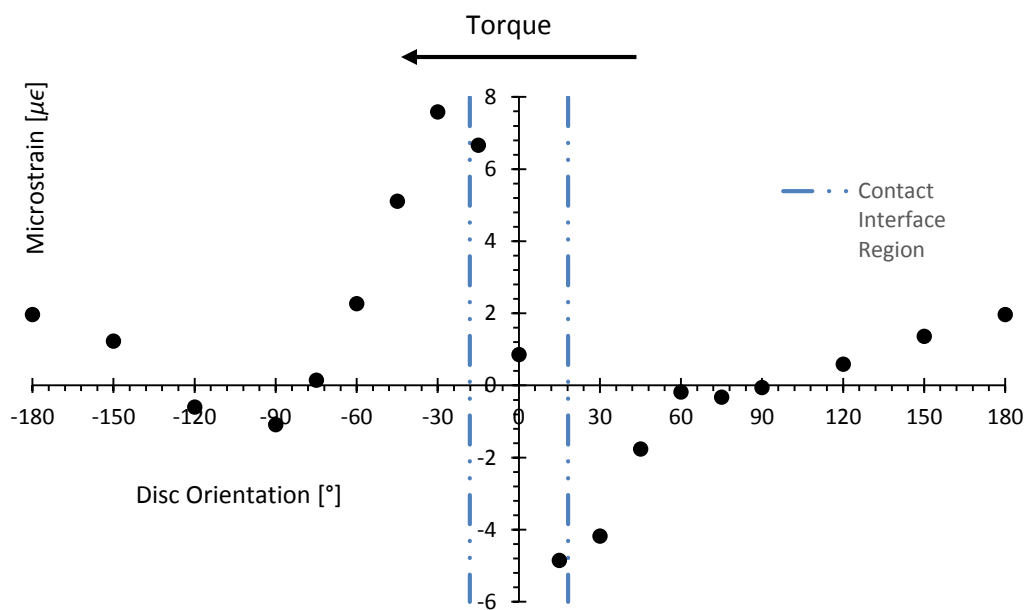


Figure 40: Calculated normal strain  $\epsilon_z$  around the solid disc face at the upper rosette location

### 5.3.2 Lower Position Strain Gauge Rosette

#### Normal Stress

The normal stress in the circumferential direction,  $\sigma_\theta$ , measured by the lower location strain gauges on the disc outboard face at different disc orientations is shown in Figure 41. The

trend of the stress results was identical to the results obtained for the normal stress in the circumferential direction obtained by the upper location rosette which displays repeatability of the behaviour. The normal stress in the radial direction,  $\sigma_r$ , on the disc outboard face is shown in Figure 42. The trend of the stress results was identical to the results obtained for the normal stress in the radial direction obtained by the upper location strain rosette which indicated repeatability.

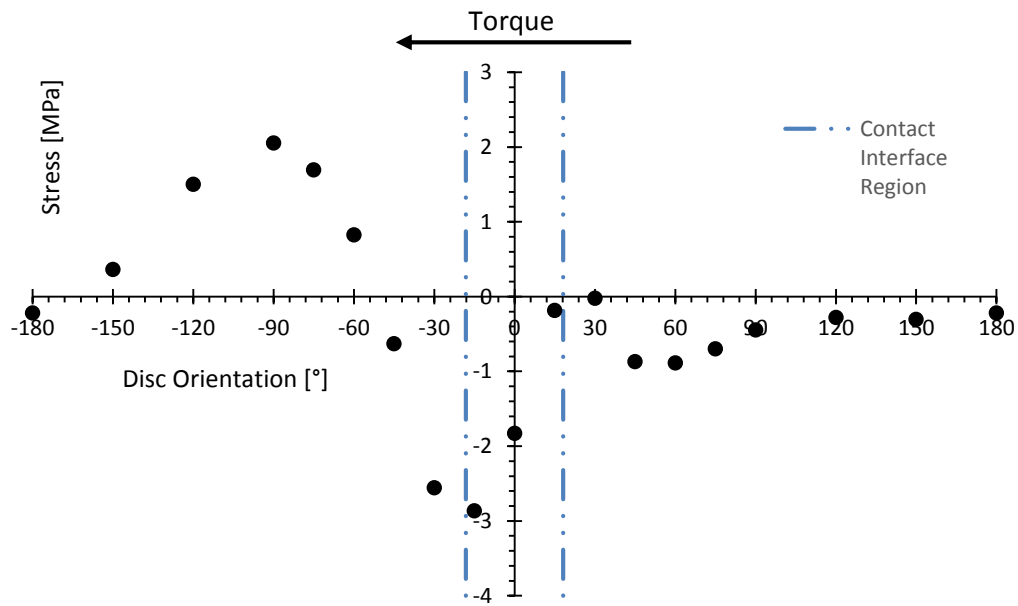


Figure 41: Normal stress  $\sigma_\theta$  experienced around solid disc face at the lower rosette location

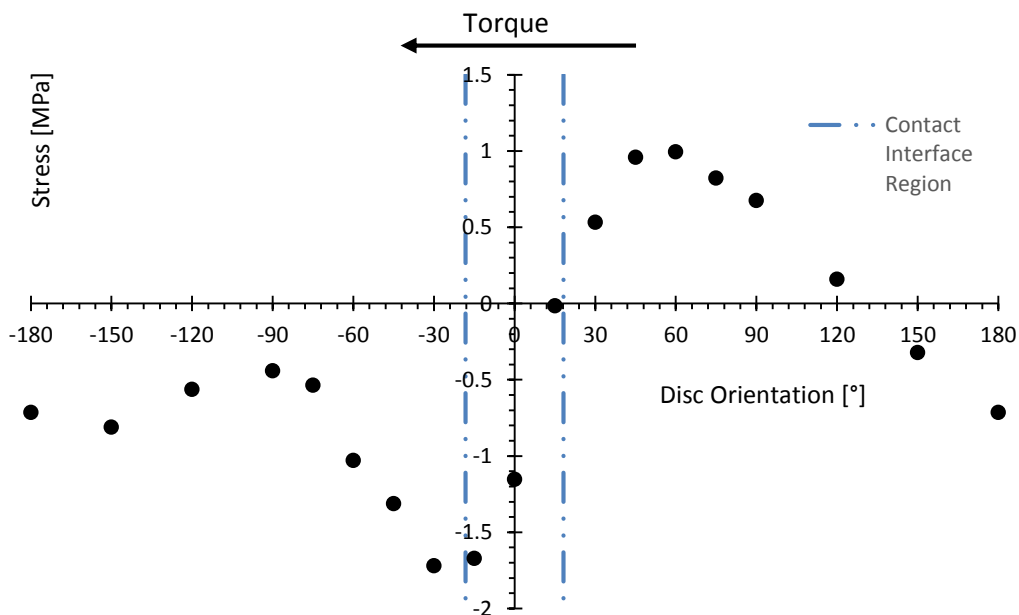


Figure 42: Normal stress  $\sigma_r$  experienced around solid disc face at the lower rosette location

## Shear Stress

The shear stress,  $\tau_{\theta r}$ , on the disc outboard face at the lower strain rosette position is shown in Figure 43. Similar to the upper location strain rosette, the shear stress  $\tau_{\theta r}$  experienced around the disc face due to the applied torque load can be seen to exhibit higher stresses on the leading end as compared to the trailing end of the contact interface. The shear stress at  $15^\circ$  (leading end) was 1.88 MPa as compared to the shear stress at  $-15^\circ$  (trailing end) of 1.53 MPa. This behaviour was further extended to the adjacent regions as the shear stress at  $30^\circ$  was 3.60 MPa as compared to the shear stress at  $-30^\circ$  of 3.06 MPa. Referring to the setup of the strain gauge rosettes, the upper location rosette was installed on the disc face directly below the contact area (as strain gauges would be damaged if placed directly within the contact area). It was discussed that the stress results and distributions were within expectations and conformed with the Literature (Section 2.4.4). The traits of the constriction of the shear deformation due to the clamping load was also visible for the lower rosette as the shear stresses between the regions of  $-30^\circ$  to  $30^\circ$  exhibited lower magnitudes as compared to the adjacent regions. This showed that the restriction of the shear deformation due to the clamping load was not limited to the contact region, but was extended to the regions towards the disc hub. Additionally, the shear stresses were greater near the contact interface region as compared to the far regions away on the opposite side of the disc. Therefore, it was observed that although the lower strain rosette was closer to the disc hub than the contacting interface, the effects of the local deformations at the points of application of the torque was extended along the radial lines from the contact interface to the hub. It was also shown that the shear stresses were distributed around the entire circumference, and not only concentrated at the contact interface.

When compared, the magnitudes of the shear stresses at the lower rosette were greater than those at the upper rosette at the corresponding orientations. The clamping force was applied by the pads during the braking action which subsequently developed the braking torque. The contact region was on the outer regions of the disc. Therefore, the torque developed was transferred from the outer region (from disc circumference) moving towards the centre of the disc. The magnitude of the torque transferred throughout would be identical. However, the area was decreasing (since the radius was decreasing), thus in order for the torque to remain the same, the shear stress needs to be greater in the region of decreased area. Additionally, since the lower location rosette was in close proximity to the disc recess, the presence of a stress concentration factor was possible. However, it was

noted that the ratios between the upper and lower rosette values differed at each orientation angle, therefore the common graphical method of selecting a stress concentration factor from handbooks to apply across all the orientations was not viable. The characterisation of the extent of the effect of the stress concentration was considered beyond the scope of the research as there were numerous factors to consider to achieve an accurate stress concentration model. Since the WBD disc consists of an identical hub setup to the solid disc, the lower rosette would be at a position of solid hub material with no contact to the WBD material. Therefore, the stress concentration effects of the recess are not required to be considered in the WBD brake disc stress analysis.

The calculated normal strain  $\epsilon_z$  around the disc face is shown in Figure 44. Similar to the upper strain rosette, the comparison of the normal strain  $\epsilon_z$  to the other two normal strain components  $\epsilon_\theta$  and  $\epsilon_r$ , show that the maximum magnitudes of the normal strains in the z-direction are less than half of those in the circumferential and radial directions. Comparison of  $\epsilon_z$  to the shear strains  $\gamma_{\theta r}$  also shows that the normal strains were significantly less than the shear strains.

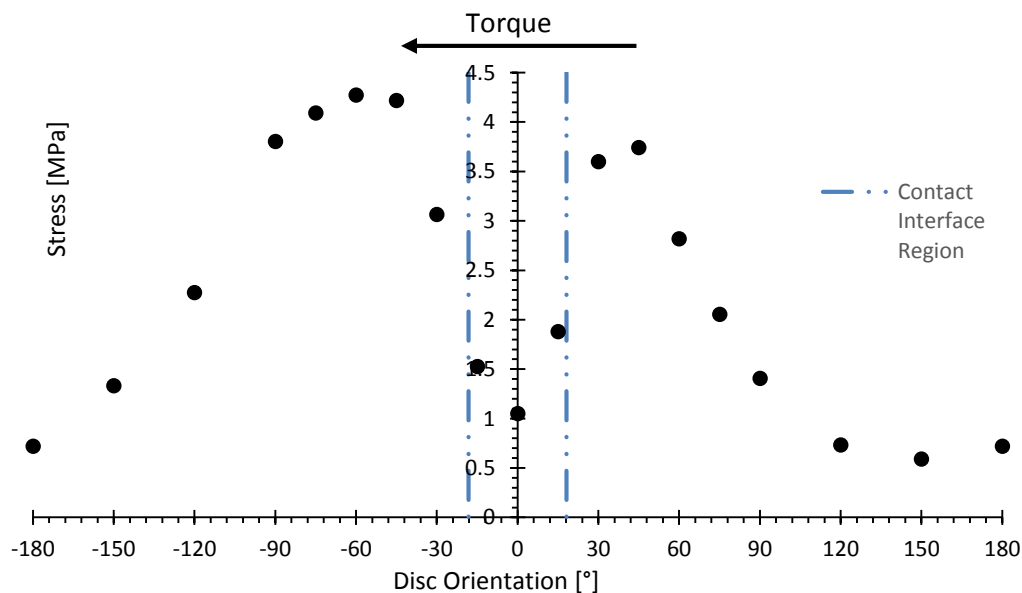


Figure 43: Shear stress  $\tau_{\theta r}$  experienced around solid disc face at the lower rosette location

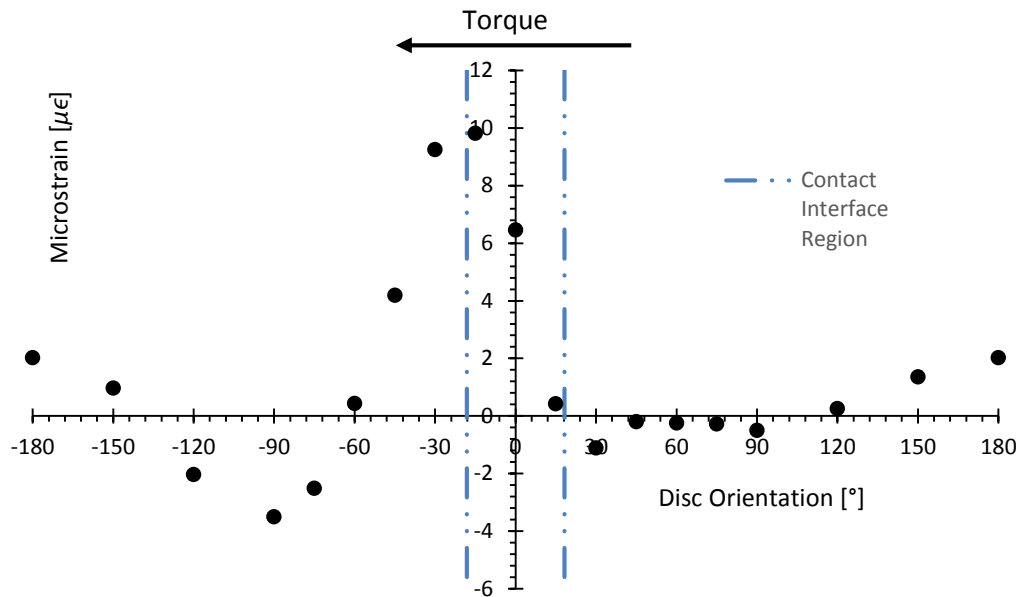


Figure 44: Calculated normal strain  $\epsilon_z$  around the solid disc face at the lower rosette location

#### 5.4. Design Application of the WBD Brake Disc Core

It was discussed in the Introduction (Section 1.1) that the current core of the WBD brake disc prototype required further development to increase the disc strength to withstand emergency braking. The first step was to understand how a brake caliper applies the load on a brake disc. It was found that there exists limited research in the literature on the loading mechanism of a brake disc as the need to determine the mechanical stresses due to a typical brake disc set-up has never been necessary; these stresses are well below the strength of typical brake disc materials like grey cast iron and steel. Therefore, it was required to first determine and characterise the loading mechanism of a solid brake disc with the resultant compressive stresses due to the clamping load as well as the shear stresses due to the applied braking torque. This was completed with the results discussed in Section 5.2 and Section 5.3, respectively. In this section the experimental solid brake disc stress distribution results will be applied to the WBD brake disc to determine the required reinforcement to the WBD core to ensure adequate strength of the core material for an improved lightweight brake disc suitable for use on a vehicle.

The cross-section for half of the WBD brake disc is shown in Figure 45. The WBD core is sandwiched between the two rubbing surfaces (made of solid material). The other dimensions of the WBD brake disc are identical to the solid brake disc as both discs are to be



fitted to the Mercedes Benz Atego truck. Therefore, the characterisation of the loading mechanism on the solid disc can be applied to the WBD disc. For the conditions of applying the brakes on a vehicle operating on the road, the maximum torque developed was calculated to be 6841 Nm (refer to Section 5.3.1 for the details of the calculation), which is divided by 2 to calculate the torque transmitted through each disc face; i.e. approximately 3421 Nm. Since the core of the solid brake disc was purely solid material, there was no differentiation between the core and the two rubbing surfaces. However, for the WBD brake disc the ventilated core consisted of porous material, that was sandwiched between the two solid rubbing surfaces. On the outboard side of the WBD disc (see Figure 45), the shear does not act through the WBD material; the load from the disc/pad interface is transmitted to the hub. However, on the inboard side the load is transmitted through the WBD material through to the hub.

Referring to the distribution of the shear stress results for the solid brake disc (Section 5.3), there was a degree of local deformation at the disc/pad contact interface regions but the shear stresses were distributed all throughout the circumference. This was applied to the WBD disc where the shear stresses were assumed to be distributed around the entire disc, such that the torque acted upon the entire face. Therefore, for the calculation of the shear stress, it was assumed that it acted over the entire WBD annulus area which presented a non-conservative approach. A torque on the inboard side of 3421 Nm, was assumed to be transferred through the WBD material. Referring to Figure 45, the outer radius ( $r_{\text{outer}}$ ) of the WBD disc is 167 mm, which coincides with the outer radius of the rubbing surface. The inner radius of the rubbing surface ( $r_{\text{inner}}$ ) is 93 mm. The annulus area between the outer and inner radius was the area that the shear stress acted upon. Since it was considered that the shear stresses were distributed around the entire circumference and not concentrated at the contact interface only, it was approximated that the torque was the result of an average force ( $F_{\text{average}}$ ) that acted on the WBD annulus area at the radial distance measured from the centre of the disc to the centre point of the annulus area (denoted as  $\bar{r}$ ) of 130 mm. The average force acted in the same direction as the force of friction between the pad and disc.  $F_{\text{average}}$  was calculated to be equal to 26.3 kN. Since the shear stresses were assumed to be distributed around the entire circumference, the average force value acted over the area of the WBD annulus, which was  $60.4 \times 10^{-3} \text{ m}^2$ . This resulted in an average shear stress value of 0.44 MPa around the entire circumference. However, localised deformation effects need to be accounted for to determine the maximum shear stress. Referring to the solid brake disc

shear stress results in Figure 37, the maximum shear stress was 2.40 MPa which was at the 30° position. The shear stress at the far regions of the disc away from the contact interface (180°) was 0.59 MPa. Therefore, the ratio between the maximum shear stress and the shear stress distributed at the far region was 4.05. This ratio was used as an approximation for a stress concentration factor to be applied to the shear stress results of the WBD disc to adjust for the localised deformation effects of the contact interface. Therefore, multiplying the ratio by the WBD average shear stress, resulted in a predicted WBD maximum shear stress of 1.76 MPa.

The maximum shear stress was required to be compared with the WBD material properties to ensure adequate strength. The equivalent compressive strength of the material is in the region of 6 MPa [22]. Referring to the WBD Shear Characteristics (Section 2.3.4), the shear strength as a first estimation can be determined from the analytic solution which simplifies to a strength ratio. The shear strength divided by the compressive strength of the WBD material is approximately between 0.5 to 0.7. Therefore, the expected equivalent shear strength of the WBD core was between 3 MPa to 4.2 MPa. For the further refinement of the estimation, the WBD material could be sheared in two different orientations (refer to Section 2.3.5 for details). The analytical solutions and numerical simulations were performed by Song et al. [32]. The shear strength was defined as the strength at a strain of 5%. The shear strength was determined to be between 2.4 MPa to 2.7 MPa. However, the results were for a slenderness ratio 7.5% less than the value for the WBD core for the disc. Therefore, referring to the trend in [32], it was expected that the shear strength to be greater for the larger slenderness ratio. It was to be noted that Song et al. [32] tested SUS 304 stainless steel wire core as the WBD material, while the WBD brake disc core was fabricated using cold-rolled mild steel SAE1006B wires. The yield strength of cold-rolled mild steel wires is greater than stainless steel wires. Nonetheless, the maximum shear stress for the WBD disc (1.76 MPa) was expected to be less than the shear strength of the WBD material. Therefore, it was not required to reinforce the shear component of the WBD disc. The discussion and analysis that follows focuses on the compressive loading of the clamping forces.

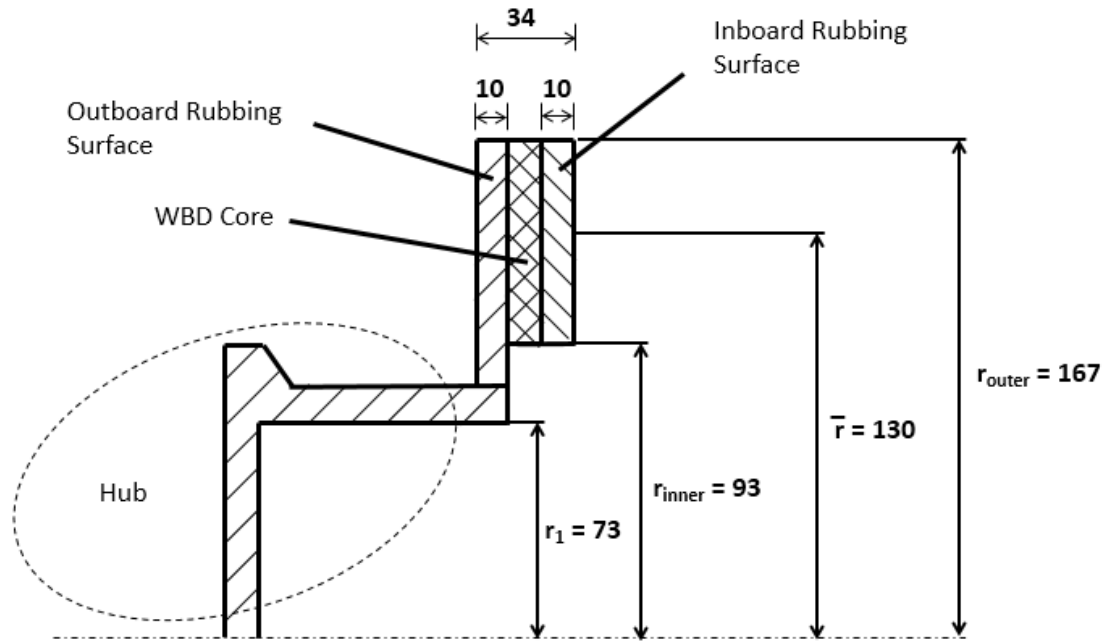


Figure 45: Cross-section of half of the WBD brake disc (not to scale and dimensions in mm)

Referring to the results from the clamping load test in Figure 32, the maximum compressive stress experienced by the solid brake disc was 16.8 MPa when loaded with a clamping load of 6 bar of pneumatic chamber pressure. According to the load cell test results, 6 bar of pneumatic chamber pressure was equivalent to the pad compressive force of approximately 77.4 kN. The brake pad area was calculated to be  $8.5 \times 10^{-3} \text{ m}^2$ . The average compressive stress was calculated as the applied compressive pad force divided over the brake pad area, resulting in a value of 9.11 MPa. It was to be expected that the maximum compressive stress would be greater than the average compressive stress as there were regions on the disc that exhibited tensile stresses, and as such will increase the magnitude of the compressive stress to compensate for equilibrium to obtain the average compressive stress. The ratio of the maximum compressive stress to the average compressive stress was 1.85. The ratio was applied to the WBD disc core reinforcement design as a stress concentration factor. It was not an exact solution but considering the stress distribution of the solid brake disc, it did provide insight into the WBD behaviour such that an estimation could be made. The trends of the solid brake disc results show that the shear stress is distributed around the entire circumference for the applied brake torque test. However, for the compressive stresses due to the clamping load the stresses were concentrated at the disc/pad contact interface and did not distribute to the entire disc, as the far regions away from the contact interface experienced zero stresses. The behaviour was applied to the design of the WBD brake disc reinforcement.

Since the compressive stresses were considered to be concentrated at the disc/pad contact interface only, the contact interface was the region considered for the reinforcement which is the pad area. According to the European Council Directive (EEC 71/320) [16] the pressure in the feed pipe to the brakes must be 6.5 bar. The United States of America Federal Motor Vehicle Safety Standards (FMVSS 121) [43] require the brake systems to be able to increase the air supply to 100 psi (6.9 bar). Therefore, the reinforcement of the core was designed for the core to withstand a maximum pneumatic chamber pressure of 7.0 bar, equivalent to the compressive pad force of approximately 90.7 kN, which was extrapolated from the results graph for the Load Cell Test (Section 4.1). For a relatively conservative approach a safety factor of 1.3 was applied to the force, thus the new force considered in the design application was 118 kN. The WBD brake disc was strengthened by reinforcing the WBD core with solid material to provide the necessary strength. The reinforcement design had to provide a method that was both cost-effective and practical to implement. The addition of ribs (or vanes) to the core was practical as vaned brake discs are well established. The amalgamation of the WBD material and the supporting ribs into the brake disc core will create a hybrid core that possesses improved thermal dissipation characteristics with the required strength properties. Straight radial ribs were utilised to reinforce the core as it was non-directional and realistic to implement. It was required that at any given moment in time of the rotation that there was a minimum of one rib providing support in the core under the contact interface. The reinforcement of the core with the straight ribs would unavoidably increase the overall mass of the disc. However, there was merit in reinforcing the WBD brake disc as it possessed superior heat dissipation properties as compared to the commercial brake discs. Consequently, one of the criteria for the design was to utilise the minimum quantity of ribs in the reinforcement to achieve the required strength, to avoid significantly increasing the overall mass of the disc.

The WBD ventilated core thickness (sandwiched between the two rubbing surfaces) is 14 mm. Since the ribs would be reinforcing the core by slotting it between the WBD material, it was required to fit between the core thickness (14 mm) to distribute the load originally supported solely by the WBD material. Figure 46 shows the WBD disc core reinforced with the solid rib material sandwiched between the WBD material in the core. It was shown that the compressive pad force was transferred through the rubbing surface to the core. Referring to Figure 46 and Figure 47, the compressive pad force of 118 kN is supported by both the WBD and rib material, generating the  $F_{WBD}$  and  $F_{rib}$  internal forces

respectively. Since the stresses were assumed to be concentrated in the disc/pad contact interface only, only the pad area was considered for the reinforcement.

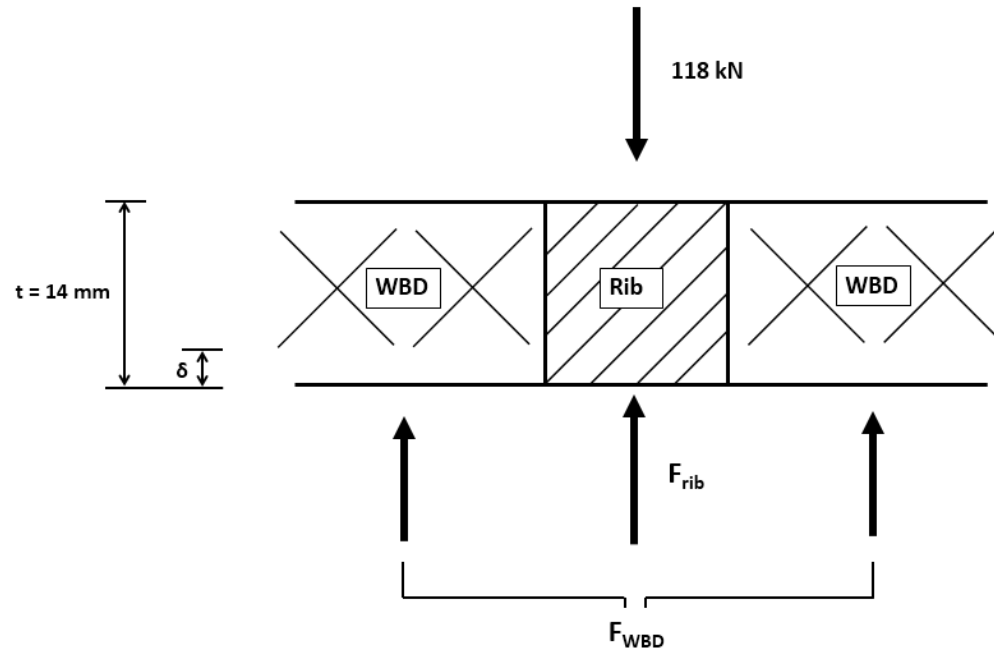


Figure 46: WBD core thickness reinforced with rib distributing the axial compressive pad load

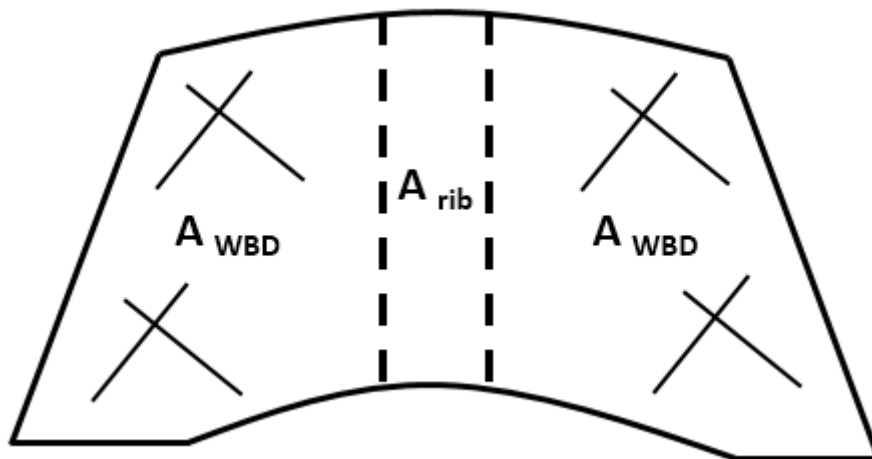


Figure 47: Pad area distribution considered to withstand the compressive force

Utilising the free body diagram of the core, the vertical force equilibrium is given by equation 3:

$$\begin{aligned} +\uparrow \Sigma F_y &= 0; \\ -118 \text{ kN} + F_{rib} + F_{WBD} &= 0 \end{aligned} \quad (3)$$

The problem is statically indeterminate; requiring compatibility conditions to be considered. The application of the compressive load onto the rubbing surface causes both the solid rib and the WBD material to displace the same amount in the core. This results in the displacements ( $\delta$ ):

$$\delta_{rib} = \delta_{WBD} \quad (4)$$

Applying the load-displacement relationships, results in equation 5. The equivalent Young's modulus of the WBD porous material is 1.08 GPa. The solid ribs would be manufactured using the same mild steel material (SAE1006) as the two solid rubbing surfaces that sandwiches the core which has a Young's modulus of 200 GPa.

$$\frac{F_{rib} t}{A_{rib} E_{rib}} = \frac{F_{WBD} t}{A_{WBD} E_{WBD}} \quad (5)$$

Where:

F: Internal force [N]

t: original thickness of core [m]

A: Cross-sectional area [m<sup>2</sup>]

E: Modulus of elasticity (or Young's modulus) [Pa]

The equivalent compressive strength of the WBD material is 6 MPa. It was previously mentioned that a stress concentration factor of 1.85 would be applied to compensate for the ratio between the maximum compressive stress and the average compressive stress. Therefore, the stress concentration factor ( $n$ ) was applied to the WBD average normal stress ( $\sigma_{WBD}$ ), as shown in equation 6.

$$\sigma_{WBD} = \frac{F_{WBD}}{A_{WBD}} n \quad (6)$$

The area of the pad ( $A_{pad}$ ) was previously calculated as  $8.5 (10^{-3}) \text{ m}^2$ . Referring to Figure 47, the pad area was segmented into two areas, namely the area wherein the WBD material supports the load ( $A_{WBD}$ ) and the area wherein the rib supports the remaining of the load ( $A_{rib}$ ). The relationship between the two areas is expressed in equation 7.

$$A_{WBD} + A_{rib} = A_{pad} \quad (7)$$

Solving equation 3 and equation 5 simultaneously, and rearranging the terms in equation 6 and equation 7 results in the expression for  $A_{rib}$ , as shown in equation 8.

$$A_{rib} = \frac{\left(\frac{E_{WBD}}{E_{rib}}\right) \left[ \frac{118 \text{ kN}}{\left(\frac{\sigma_{WBD}}{n}\right)} - A_{pad} \right]}{\left(1 - \frac{E_{WBD}}{E_{rib}}\right)} \quad (8)$$

Substituting the numerical values into equation 8 results in  $A_{rib}$  equal to  $1.51 (10^{-4}) \text{ m}^2$ . The other terms were subsequently calculated, with the results shown in Table 10. Therefore, the design of the rib was based on a rib area of  $1.51 (10^{-4}) \text{ m}^2$ . For the reinforcement analysis, it was assumed that the rib was at the centre position of the pad area as shown in Figure 47. At this position, the rib is approximated as a rectangular geometry. The vertical length at the centre of the pad was 66 mm, which would also be the length of the rib. Since the rib area and length were known, the width of the rib was calculated to be 2.29 mm. Therefore, the minimum width required for the rib to withstand the maximum compressive pad force of 118 kN is 2.29 mm. To reduce costs, dimensions should be specified to those readily available from metal suppliers, hence the rib dimensions for the reinforcement were designed to be mild steel flat bars 14 mm x 2.5 mm which could be obtained from a local supplier [44]. The WBD core was brazed onto the two mild steel rubbing surfaces. Since the ribs would be fabricated using the same grade of mild steel as the latter, the identical brazing method should be utilised such that the ribs are brazed simultaneously with the WBD material onto the rubbing surfaces.

Table 10: WBD disc reinforcement results for 118 kN of maximum compressive pad force

Parameter	Value
$A_{rib}$	$1.51 (10^{-4}) \text{ m}^2$
$A_{WBD}$	$8.35 (10^{-3}) \text{ m}^2$
$F_{WBD}$	27.1 kN
$F_{rib}$	90.9 kN

At any given orientation during the disc rotation there should be a minimum of one rib providing support in the core under the contact interface (refer to Figure 48). Therefore, the core should be reinforced with a sufficient number of ribs to withstand the maximum exerted compressive force, while not significantly increasing the overall weight. Referring to Figure 33 of the pad in contact with the disc, it can be seen that the bottom edge-to-edge

encloses an angle of  $78.2^\circ$ . Therefore, the angle of the centre line of the pad to either bottom edges of the pad encloses an angle of  $39.1^\circ$  on the disc. Therefore, considering the scenario that a rib is located at the  $0^\circ$  position (centre of pad), if a second rib is approaching the leading edge (hence aligned on the bottom right edge of the pad  $39.1^\circ$  away from the centre of the pad) where it is on the boundary of the contact interface and therefore not supporting the load yet. With a slight disc rotation, the rib in the centre position rotates counter-clockwise; the second rib originally positioned on the edge of the contact interface begins to support a portion of the load. The incoming second rib will gradually support more of the load as it rotates. When the second rib reaches the centre position of the pad, the first rib will be exiting the contact interface on the trailing edge on the bottom left edge of the pad. The second rib becomes the sole rib within the interface. However, at this moment, a third rib will be entering the contact interface on the leading edge from the bottom right pad edge, and the rotation motion will repeat with the ribs exiting and entering the interface. Therefore, if the ribs were spaced at least  $39.1^\circ$  from each other on the disc core, there would be a minimum of one rib within the contact interface at any moment of time during the rotation. Considering all the factors, the core was reinforced with 10 ribs, where the ribs would be installed with  $36^\circ$  spacing between each other in the core. Referring to Figure 45, the core encompassed the region between the outer and inner radius dimensions of the annulus. Therefore, although the rib was designed to reinforce the pad area only, for practicality during manufacturing the rib would be required to extend from the outer radius to inner radius of the annulus resulting in the rib with a length of 74 mm. Therefore, the final dimension of the rib was 74 x 14 x 2.5 mm. The density of the mild steel ribs (SAE1006) is  $7.87 (10^3) \text{ kg/m}^3$ , therefore the total mass added to the original disc by the 10 ribs was 0.20 kg. The newly designed reinforced WBD brake disc (13.67 kg) remains lighter than the commercially available pin-finned disc (14.22 kg).

The inclusion of ribs (vanes) to strengthen the WBD disc core will inexorably affect the heat transfer performance. However, vaned brake discs are well established. The suction side of the vanes are affected by the formation of flow recirculation regions which reduces the flow of cooling air in the ventilated channel. However, it is expected to be compensated as the WBD material in the core inherently possesses a stronger suction capability, increasing the resultant coolant rate. The three-dimensional thin ligaments of the WBD material leads to more uniform heat transfer. Additionally, the material has demonstrated stronger flow mixing, and combined with the enlarged heat transfer area considerably enhances the heat



transfer performance [12]. Therefore, with all these factors considered, it is expected that the WBD brake disc is viable after reinforcement.

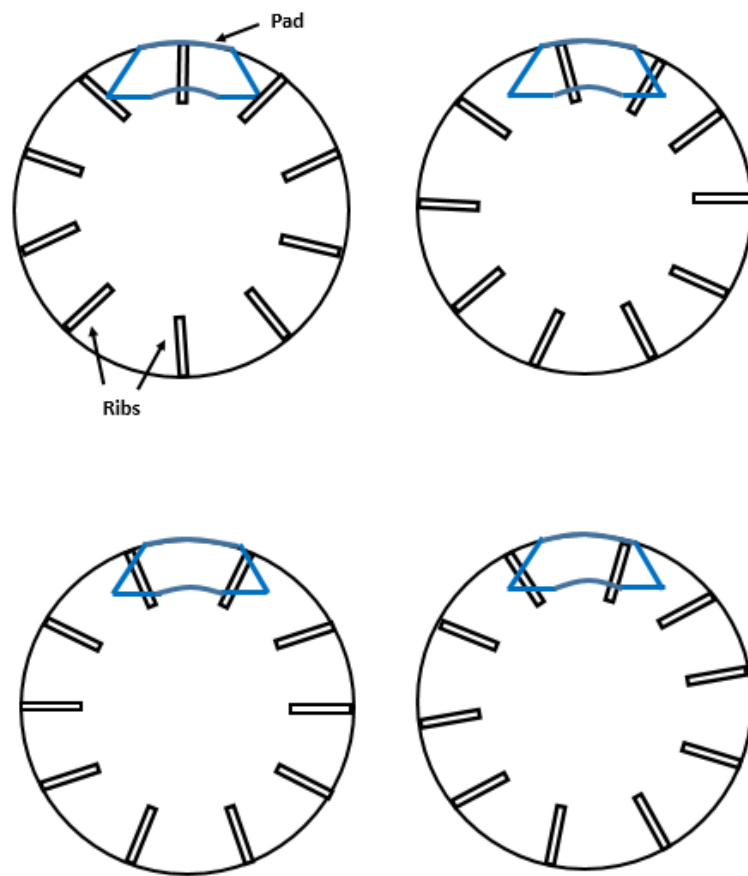


Figure 48: Minimum of one rib providing support in the disc core under the contact interface at any given orientation

## 6. CONCLUSIONS

The newly developed highly porous WBD brake disc required further research into improving the disc strength to reinforce the disc core to withstand the high stresses developed during emergency braking. The porous material possesses good strength especially when normalised by its mass but is nevertheless weaker than grey cast iron or mild steel. There exists limited research on the loading mechanism of a brake disc as the need to determine the mechanical stresses due to a typical brake disc set-up has never been necessary; these stresses are well below the strength of typical brake disc materials like grey cast iron and steel. Consequently, it was required to first characterise the loading mechanism of a solid brake disc with the resultant compressive stresses due to the clamping load as well as the shear stresses due to the applied braking torque. Thereafter, the experimental solid brake disc stress distribution results were applied to the WBD brake disc to determine the required reinforcement to the WBD core to ensure adequate strength of core material for an improved lightweight brake disc suitable for typical vehicle use.

The conclusions drawn from the research findings are summarised below:

1. The clamping load test performed on the solid brake disc was completed at four different pneumatic chamber pressures, namely: 1 bar, 2 bar, 4 bar, and 6 bar. The normal strains on the disc core were measured around the entire circumference of the disc.
  - a) A load cell test was performed to characterise the relationship between the pneumatic chamber pressures to the clamping forces applied by the brake pads. The trend was linear with the results as follow: 1 bar = 11.0 kN, 2 bar = 24.6 kN, 4 bar = 50.4 kN, 6 bar = 77.4 kN.
  - b) The disc core normal stresses were fairly symmetrical about the 0° vertical centre-line of the disc/pad contact interface, which represents a near uniform and equal distribution of the stresses on either sides of the centre-line. The symmetric interface pressure distribution about the geometric centre-line of the pad is an indication of a favourable pressure distribution as it would reduce uneven pad wear and brake squeal.
  - c) The highest compressive stresses experienced in the disc due to the clamping load were concentrated within the region of the disc/pad contact interface (between -18.2° to 18.2°). The stresses were concentrated at the disc/pad

contact interface only and did not distribute to the far regions of the disc, away from the contact interface.

- d) The maximum compressive stress experienced by the solid brake disc was 16.8 MPa when loaded with the pad compressive force of 77.4 kN. The average compressive stress calculated at this force was 9.11 MPa. Therefore, the ratio of the maximum compressive stress to the average compressive stress was 1.85.
2. For the applied brake torque load test the maximum torque applied was 1005 Nm. The disc face strains were measured with two strain gauge rosettes (upper and lower locations) installed on the disc outboard face in the region directly under the disc/pad contact interface.
  - a) A pad compressive force of 50.4 kN was applied to prevent the disc from rotating during the application of the torques. The clamping force under the pad constrained the material at the disc/pad contact interface and prevented it from shearing, as the shear stress at the centre of the contact interface ( $0^\circ$  orientation coordinate) were near zero.
  - b) Despite the presence of localised deformation effects at the disc/pad contact interface, it was shown that the shear stress was distributed throughout the circumference of the brake disc (as the stresses in the far regions away from the contact interface were non-zero) and not only concentrated at the contact interface.
  - c) The shear stresses are significantly higher on the leading end ( $0^\circ$  to  $30^\circ$ ) as compared to the trailing end ( $0$  to  $-30^\circ$ ) in and around the contact interface region. The inherent property of pads exhibiting more wear on the leading entrance as compared to the trailing end can be attributed to the larger shear stresses.
3. The experimental solid brake disc stress distribution results were applied to the WBD brake disc to design the required reinforcement to the WBD core.
  - a) The WBD core was analysed based on maximum deceleration conditions where the torque acting on each face of the disc was approximately 3421 Nm.
  - b) The average shear stress was calculated to be 0.44 MPa acting over the area of the WBD annulus; assumed to be distributed around the entire circumference. Applying a stress concentration factor due to the contact interface local deformation effects resulted in a predicted maximum shear stress of 1.76 MPa. This is lower than the expected equivalent shear strength of the WBD core

material (between 3 MPa to 4.2 MPa). Therefore, it is not required to reinforce the WBD to resist the shearing stress due to the torque.

- c) The reinforcement of the core was designed to withstand a maximum pneumatic chamber pressure of 7.0 bars. A safety factor of 1.3 was utilised, hence the clamping pad force considered for the reinforcement design application was 118 kN.
- d) The compressive stresses due to the clamping load was concentrated at the disc/pad contact interface only, therefore the contact interface was the region considered for the reinforcement. A stress concentration factor of 1.85 was implemented to compensate for the ratio between the maximum compressive stress to the average compressive stress (over pad area).
- e) Straight radial ribs are utilised to reinforce the core as it is non-directional, cost-effective and realistic to implement. The reinforcement was designed so that at any given moment in time of the rotation that there is a minimum of one rib providing support in the core under the contact interface region. The ribs were designed to be brazed sandwiched between the WBD material in the core.
- f) It was calculated that the minimum width required for the rib to withstand the maximum compressive pad force was 2.29 mm. Considering all the factors the final dimensions of the designed rib was 74 x 14 x 2.5 mm, manufactured from mild steel (SAE1006).
- g) The core is reinforced with 10 ribs in total, where the ribs is installed with 36° spacing in the core. The total mass added to the original disc by the 10 ribs is 0.20 kg. The newly designed reinforced WBD brake disc remains lighter than the commercially available pin-finned disc.

## 7. REFERENCES

- [1] Palencia JCG, Furubayashi T, Nakata T (2012) Energy use and CO<sub>2</sub> emissions reduction potential in passenger car fleet using zero emission vehicles and lightweight materials. *Energy*, 48(1): 548–565
- [2] Mohapatra S, Das S (2014) Introduction of high strength steel for commercial vehicles - light weighting of vehicles. SAE, 2014-28-0002
- [3] Olatunbosun OA, Gauchia A, Boada MJL, Diaz V (2011) Dynamic performance analysis of a light van body-in-white structure. *Proceedings of the Institution of Mechanical Engineers Part D Journal of Automobile Engineering*, 225(2): 167–177
- [4] Easton M, et al. (2008) Magnesium alloy applications in automotive structures. *JOM*, 60(11): 57–62
- [5] Joost WJ, Krajewski PE (2017) Towards magnesium alloys for high-volume automotive applications. *Scripta Materialia*, 128: 107–112
- [6] Havenga JH, Simpson ZP, King D, de Bod A, Braun M (2016) Logistics barometer South Africa. Stellenbosch University
- [7] Hrovat D (1988) Influence of unsprung weight on vehicle ride quality. *Journal of Sound and Vibration*, 124(3): 497–516
- [8] Limpert R (2011) Brake design and safety. 3rd edition. SAE International
- [9] Day AJ (2014) Braking of road vehicles. Butterworth-Heinemann
- [10] Mew T, Kim T, Kang K-J, Kienhöfer F (2014) Thermal comparison of solid and ventilated brake disc rotors, 9th South African Conference on Computational and Applied Mechanics, Somerset West, RSA (ISBN: 978-0-620-58994-9)
- [11] Mew T, Kang K-J, Kienhöfer F, Kim T (2015) Transient thermal response of a highly porous ventilated brake disc, *Proceedings of the Institution of Mechanical Engineers Part D Journal of Automobile Engineering*, 229(6): 674-683
- [12] Yan HB, Mew T, Lee M-G, Kang K-J, Lu TJ, Kienhöfer FW, Kim T (2015) Thermo-fluidic characteristics of a porous ventilated brake disc. *ASME Journal of Heat Transfer*, 137(2): 022601-11
- [13] Kienhöfer F, Zedi S, Kim T, Kang K-J (2016) Characterising the thermal performance of a novel lightweight brake disc with wire-woven ventilated channel at varying speeds, EuroBrake 2016, Milan, Italy (ISBN: 978-0-9572076-4-6)

- [14] Atkins M, Muhammad B, Suhail A, Kienhöfer F, Kang K-J, Kim T (2017) Field testing of a highly porous ventilated brake disc, EuroBrake 2017, Dresden, Germany (ISBN: 978-0-9572076-8-4)
- [15] Chen A (2016) Mechanical testing of a WBD disc, 4th year project, University of the Witwatersrand
- [16] The Council of the European Communities (1971), Council Directive 71/320/EEC, Official Journal of the European Union, Series I Volume 1971 (III) P.746 – 783
- [17] Palmer E, Mishra R, Fieldhouse J (2009) An optimization study of a multiple-row pin-vented brake disc to promote brake cooling using computational fluid dynamics. Proceedings of the Institution of Mechanical Engineers Part D Journal of Automobile Engineering, 223(7): 865–875
- [18] Palmer E, Mishra R, Fieldhouse JD (2008) A computational fluid dynamic analysis on the effect of front row pin geometry on the aerothermodynamic properties of a pin-vented brake disc. Proceedings of the Institution of Mechanical Engineers Part D Journal of Automobile Engineering, 222(7): 1231–1245
- [19] Campbell J (1991) Castings. Butterworth-Heinemann
- [20] Evans AG, Hutchinson JW, Ashby MF (1999) Multifunctionality of cellular metal systems. Progress in Materials Science, 43: 171-221
- [21] Lee BK, Kang K-J (2010) A parametric study on compressive characteristics of wire-woven bulk Kagome truss cores. Composite Structures, 92: 445-453
- [22] Lee M-G, Ko G-D, Song J, Kang K-J (2012) Compressive characteristics of a wire-woven cellular metal. Materials Science and Engineering A, 539: 185-193
- [23] Lee B-C, Lee K-W, Byun J-H, Kang K-J (2011) The compressive response of new composite truss cores. Composite Part B, 43(2): 317-324
- [24] Kim T, Kienhöfer F (2014) Novel lightweight highly-porous ventilated brake discs for light/heavy duty vehicles, South African and international patents (WO 2014/068540)
- [25] Kaina S, et al. (2016) Wire structure core brake disc - concept study. EuroBrake 2016, Milan, Italy (ISBN: 978-0-9572076-4-6)
- [26] Kieselstein E, et al. (2010) Cellular metals based on 3D-wire structures. Proceedings of the Cellmat Conference, Dresden, Germany
- [27] Gilles T, Automotive Chassis, Brakes, Suspension, and Steering, Delmar Learning, 2005
- [28] Kang K-J (2014), Wire-woven cellular metals: The present and future. Progress in Materials Science, 69: 213-307

- [29] Lee K.W, Park J-S, Jeon I., Kang K-J (2013) Equivalent material properties of a wire-woven cellular core. *Mechanics of Materials* 57:1-14
- [30] Lee M-G, Kang K-J, Mechanical properties of three variation of a wire-woven metal subjected to shear (2014), *International Journal of Solid and Structures* 51: 4504-4518
- [31] Lee M-G, Kang K-J (2014) Feasibility of a wire-woven metal for application as a sandwich core. *International Journal of Mechanical Sciences* 80: 81-92
- [32] Song JY, Ko JD, Lee KW, Kang K-J (2011), Shear Characteristics of WBK and WBD, In: *Proceedings of the 18<sup>th</sup> International Conference on Composite Materials*, Paper number: TH30-4-AK1224.
- [33] Tirovic M, Day AJ (1991), Disc Brake Interface Pressure Distributions, *Proc. Instn Mech. Engrs, Part D* (205) 137-146
- [34] Harding P.R.J., Wintle B.J. (1978), Flexural Effects in Disc Brake Pads, *Proc. Instn Mech. Engrs*, (192) 1-7
- [35] Day A.J., Newcomb T.P, Tirovic M (1991), Drum Brake Interface Pressure Distributions, *Proc. Instn Mech. Engrs, Part D* (205) 127-136
- [36] Dubensky R.G. (1985), Experimental Techniques for rotor performance measurements, SAE Paper 850078
- [37] Tumbrink H.J. (1989), Measurement of Load Distribution on Disc Brake Pads and Optimization of Disc Brakes Using the Ball Pressure Method, SAE Paper 890863
- [38] Abu Bakar A.R., Ouyang H., Cao Q. (2003), Interface Pressure Distributions Through Structural Modifications, SAE International, 21<sup>st</sup> Annual Brake Colloquium and Exhibition, Florida, USA, SAE Technical Paper 2003-01-3332
- [39] Chen F., Abdelhamid M.K, Blaschke P., Swayze J. (2003), On Automotive disc brake squeal Part III: Test and evaluation, SAE International, SAE Technical Paper 2003-01-1622
- [40] Abu Bakar A.R., Ouyang H., Siegel J. (2005), Brake Pad Surface Topography Part I: Contact Pressure Distribution, SAE International, SAE Technical Paper 2005-01-3941
- [41] Hibbeler R.C., *Mechanics of Materials* (2014), Pearson, Ninth Edition
- [42] WABCO, Product Catalogue: Inform “Search WABCO braking deceleration”, [Online]. Available: <http://inform.wabco-auto.com/intl/pdf/815/00/57/8150100573-23.pdf>
- [43] National Highway Traffic Safety Administration (Department of Transportation) (2009), Federal Motor Vehicle Safety Standards Number 121; Air Brake Systems, Chapter V Part 571 Subpart B
- [44] Njrsteel, Manufacturing “Steel flat bar – sizes and spec”, 2014. [Online]. Available: <http://www.njrsteel.com/manufacturing/flat-bar>

- [45] National Instruments Documentation (2018) Differences Between Accuracy, Code Width and Bits of Resolution, Available: <http://www.ni.com/product-documentation/54402/en/>
- [46] NI SCXI-1520, 2008. SCXI Universal Strain Gage Input, National Instruments, USA
- [47] NI SCXI-1600, 2004. SCXI Data Acquisition Systems – 16-Bit, 200 kS/s USB Data Acquisition Module, National Instruments, USA
- [48] Hoffmann K (1989) An Introduction to Measurements using Strain Gages. Hottinger Baldwin Messtechnik GmbH, Darmstadt Germany
- [49] SCXI, SCXI-1520, 2009 May. User Manual, National Instruments, USA
- [50] Window AL, Holister GS (1982) Strain Gauge Technology. Applied Sciences Publishers LTD
- [51] Eder L, Strain Gauge Circuitry: Wheatstone Bridge, Instruments for Engineering Measurement (IEM), South Africa



## APPENDIX A

### A.1. Strain Measurement Uncertainty

#### A.1.1. Code Width and Bits of Resolution

The code width of a data acquisition (DAQ) card that has an Analogue-to-Digital Converter (ADC) with specified bits of resolution can be calculated using equation A1.

$$Code\ Width = \frac{Range}{2^{bits}} \quad (A1)$$

The equation calculates the smallest change the ADC should be able to measure. It may be expected that the analog input measurements will fall within the calculated code width tolerance. However, during the recording of the actual measurements with the DAQ, the readings falls outside of the code width. The code width is a misleading source in determining the instrument's resolution [45]. A more accurate source of determining the instrument's resolution is to utilise the input noise specification. It is important to consider that before the measurement signal can be received by the ADC, the suitable input channel must be selected, together with applying the appropriate amount of gain. Signal conditioning may be required. Each of these components will be affected by real world phenomena which will introduce gain error, offset error, system noise, and temperature drift. All of these variables will affect the absolute accuracy of the module and the entire system. The quantification of these errors are performed in the sections that follow.

#### A.1.2. Absolute Accuracy

The code width and resolution do not solely define the accuracy of a system or module. Firstly, the accuracy of each of the system components need to be calculated before the overall system accuracy can be determined. It is required to identify how each component is connected to the system and the operating environmental parameters. National Instruments™ provides equation A2 for calculating the absolute accuracy for an individual device with gain, for a specified nominal range. The absolute accuracy is used to specify the overall maximum tolerance of the measurements.

*Absolute Accuracy*

$$= \pm[(Voltage\ Reading \times \% \ of\ Reading) + Offset\ Error \\ + System\ Noise + Temperature\ Drift]$$

Absolute accuracy is comprised of four components:

- Voltage reading: absolute magnitude of the voltage input. The full-scale voltage is frequently used for this value.
- % of Reading: a gain uncertainty factor which is multiplied by the actual input voltage for the measurement, which accounts for the gain error.
- Offset Error: the maximum offset error, a constant value applied to all the measurements.
- System Noise: error introduced to a measurement by the device itself. It is based on random noise and is dependent on whether a single sample is used or multiple samples being averaged. It includes the quantisation error.
- Temperature Drift: dependent on variations in the ambient temperature. However, temperature drift is already accounted for unless the ambient temperature is outside the range of 15°C to 35°C.

Absolute accuracy at full scale is commonly used to represent the absolute accuracy of a DAQ device. This is calculated using the maximum voltage within range taken one year after calibration. Each of the error terms can be obtained from the accuracy tables from the individual component's datasheet. The absolute accuracy for the SCXI-1520 module and the SCXI-1600 USB DAQ module is calculated using equation A2 where each of the error terms are read off the respective data sheets [46, 47]. The selected values are shown in Table A-1. For the duration of the experiment, the ambient temperature was maintained between 15 °C to 35°C, whereby the temperature effects had already been accounted for and as such the temperature drift value is equal to zero (0).

Table A-1: SCXI-1520 and SCXI-1600 absolute accuracy error terms

	SCXI-1520	SCXI-1600
Voltage Reading	2.5 V	2.5 V
Percent of Reading	±0.1	±18.8 (10 <sup>-3</sup> )
Offset	±1.5 mV	±811 µV
System Noise (Peak,100 point average)	0.5 µV	±46 µV
Temperature Drift	0	0

Frequently, it is useful to calculate the absolute accuracy relative to the input (RTI) as seen in equation A3.

$$Absolute\ Accuracy\ RTI = \pm \frac{Absolute\ Accuracy}{Input\ Voltage} \quad (A3)$$

The calculation of the absolute accuracy for the SCXI-1520 and SCXI-1600 is as follows:

#### SCXI-1520

##### Absolute Accuracy(SCXI-1520)

$$\begin{aligned}
 &= \pm [(Voltage\ Reading \times \% \text{ of Reading}) + Offset\ Error + System\ Noise + Temp.\ Drift] \\
 &= \pm [(2.5 \times 0.0001) + 0.0015 + 0.0000005] V \\
 &= \pm 1.751 \times 10^{-3} V \\
 &= \pm 1.751 mV
 \end{aligned}$$

##### Absolute Accuracy RTI (SCXI-1520)

$$\begin{aligned}
 &= \pm (1.751 \times 10^{-3})/2.5 \\
 &= \pm 0.07\%
 \end{aligned}$$

#### SCXI-1600

##### Absolute Accuracy(SCXI-1600)

$$\begin{aligned}
 &= \pm [(Voltage\ Reading \times \% \text{ of Reading}) + Offset\ Error + System\ Noise + Temp.\ Drift] \\
 &= \pm [(2.5 \times 0.0000188) + 0.000811 + 0.000046] \\
 &= \pm 0.904 \times 10^{-3} V \\
 &= \pm 0.904 mV
 \end{aligned}$$

##### Absolute Accuracy RTI (SCXI-1600)

$$\begin{aligned}
 &= \pm (0.904 \times 10^{-3})/2.5 \\
 &= \pm 0.036\%
 \end{aligned}$$

The absolute system accuracy represents the end-to-end accuracy of the signal conditioning and data acquisition device. Since the absolute accuracy of the various components may be setup for different input ranges, the absolute system accuracy is therefore calculated using the absolute accuracy RTI values for each component, as seen in equation A4.

##### *Total System Accuracy RTI*

$$= \sqrt{(Module\ absolute\ accuracy\ RTI)^2 + (DAQ\ Device\ Absolute\ Accuracy\ RTI)^2} \quad (A4)$$

Absolute System Accuracy based on the module and USB DAQ:

##### Total System Accuracy RTI (SCXI-1520 and SCXI-1600)

$$\begin{aligned}
 &= \pm \sqrt{(0.0007)^2 + (0.00036)^2} \\
 &= \pm 0.79 \times 10^{-3}
 \end{aligned}$$

$$= \pm 0.079\%$$

### A.1.3. Wheatstone Bridge Circuit Equation

The supply voltage,  $V_s$  and bridge output voltage,  $V_o$  of a Wheatstone bridge circuit can be expressed as a relative output voltage  $V_o/V_s$  to define the unbalance of the bridge. All bridge connections can be calculated using equation A5. If the bridge resistors  $R_1$  to  $R_4$  change their value by  $\Delta R$ , the bridge circuit will be unbalanced resulting in an output voltage  $V_o$  to be present.

$$\frac{V_o}{V_s} = \frac{R_1 + \Delta R_1}{R_1 + \Delta R_1 + R_2 + \Delta R_2} - \frac{R_4 + \Delta R_4}{R_3 + \Delta R_3 + R_4 + \Delta R_4} \quad (A5)$$

In strain gauge techniques all the arms of the bridge should possess the same resistance. The variations due to the tolerance of the strain gauge resistance does not affect the measurement accuracy. Differences as large as 5% in the resistance of  $R_1$  and  $R_2$  results in errors of less than 0.1% [48].

In strain gauge techniques the changes in resistance in metal strain gauges are very small, typically in the order of  $10^{-3}$ . Therefore, as an approximation it is frequent to use equation A6 [48]. It provides results that are sufficiently accurate for practical requirements.

$$\frac{V_o}{V_s} = \frac{1}{4} \left( \frac{\Delta R_1}{R_1} - \frac{\Delta R_2}{R_2} + \frac{\Delta R_3}{R_3} - \frac{\Delta R_4}{R_4} \right) \quad (A6)$$

The approximation formula shows that the relative change of resistance of each arm of the Wheatstone bridge is the governing factor in balancing the bridge, not the absolute change of resistance. The equation assumes that  $R_1$  to  $R_4$  in the bridge changes. For experimental stress analysis using a quarter-bridge configuration, only a single one of the bridge arm contains an active strain gauge while the remainder is made up of bridge completion resistors. Therefore, only  $R_1$  exhibits a resistance change, which results in a simplified equation as described by equation A7.

$$\frac{V_o}{V_s} = \frac{1}{4} \cdot \frac{\Delta R_1}{R_1} \quad (A7)$$

The relative change in resistance can additionally be described by equation A8.

$$\frac{\Delta R}{R} = k \cdot \varepsilon \quad (A8)$$

Substituting in equation A8 and rearranging results in

$$\frac{V_o}{V_s} = \frac{1}{4} \cdot \frac{\Delta R_1}{R_1} = \frac{1}{4} \cdot k \cdot \varepsilon \quad (A9)$$

Rearranging the equation in terms of  $\varepsilon$ :

$$\varepsilon = \frac{4}{k} \cdot \frac{V_o}{V_s} \quad (A10)$$

Using the root sum squares (RSS) method for propagation of uncertainty. The uncertainty  $\Delta\varepsilon$  can be calculated using equation A11.

$$\Delta\varepsilon = \sqrt{\left(\frac{\delta\varepsilon}{\delta V_0}\Delta V_0\right)^2 + \left(\frac{\delta\varepsilon}{\delta V_s}\Delta V_s\right)^2 + \left(\frac{\delta\varepsilon}{\delta k}\Delta k\right)^2} \quad (A11)$$

With the following partial derivatives:

$$\begin{aligned}\frac{\delta\varepsilon}{\delta V_0} &= \frac{4}{k}\left(\frac{1}{V_s}\right) \\ \frac{\delta\varepsilon}{\delta V_s} &= \frac{4V_0}{k}\left(-\frac{1}{V_s^2}\right) \\ \frac{\delta\varepsilon}{\delta k} &= \frac{4V_0}{V_s}\left(-\frac{1}{k^2}\right)\end{aligned}$$

The first two terms of equation A11 will not be calculated directly but will rather be represented by the absolute accuracy calculated above (Section A.1.2) for the strain gauge input module and the DAQ. This approximation is used as the input module and DAQ performs the excitation and signal processing. The uncertainty  $\Delta\varepsilon$  will vary for each data point as it is dependent on  $V_0/V_s$ .

The sample calculation performed was based on using the highest strain measured during the static test of the solid brake disc, where:

$$\varepsilon = 180 \mu\varepsilon$$

$$\Delta k = \pm 0.021$$

$$V_0/V_s = 9.45 (10^{-5})$$

$$\Delta\varepsilon = \sqrt{(SCXI1520 \text{ Error})^2 + (SCXI1600 \text{ Error})^2 + \left[(4)(9.45 \times 10^{-5})\left(-\frac{0.021}{2.1^2}\right)\right]^2}$$

Expressing the uncertainty  $\Delta\varepsilon$  as a percentage:

$$\begin{aligned}\frac{\Delta\varepsilon}{\varepsilon} &= \sqrt{(7 \times 10^{-4})^2 + (3.6 \times 10^{-4})^2 + \frac{(-1.8 \times 10^{-6})^2}{(180 \times 10^{-6})^2}} \\ &= 0.01 \\ &= 1 \%\end{aligned}$$

#### A.1.4. Alternative Approach of Calculating Uncertainty

It is not uncommon that the standard approach of calculating the uncertainty propagation (the RSS method) using the instrument uncertainties being considered not sufficiently accurate. It was noted that during the experiment there were noticeable fluctuations in the strain readings. A second method of calculating the uncertainty of the experiment was used

to validate the RSS method. The second method included applying a 6 bar brake pressure on the disc, and then recording the strain values at the 0° disc orientation. This was repeated five times at this same location. Ideally these five measurements should be equal. However, there will be differences in real applications as the system is subjected to many internal and external factors that cannot be completely eliminated such as noise and disturbances. The uncertainty was calculated based on the standard deviation of the five strain readings and was performed for each strain gauge.

Table A-2 contains the standard deviation for the three strain gauges that were used for the static test of the solid brake disc. The standard deviation is divided by the measured strain values at 1, 2, 4, and 6 bar brake pressures and is expressed as a percentage. At the lowest brake pressure of 1 bar the strain uncertainty is 8.2%, 0.26%, and 2.53% for strain gauge 1 to strain gauge 3, respectively. At the highest brake pressure of 6 bar the uncertainty is 0.47%, 0.04%, and 0.29% for strain gauge 1 to strain gauge 3, respectively. The percentage of error for all the strain gauges decreased as the braking pressure increased. Therefore, the uncertainty at the lowest braking pressure does slightly affect the strain values but is within an acceptable range. At the higher braking pressures, the uncertainty can be considered negligible.

Table A-2: Standard deviation of the static test of the solid brake disc

	Strain Gauge 1	Strain Gauge 2	Strain Gauge 3
Standard deviation [ $\mu\text{m}/\mu\text{m}$ ]	0.554 ( $10^{-6}$ )	70.23 ( $10^{-9}$ )	0.388 ( $10^{-6}$ )
% error at 1 bar	8.20%	0.26%	2.53%
% error at 2 bar	2.50%	0.14%	1.08%
% error at 4 bar	0.80%	0.07%	0.46%
% error at 6 bar	0.47%	0.04%	0.29%

Averaging the uncertainty values across the three strain gauges and across all pressures results in an uncertainty of 1.41%. Comparison of the uncertainty calculated based on the RSS method and the standard deviation method thus shows good correlation. The shunt calibration capability is able to correct for system gain error and discrepancies between the nominal gauge factor and actual gauge factor of the strain gauge [49]. Therefore, the error would be less as the SCXI signal processing device is able to provide compensation.

#### A.1.5. Wheatstone Bridge Linearity

Wheatstone bridge non-linearity occurs under the general conditions of non-symmetrical resistance changes within the bridge and also when the resistance changes are large. Applying the quarter bridge configuration, for most measurements on metals within the elastic range where the changes in resistance are small, the non-linearity error is negligible [50]. For strains less than  $-250 \mu\text{m/m}$  the non-linearity error in quarter bridge configuration is less than 0.1% [51].

#### **A.1.6. Bridge Balance**

Generally, most strain signal processing systems is equipped with the function to perform the initial balancing of the bridge to compensate for resistance tolerances of the gauges and lead wires. This is performed to compensate for the initial strain offsets. Each input channel of the SCXI-1520 module included an offset null compensation circuit to remove the initial bridge offset voltage from the Wheatstone bridge. This adjusted the signal voltages to the desired levels when the strain gauge or bridge sensor was in the unstrained state. The Kyowa  $350 \Omega$  strain gauges used for the research experiments had an uncertainty of  $\pm 2.4 \Omega$ . This uncertainty was compensated in the bridge circuit through the bridge balancing performed prior to the testing, which was performed through driver software which nulls the offset voltage to zero, replacing the need to manually adjust a potentiometer. The removal of the offset allowed for an increased system gain which lead on to an increased measurement sensitivity and resolution.

#### **A.1.7. Shunt Calibration**

Each of the input channels of the SCXI-1520 module was equipped with two independent shunt calibration circuits which could be activated to simulate two separate loading effects to obtain a gain adjust factor to compensate for the possibility of system gain errors or any discrepancies in the nominal gauge factor. The shunt calibration resistors were located within the sockets of the SCXI-1314 front-mounting terminal block. These shunt resistors were enabled or disabled through software commands such that the user was not required to explicitly control the shunt calibration switches but instead allowed the driver software to make automatic adjustments during the automated shunt calibration procedure.

### **A.2. Load Cell Test**

Table A-3 contains the clamping forces corresponding to each of the pneumatic chamber pressures from the load cell test.

Table A-3: Clamping forces for each pneumatic chamber pressures as per the load cell test

Pneumatic Pressure [Bars]	Clamping Force [kN]
0.5	3.724
1	10.95
1.5	17.91
2	24.64
2.5	31.14
3	37.7
3.5	44.03
4	50.44
5	64.12 (Extrapolated)
6	77.42 (Extrapolated)

### A.3. Shaft Torque Calibration

The shaft torque (hence braking torque) was monitored by measuring the strain obtained by strain gauges directly installed on the shaft. Two pairs of biaxial strain gauges orientated at  $45^\circ$  was mounted on the shaft and wired in a full bridge configuration. Due to the twisting force, the surface of the shaft under torque experiences compression and tension which were both measured by the two strain gauges on each of the biaxial strain gauge rosettes. The strain gauges were connected to the Lord MicroStrain SG-Link-Oem-LXRS analog input sensor node for signal processing. The signals were wirelessly transmitted to the Lord MicroStrain WSDA-Base-101 analog output base station which interfaced with the computer via USB connection.

A shaft torque calibration procedure was performed to validate the accuracy of the shaft strains (used to calculate the torque) measured by the strain gauges. A flat bar of known dimensions was manufactured where one end has two drilled holes with similar diameters to the bolts that secure the brake disc to the flange. The flat bar was inserted in place by sharing two bolts with the brake disc and was secured with the two nuts tightening against the flat bar. The opposite end of the flat bar had a single hole drilled where the mass hanger was hooked through. Slotted calibration weights were placed on the mass hanger. The shaft end by the gearbox was restrained such that the shaft did not rotate when the calibration torque was applied on the flange end. The calibration set-up is shown in Figure 27 and it can be seen from the configuration that the torque acts through the centre of the shaft.



Therefore, with known calibration weights and the lever arm distance, the applied torque through the flat bar (hence the shaft) is calculated as the product of the two values.

The experimental shaft torque measured by the strain gauges were compared with the applied calibration weight torques mentioned above. The strain values measured were recorded using NodeCommander proprietary software. Shunt calibration and other initialising settings were performed in the software to prepare the strain gauges before each operation.

In total, four calibration weights were used to perform the torque calibration. The force applied by the combinations of these weights are shown in Table A-4. The flat bar lever arm distance was 0.5 m which was measured from the point at which the mass hanger was located, to the centre point of the shaft. Therefore, the corresponding calibration torques were the products of the calibration weight and lever arm distance, as seen in Table A-4.

Table A-4: Calibration weights and corresponding torques

Calibration Weights	Force [N]	Calibration Torque (= F x d)
50N	50	25 Nm
50N + 5kg	99.1	49.5 Nm
50N + 5kg + 50N	149	74.5 Nm
50N + 5kg + 50N + 5kg	198	99.1 Nm

Shear strain is twice the experimental strain measured by the strain gauge orientated at 45°. Therefore, the torsional shear stress is calculated using equation A12, where G is the shear modulus.

$$\tau_{(experimental)} = 2(\epsilon_{measured})G \quad (A12)$$

The torque is calculated using equation A13.

$$T = \frac{\tau J}{R} \quad (A13)$$

Where:

T: Torque

$\tau$ : Torsional shear stress

J: Polar moment of inertia

R: Radius of the shaft

The polar moment of inertia was calculated using equation A14, where  $d$  is the diameter of the shaft,  $d = 60$  mm. Therefore, the polar moment of inertia for the shaft,  $J = 1.272 (10^{-6})$  m<sup>4</sup>. The shaft was manufactured from EN8 carbon steel where the shear modulus is approximately  $G = 79$  GPa.

$$J = \frac{\pi d^4}{32} \quad (A14)$$

The experimental torque was calculated using equation A12 to equation A14 which is based on the strain recorded by the strain gauges on the shaft. These strain values were recorded in NodeCommander where the sampling rate was set at 128 Hz. To further minimise noise, the strain values were processed as an averaged value over 2000 readings. The experimentally measured strain, torsional shear stress, and torque are shown in Table A-5.

Table A-5: Measured torque results based on experimental shaft strain

Calibration Weights	Strain [ $\mu$ Strain]	$\tau$ (experimental) [MPa]	Measured Torque [Nm]
50N	3.332	0.527	22.33
50N + 5kg	6.755	1.067	45.26
50N + 5kg + 50N	10.34	1.633	69.26
50N + 5kg + 50N + 5kg	13.86	2.190	92.88

The measured torque values calculated from the strain gauge readings were compared to the calibration weight torques. The difference between the two values displayed a trend of decreasing differences from a 10.68% difference at the smallest calibration weight to a 6.23% difference at the highest calibration weight as seen in Table A-6. This exhibits good correlation between the known applied calibration torque and the experimentally measured torque, where it can be concluded that the accuracy of the torque measured using the strain gauges are acceptable. The calibration procedure was originally performed using the Lord MicroStrain devices and NodeCommander software to determine the shaft torque, however it was later decided that for the applied torque load test to wire the shaft strain rosettes into the SXCI DAQ as it provided synchronised timing with the other strain gauges measuring the shear on the brake disc. For reassurance purposes the lightest (50N) and heaviest (50N + 5kg + 50N + 5kg) calibration weights torque tests were repeated with the SCXI DAQ, which yielded very similar results to those in Table A-5.

Table A-6: Percentage differences between calibration torque and measured torque

Calibration Weights	Calibration Torque [Nm]	Measured Torque [Nm]	Percentage Difference [%]
50N	25	22.33	10.68
50N + 5kg	49.53	45.26	8.61
50N + 5kg + 50N	74.53	69.26	7.06
50N + 5kg + 50N + 5kg	99.05	92.88	6.23

## APPENDIX B

### B.1 Converting the Uniaxial Strains to Stresses (for Applied Torque Load Test)

A single uniaxial strain gauge measures the normal strain in the material. When determining the general loading on a body, the strains at a point on the free surface are determined using a cluster of three strain gauges arranged in a specified pattern, a strain gauge rosette. The normal strains measured by the three strain gauges are transformed to specify the state of strain at that point. These three strains are measured only in the plane of the gauges. Additionally, since gauges are mounted on the free surface of a body, it is known that the body is stress-free on the surface in the direction normal to the surface. The strain normal to the surface was measured, but it was assumed that the out-of-plane strain will not affect the in-plane measurements of the strain gauges [41].

The experiment was conducted with the configuration of 45° strain rosettes, where the arrangement of the axes of the three strain gauges are shown in Figure 23. Using the strains measured by the strain gauges  $\epsilon_a$ ,  $\epsilon_b$ ,  $\epsilon_c$ , it is possible to determine the strain components  $\epsilon_x$ ,  $\epsilon_y$ ,  $\gamma_{xy}$  at that point by applying the strain-transformation equations (equations B1 – B3).

$$\epsilon_a = \epsilon_x \cos^2 \theta_a + \epsilon_y \sin^2 \theta_a + \gamma_{xy} \sin \theta_a \cos \theta_a \quad (B1)$$

$$\epsilon_b = \epsilon_x \cos^2 \theta_b + \epsilon_y \sin^2 \theta_b + \gamma_{xy} \sin \theta_b \cos \theta_b \quad (B2)$$

$$\epsilon_c = \epsilon_x \cos^2 \theta_c + \epsilon_y \sin^2 \theta_c + \gamma_{xy} \sin \theta_c \cos \theta_c \quad (B3)$$

The angle  $\theta$  is measured counter-clockwise from the x-axis to each of the strain gauge axis. Therefore,  $\theta_a = 0^\circ$ ,  $\theta_b = 45^\circ$ ,  $\theta_c = 90^\circ$ . Applying these values to equations (B1 - B3) and solving simultaneously results in equations B4 - B6.

$$\epsilon_x = \epsilon_a \quad (B4)$$

$$\epsilon_y = \epsilon_c \quad (B5)$$

$$\gamma_{xy} = 2\epsilon_b - (\epsilon_a + \epsilon_c) \quad (B6)$$

It was mentioned in the Repeatability of the Uniaxial Strain Gauges Orientated at 45° (Section 4.4) that for the processing of the strain results to stress values that it was possible to process the rosette using either strain gauge 1 and 2 or strain gauge 3 and 4 as the 45° orientation gauges, as either pair would produce similar stress results. Therefore, strain gauge 1 and 2 were used as the 45° orientation strain gauges to form the rosettes, as shown in Figure B-1.

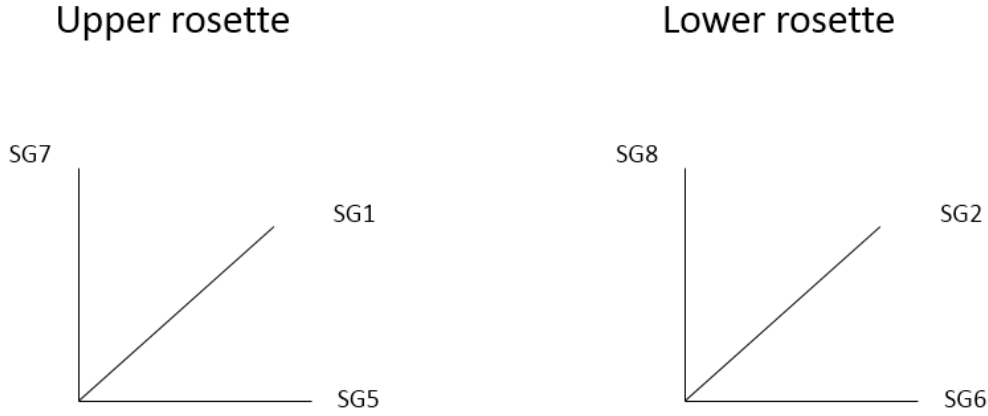


Figure B-1: Strain gauge configuration of the upper and lower strain rosette

Applying the strain rosette equations (equation B4 - B6) to the upper rosette results in:

$$\epsilon_x = \epsilon_5 \quad (B7)$$

$$\epsilon_y = \epsilon_7 \quad (B8)$$

$$\gamma_{xy} = 2\epsilon_1 - (\epsilon_5 + \epsilon_7) \quad (B9)$$

Applying the strain rosette equations (equation B4 - B6) to the lower rosette results in:

$$\epsilon_x = \epsilon_6 \quad (B10)$$

$$\epsilon_y = \epsilon_8 \quad (B11)$$

$$\gamma_{xy} = 2\epsilon_2 - (\epsilon_6 + \epsilon_8) \quad (B12)$$

When a material is subjected to multiaxial stress and strain, and assuming that the material is homogeneous and isotropic and linearly-elastic, it can be analysed using material-property relationships.

According to the generalised Hooke's law, when the material at a point is subjected to a triaxial state of stress,  $\sigma_x$ ,  $\sigma_y$ ,  $\sigma_z$ , the associated normal strains  $\epsilon_x$ ,  $\epsilon_y$ ,  $\epsilon_z$  will be developed. The stresses are related to the strains by using a combination of the principle of superposition, Poisson's ratio, and Hooke's law, in the uniaxial direction. The normal strain in each direction is caused by the separate applications of each of the normal stresses i.e. the strain  $\epsilon_x$  is a result of the superposition of the components in the x-direction due to the respective application of  $\sigma_x$  (Hooke's law), and  $\sigma_y$  and  $\sigma_z$  (the Poisson's ratio). The superimposed normal strain due to the three stresses contributing to  $\epsilon_x$  is shown in equation B13. Similarly, the equations are developed for  $\epsilon_y$  and  $\epsilon_z$ , in their respective directions, as shown in equation B14 and B15. Therefore, it is valid for a strain in a particular direction to exist even though there is an absence of a stress component in that specific direction. This formed the basis for

the requirement to convert all the measured strain rosette values into the stress components in each direction to achieve an unambiguous representation of the reaction to the applied loads.

$$\epsilon_x = \frac{1}{E} [\sigma_x - \nu(\sigma_y + \sigma_z)] \quad (B13)$$

$$\epsilon_y = \frac{1}{E} [\sigma_y - \nu(\sigma_x + \sigma_z)] \quad (B14)$$

$$\epsilon_z = \frac{1}{E} [\sigma_z - \nu(\sigma_x + \sigma_y)] \quad (B15)$$

When an element on a material is subjected to a shear stress  $\tau_{xy}$ , experimental observations reveal that the material will deform only due to a shear strain  $\gamma_{xy}$  i.e.  $\tau_{xy}$  will not cause other strains in the material [41]. Therefore, the relationship between shear stress and shear strain using Hooke's law is expressed in equation B16.

$$\gamma_{xy} = \frac{1}{G} \tau_{xy} \quad (B16)$$

The strain rosettes only measured the in-plane strains. Since the strain gauges were mounted on the free surface of the test specimen, the out-of-plane stress,  $\sigma_z = 0$ . Therefore, the rosettes are subjected to a state, where the general state of stress at a point is represented by a combination of two normal stress components and one shear stress component,  $\sigma_x$ ,  $\sigma_y$ , and  $\tau_{xy}$ , respectively. Applying the generalised Hooke's law, there exists a normal strain,  $\epsilon_z$ , albeit  $\sigma_z = 0$ . Therefore, for the specified state there are four non-zero strain components, namely  $\epsilon_x$ ,  $\epsilon_y$ ,  $\epsilon_z$ ,  $\gamma_{xy}$ . Rearranging equation (B13 - B16) by making the normal stresses and the shear stress the subject of the formula results in equation B17 - B19.

$$\sigma_x = \frac{E}{1 - \nu^2} (\epsilon_x + \nu\epsilon_y) \quad (B17)$$

$$\sigma_y = \frac{E}{1 - \nu^2} (\epsilon_y + \nu\epsilon_x) \quad (B18)$$

$$\tau_{xy} = G\gamma_{xy} \quad (B19)$$

Hereafter, the equations are presented using the  $r$  and  $\theta$  coordinate system as it provides a more suitable representation on the disc, where the notations represent:

$r$  : along the radial direction of the brake disc

$\theta$  : along the circumferential direction of the brake disc

The  $z$ -coordinates (out-of-plane direction) remain unchanged, whereby the into-the-page direction was the positive  $z$ -axis. Hence, for equations B1 to B19 and referring to Figure B-2, the coordinates system was replaced as follows:

$$\theta = x; \quad r = y; \quad \theta r = xy; \quad z = z$$

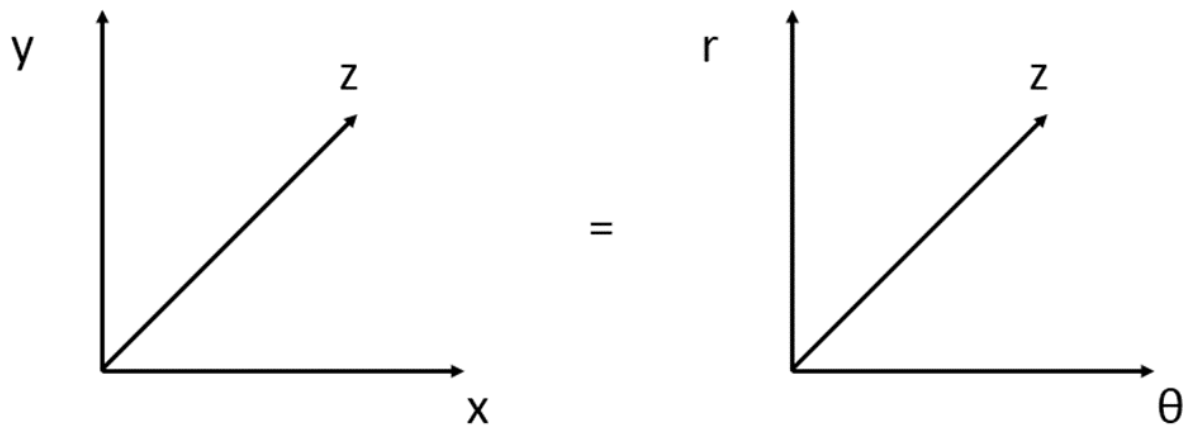


Figure B-2: Adopting the  $r$  and  $\theta$  coordinate system in favour over the  $xy$  system

## APPENDIX C

### C.1 Clamping Load Test Results

The normal strains measured on the disc core at the tested orientation locations around the disc circumference for the clamping load test measured by strain gauge 1 and strain gauge 2 is shown in Figure C-1 and Figure C-2, respectively. The results for strain gauge 3 is shown in Figure 31 in the Results and Discussion (Section 5.1).

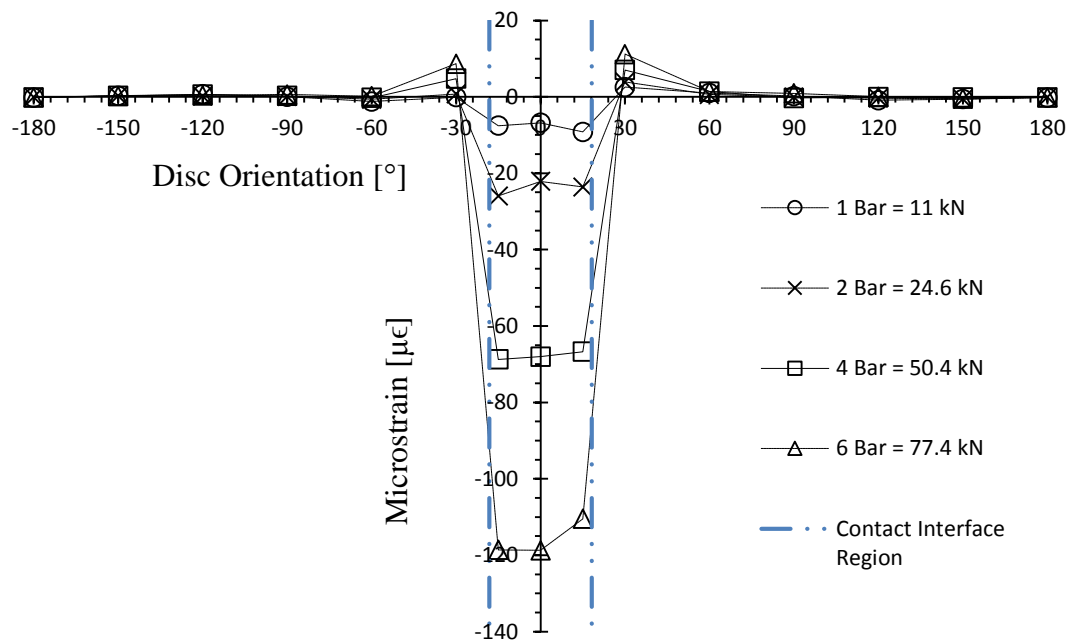


Figure C-1: Normal strains on the solid disc core as measured by strain gauge 1

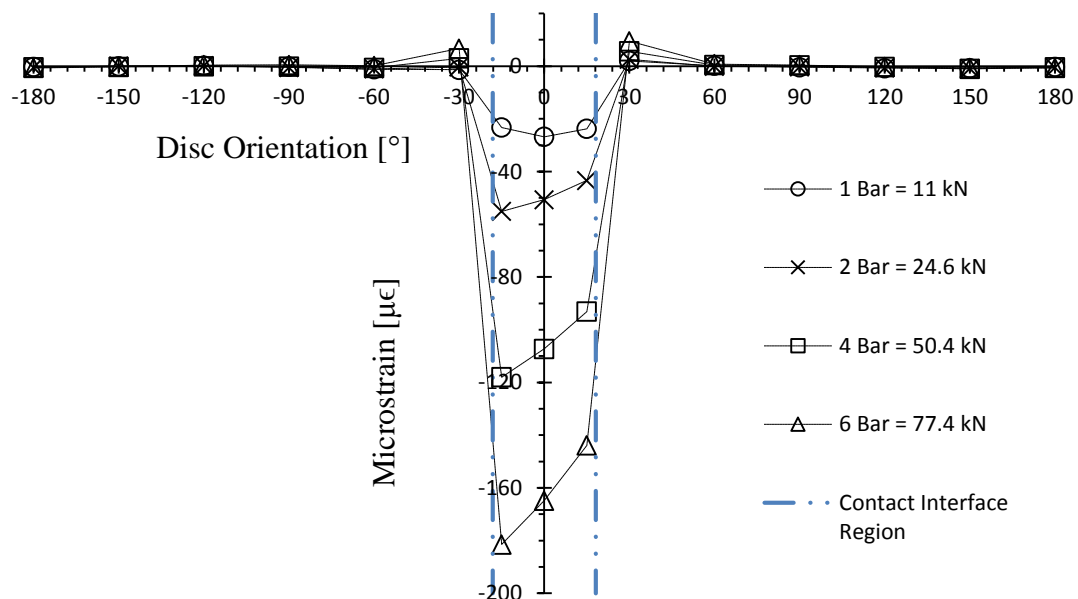


Figure C-2: Normal strains on the solid disc core as measured by strain gauge 2



The stress distribution around the solid disc circumference processed using the strain results from strain gauge 1 and strain gauge 2 are shown in Figure C-3 and Figure C-4, respectively.

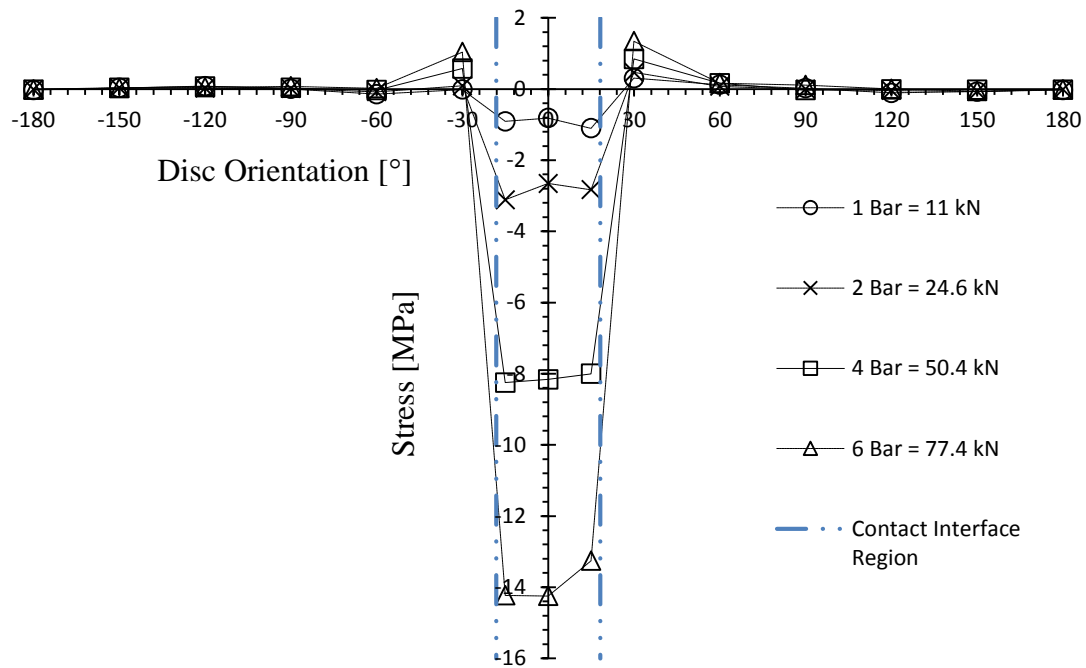


Figure C-3: Stress distribution around solid disc circumference due to applied clamping loads as processed using strain gauge 1 results

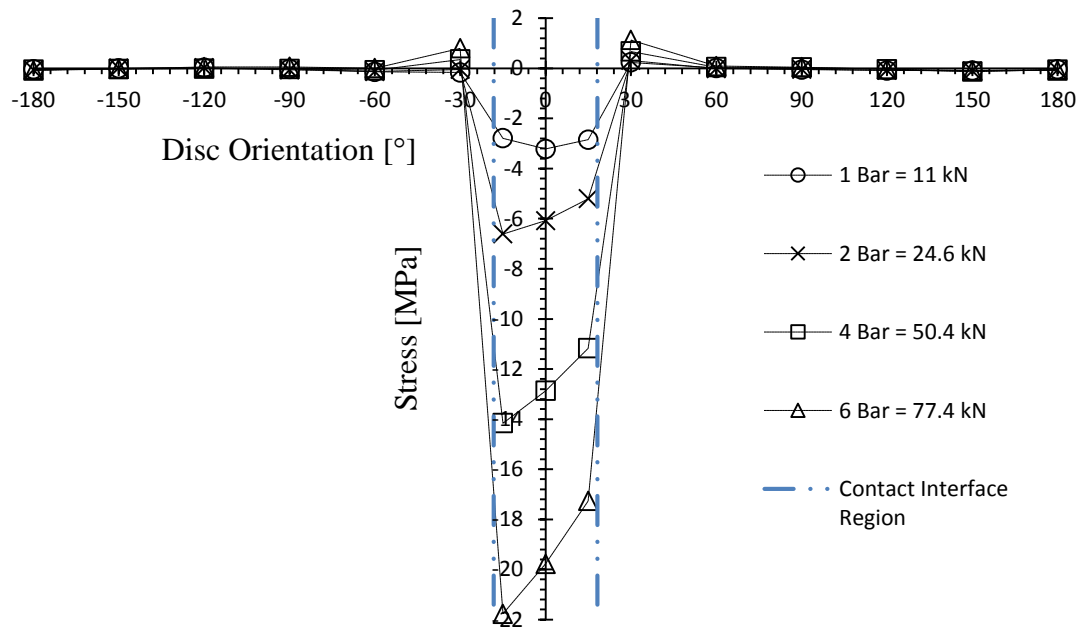


Figure C-4: Stress distribution around solid disc circumference due to applied clamping loads as processed using strain gauge 2 results

The dimensions of the brake pads used for the experimental testing is shown in Figure C-5. The two chamfer regions do not come into contact with the disc during braking when the pads are in the new condition.

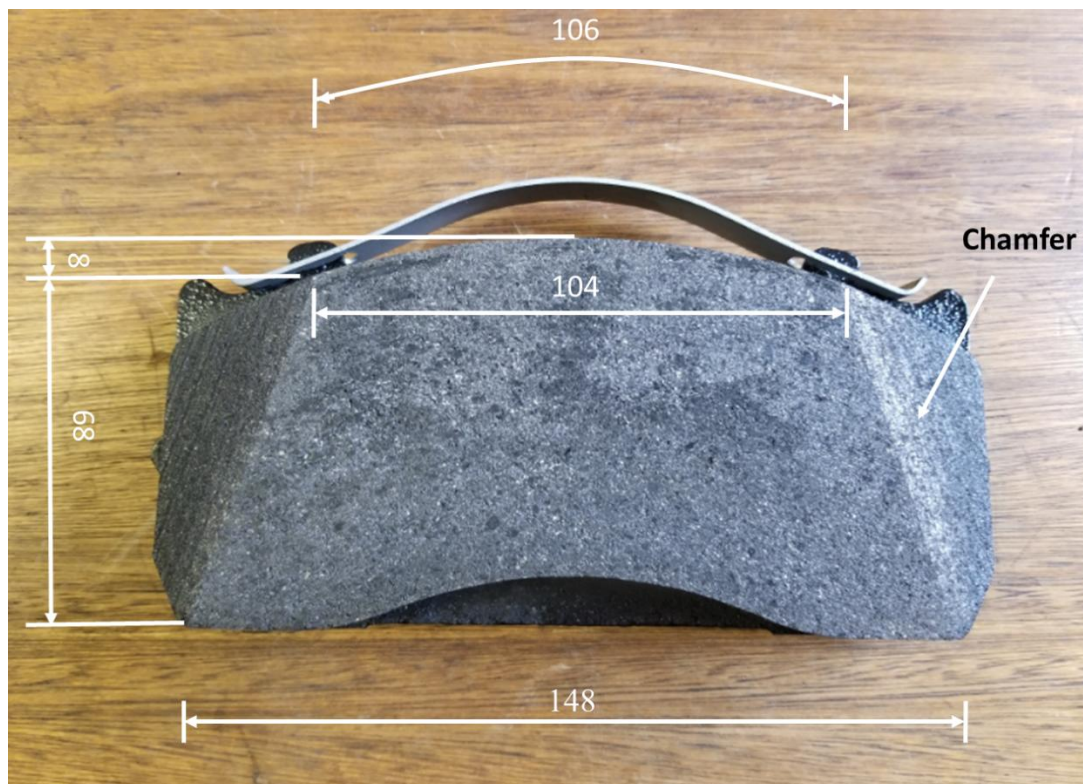


Figure C-5: Dimensions of brake pads utilised for the experimental testing

## C.2 Applied Brake Torque Load Test Results

It was previously stated that for the applied brake torque load test that the disc would be tested under non-rotating conditions and it was experimentally determined that applying a pneumatic chamber pressure of 4 bar (which translated to an applied pad compressive force of 50.4 kN) was sufficient to withstand the disc from rotating during the application of the maximum torque. However, the application of the clamping load resulted in strains being developed on the disc outboard face at a few of the disc orientations, which were subsequently recorded by the strain gauges on the disc face. Since the aim of the applied brake torque load experiment was to measure the stresses purely due to the applied torque, these strains due to the clamping loading were compensated from the final strain readings during data processing. The strain results (due purely to the applied brake torque) as measured by the eight uniaxial strain gauges installed on the pad outboard face for the applied brake torque load test are shown in Figure C-6 to Figure C-13 for strain gauge 1 to strain gauge 8, respectively. Note that the strain gauge number designations are different between the clamping load test and applied torque load test i.e. strain gauge 1 from the

clamping load test is different to the strain gauge 1 referred to by the applied torque load test. The applied brake torque load was 1005 Nm, which was the maximum applied torque. The torque was applied in a counter-clockwise direction as viewed on the disc outboard surface standpoint. Therefore, considering the convention of the disc orientations positions were set as clockwise positive, the leading edge are the positive angle orientations and the trailing edge are the negative angle orientations i.e. the region on the right of the strain results are the leading edge, and the region on the left are the trailing edge. The disc/pad contact interface region is indicated between the two dashed lines.

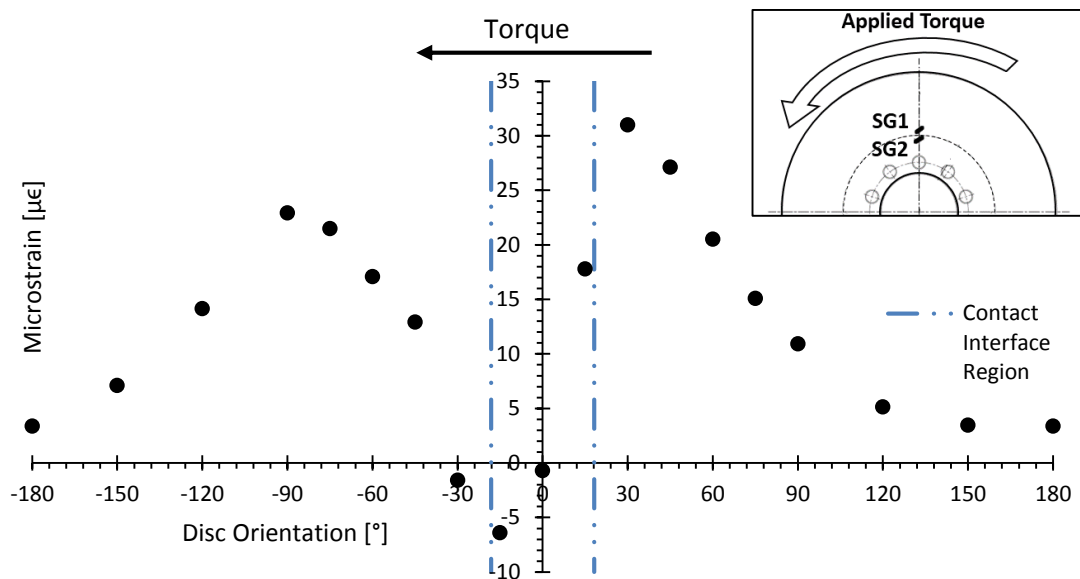


Figure C-6: Uniaxial strains on the solid disc outboard face as measured by strain gauge 1

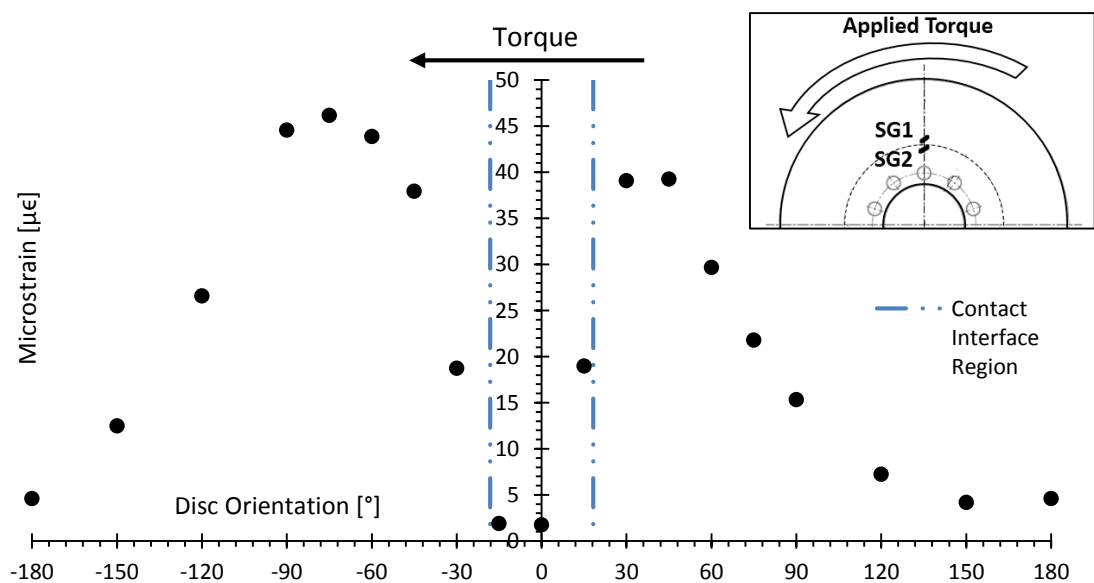


Figure C-7: Uniaxial strains on the solid disc outboard face as measured by strain gauge 2

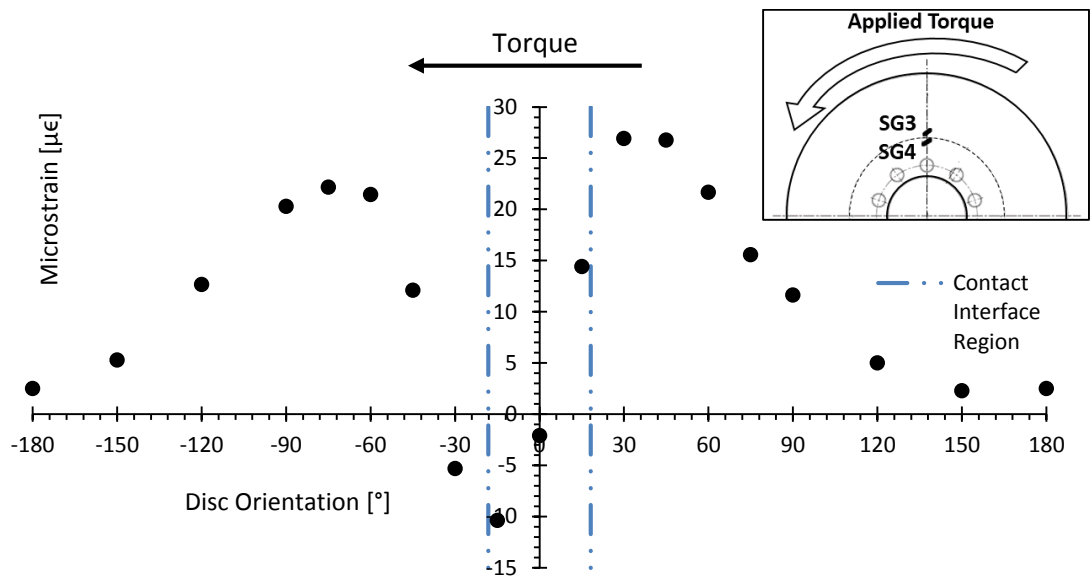


Figure C-8: Uniaxial strains on the solid disc outboard face as measured by strain gauge 3

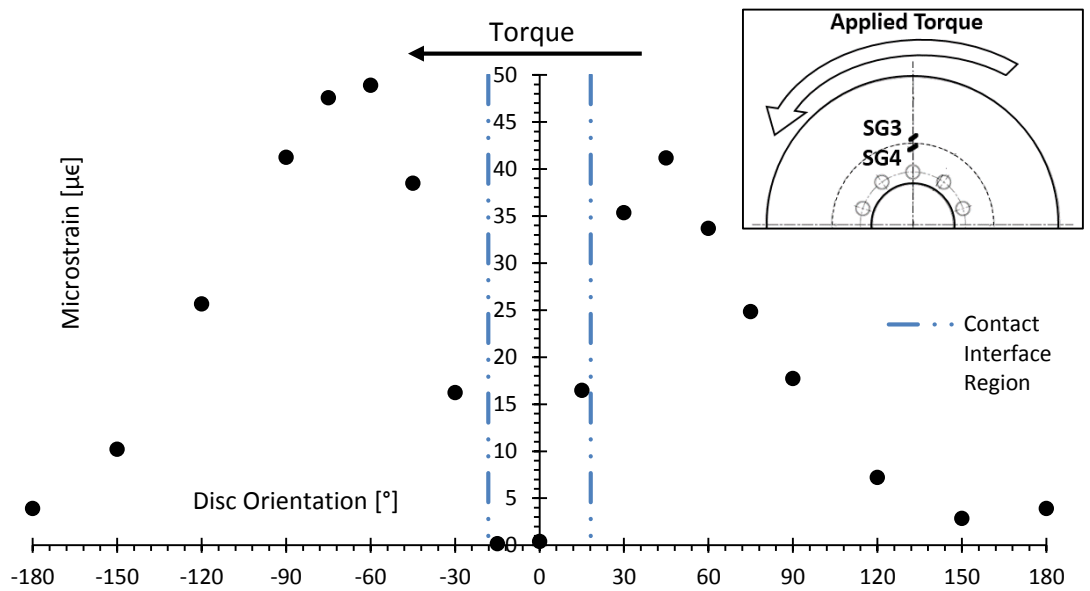


Figure C-9: Uniaxial strains on the solid disc outboard face as measured by strain gauge 4

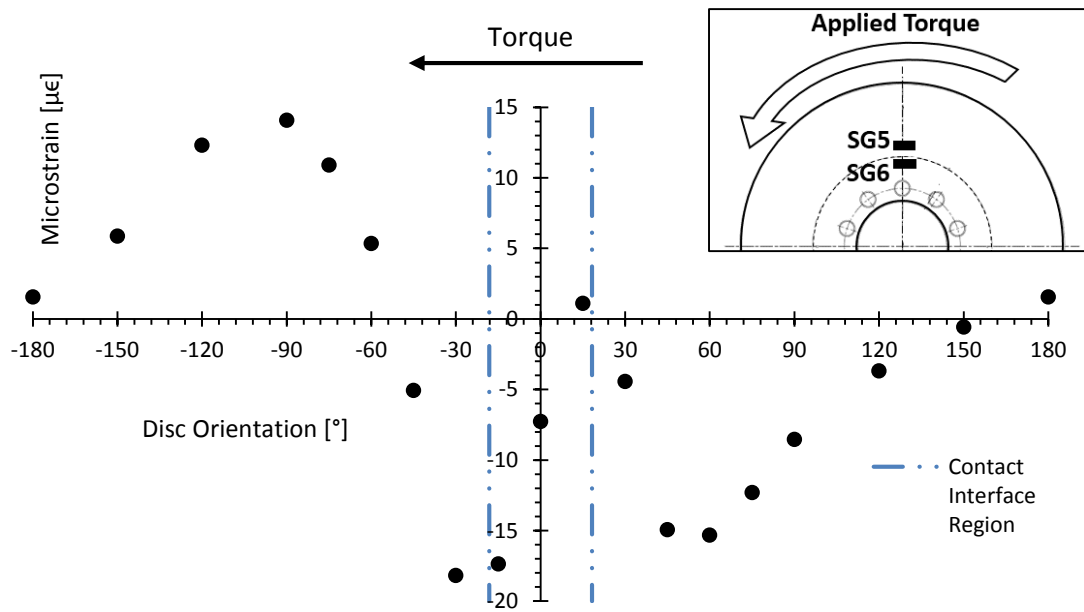


Figure C-10: Uniaxial strains on the solid disc outboard face as measured by strain gauge 5

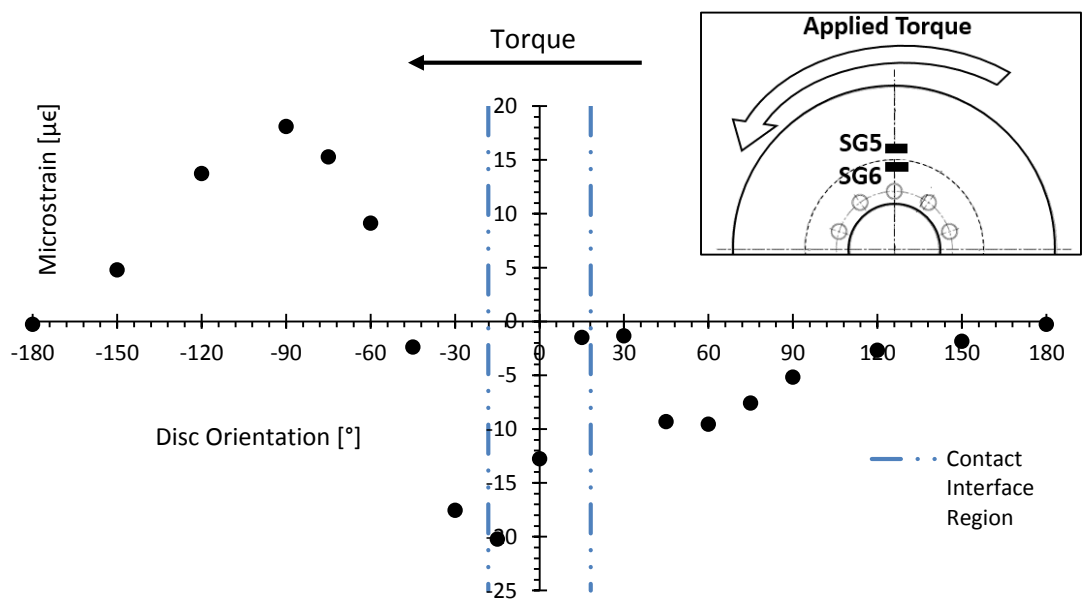


Figure C-11: Uniaxial strains on the solid disc outboard face as measured by strain gauge 6

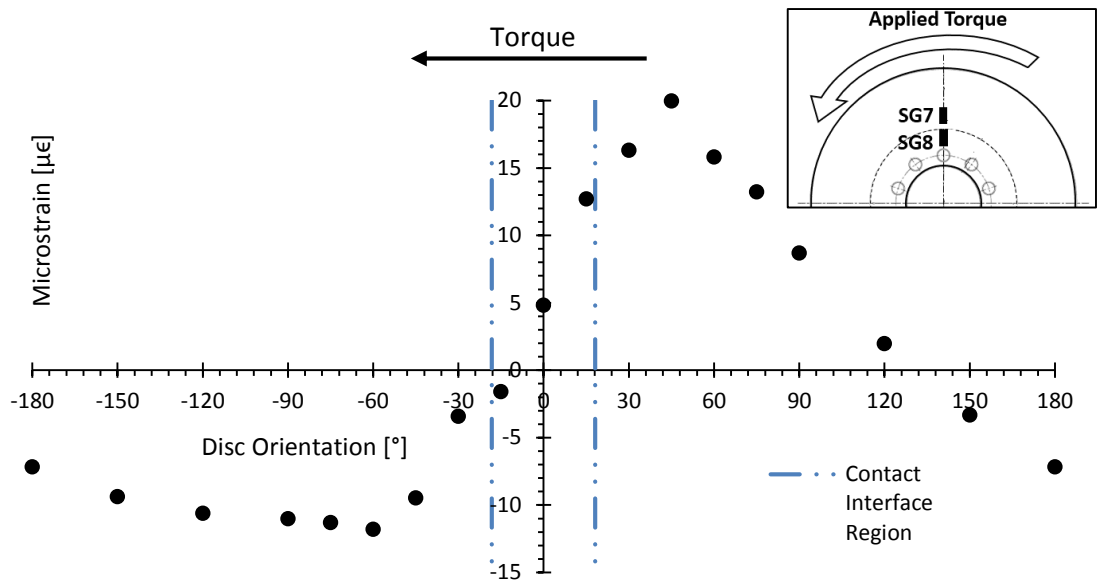


Figure C-12: Uniaxial strains on the solid disc outboard face as measured by strain gauge 7

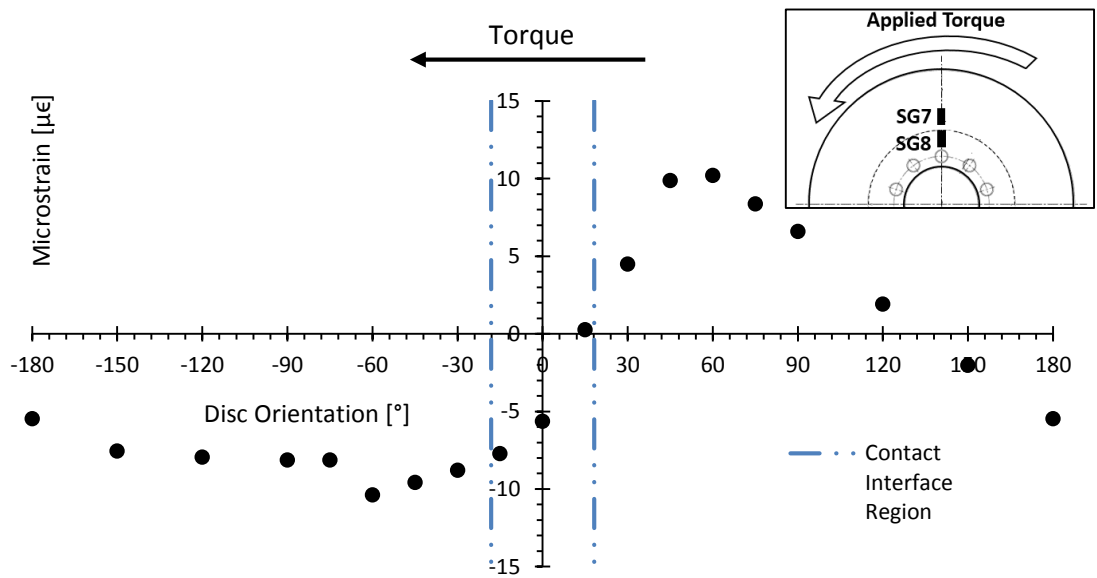


Figure C-13: Uniaxial strains on the solid disc outboard face as measured by strain gauge 8

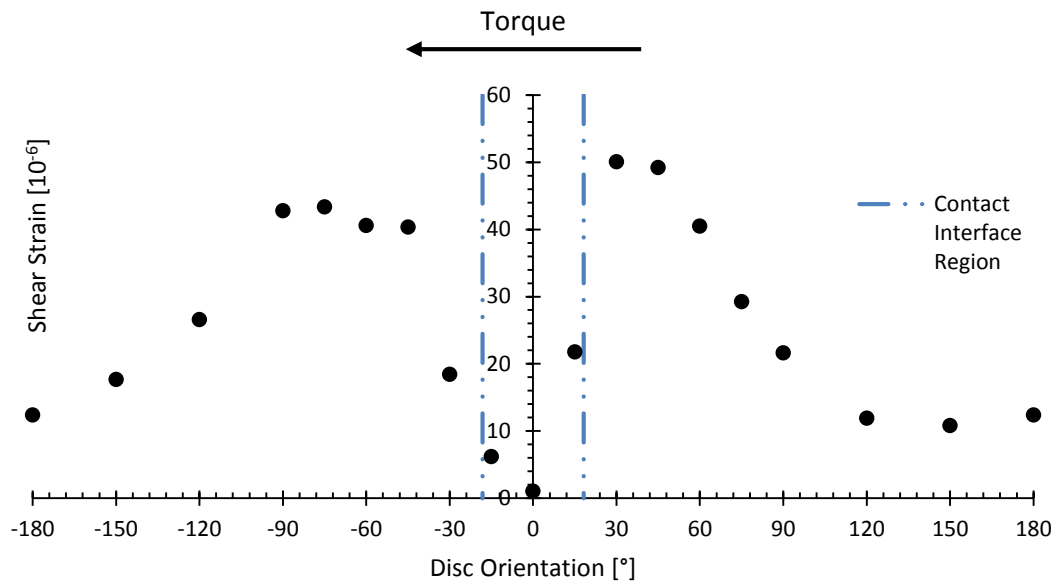


Figure C-14: Shear strains ( $\gamma_{\theta r}$ ) processed for the upper location strain gauge rosette

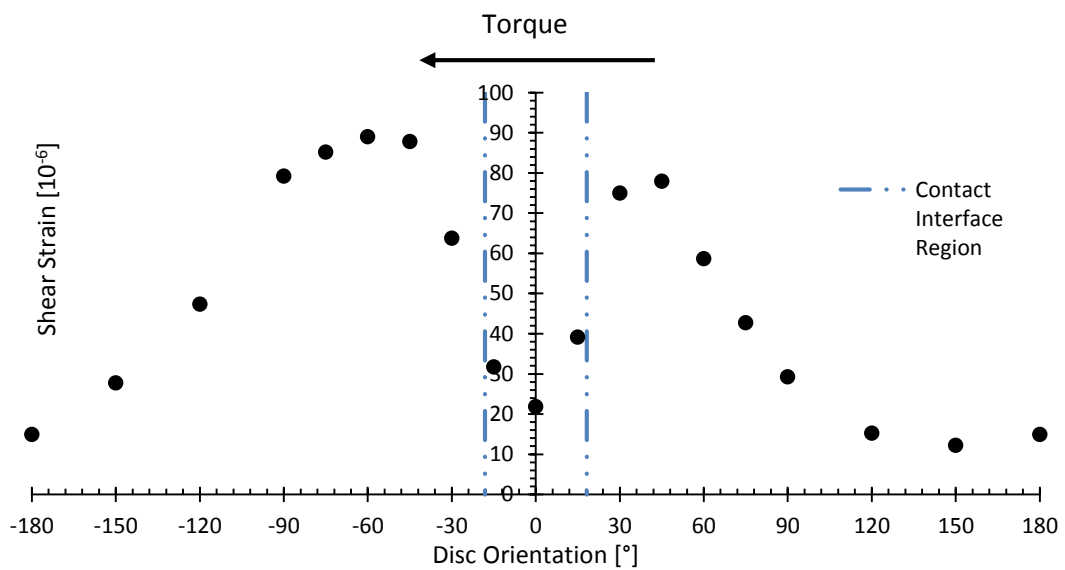


Figure C-15: Shear strains ( $\gamma_{\theta r}$ ) processed for the lower location strain gauge rosette